

Research Activities

Development of Tera-Hertz Light Sources at Compact Electron Linear Accelerator LEENA

S.Hashimoto, S. Chin, K. Kawata, Y. Minagawa[#], Y. Takemura[#], D. Li^{*}, S. Amano, S. Miyamoto
 LASTI, University of Hyogo
[#]JASRI
^{*}Institute for Laser Technology

Abstract

We have been upgrading the 15 MeV compact electron linear accelerator LEENA since last year. As a result, the electron beam transport efficiency and beam currents have been greatly improved. We have also succeeded in measuring both the synchrotron radiation from a bending magnet and Smith-Purcell radiation in a terahertz regime.

Introduction

The compact electron linear accelerator LEENA (Laser Emitted ElectroN Accelerator) is located in the NewSUBARU synchrotron light facility. Because of its old-fashioned control system and insufficient beam monitors, the accelerator could not show good performance at recent. In order to make it possible for NewSUBARU facility users to use radiation in terahertz regime for industry, we are regenerating the accelerator and developing terahertz sources using the accelerator [1,2]. As the terahertz sources we are planning both the synchrotron radiation from a bending magnet and Smith-Purcell radiation. When the electron beams pass through near a metal grating, the induced surface current on the grating radiates electromagnetic waves (Smith-Purcell effect). The main parameters of LEENA are shown in Table. I.

Table I LEENA main parameters

Beam Energy	15MeV
Macro pulse	100 mA (Max.)
RF frequency	2856 MHz
Repetition rate	1-10 Hz
Macro pulse width	5 μ s
Gun	rf gun
Cathode	thermal
Charge per bunch	35 pC
Bunch length	30 ps (design)

Upgrade of the old-fashioned accelerator

The control system of the accelerator was based on PLC, potentiometers and touch-panel. This old-fashioned system made difficult for operators to beam-handle with high precision and high reproducibility. For the flexible tuning of the accelerator, all equipments such as power-supplies are required to be controlled by a PC. Using the OPC server we made it possible for the PC to communicate with the PLC, and beam-operations become easier by using Graphical User Interface programs developed by

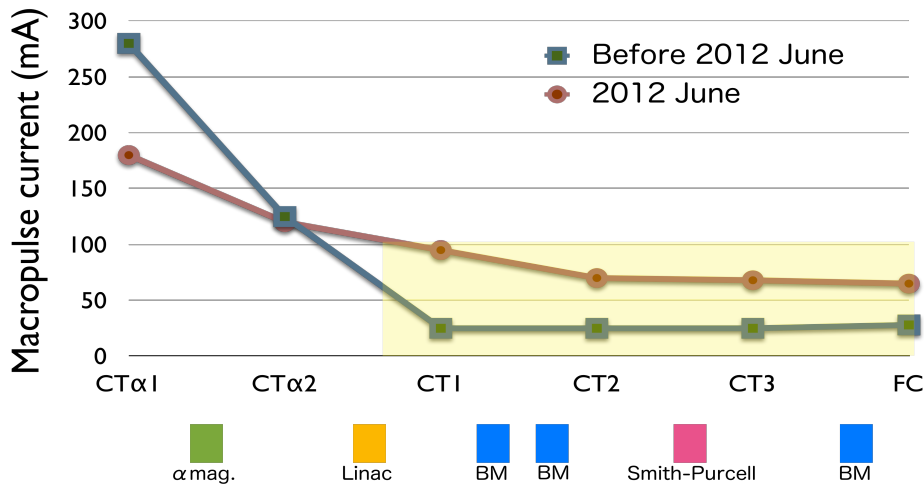


Fig.1 Macropulse current measured by several Current Transformers. Beam transport efficiency was improved after the system upgrades and the fine-tuning.

LabVIEW.

As for vacuum, a few sputtering ionization pumps and vacuum gauges were newly added and after the leak detection and the baking, the vacuum pressure became one digit better than before.

A new screen monitor was installed at the entrance of the alpha magnet for the beam to be injected with the right position and angle to reduce the beam loss at the magnet.

By the above mentioned upgrades the beam transport efficiency was greatly improved as shown in Fig. 1 [3]. The macro-pulse averaged current measured at CT1 (just after Linac) was 95mA, and 65mA at Faraday Cup (FC). The maximum current is limited to 100mA at 15 MeV by the radiation safety regulation.

Measurement of Terahertz radiation from a bend and Smith-Purcell radiation

The schematic drawing of the terahertz measurement is shown in Fig. 2. The synchrotron radiation from a bending magnet and Smith-Purcell radiation were measured with Zero Bias Diode (VDI WR6.5, 110-170 GHz, 2000V/W) through quartz windows [4].

In the case of Smith-Purcell radiation, the measured peak power was about 9.3 μ W with the electron beam of 15MeV, 40mA. Considering the macropulse width of 3.5 μ s and the ZBD antenna aperture of 78.5mm², the energy per mm² per macropulse is 0.4 pJ/mm²/pulse. The measured radiation is “incoherent”, because the measured wavelength (110-170 GHz) is shorter than the expected bunch length of 30 ps.

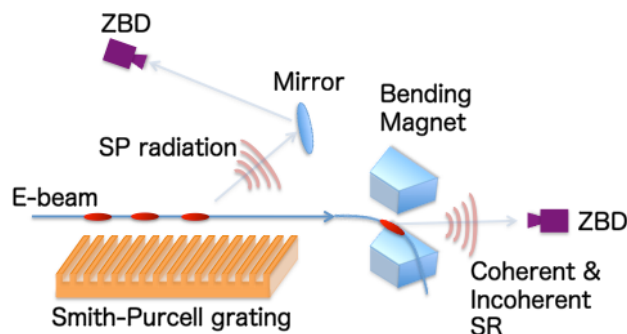


Fig.2 The generation and measurement of Terahertz radiations at LEENA; The synchrotron radiation from the bending magnet and the Smith-Purcell radiation.

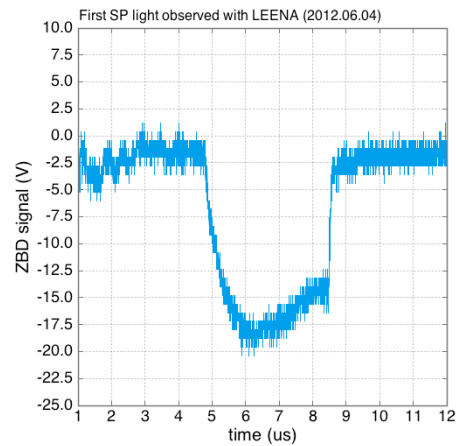


Fig.3 Waveform of Smith-Purcell radiation measured by a Zero Bias Diode.

Undergoing and future plans for developing terahertz sources at LEENA

Although we have succeeded in the first observation of the Smith-Purcell radiation and the synchrotron radiation at LEENA, those radiation intensities were relatively weak because of the incoherent radiation which intensity is proportional to the number of electron in a bunch N . If the bunch length of the electron beam is less than radiation wavelength, the radiation is coherent and proportional to N^2 . The generation of the coherent radiation by short electron bunches is the next important topic in LEENA.

To measure radiation spectrum and estimate bunch length, the Martin-Puplett interferometer is under construction. And BPM (Beam Position Monitors) for nondestructive measurement of beam position and the solenoid coil to focus and guide low energy electron beam just after RF gun are under design and will be installed in near future.

References

- [1] S.Hashimoto *et al.*, Lasti Annual Report, **10**, pp.13-14 (2010).
- [2] S.Hashimoto *et al.*, The 8th Annual Meeting of Particle Accelerator Society in Japan (2011).
- [3] S.Hashimoto *et al.*, The 9th Annual Meeting of Particle Accelerator Society in Japan (2012).
- [4] S.Chin *et al.*, The 9th Annual Meeting of Particle Accelerator Society in Japan (2012).

Laser-plasma extreme ultraviolet source at 6.7 nm using a rotating cryogenic Xe target

S.Amano, and T.Inoue
LASTI/UH

Abstract

A laser-plasma source comprising a rotating cryogenic solid-state Xe target has been studied for use in extreme ultraviolet lithography (EUVL) systems equipped with La/B₄C mirrors. The laser-to-EUV power conversion efficiency (CE) of the cryogenic Xe target was improved to achieve a maximum CE of 0.15% at 6.7 nm with 0.6% bandwidth. We successfully demonstrated the continuous generation of EUV light with an average power of 80 mW at 6.7 nm with 0.6% bandwidth using a Nd:YAG slab laser at a repetition rate of 320 Hz and an average power of 100 W.

Introduction

Recently, a new lithography system that uses La/B₄C mirrors having a reflectivity peak at 6.7 nm has been proposed as a next-generation candidate to supersede the current EUVL projection lithography system, which relies on Mo/Si mirrors having a reflectivity peak at 13.5 nm [1]. This means that a light source emitting around 6 nm will be required for use in future lithography systems for industrial mass production of semiconductors. To achieve a high CE around 6 nm, LPX sources based on targets of high-Z metal elements such as Gd and Tb, have been studied. However, these LPX sources cannot be used effectively for industrial EUVL applications until a number of difficult problems have been resolved, including the high cost of the targets, establishing a way to continuously supply the targets, and the plasma-debris problem associated with such metals, etc.

Here, we propose the use of our Xe LPX source as a 6 nm light source because it emits broadly in the 5–17 nm range and does not exhibit the problems highlighted above. Thus, we characterized the Xe LPX as a source emitting at 6.7 nm with 0.6% bandwidth required for use with La/B₄C mirrors. In this letter, we describe the characteristics of EUV at 6.7 nm using our LPX source.

Experiments

Our LPX source uses the developed target-system described in ref [2]. Figure 1 shows an experimental setup to obtain data for the EUV emission from the cryogenically cooled rotating Xe target. Here, a conventional Q-switched Nd:YAG rod laser (Spectra-Physics, PRO-230) was used in single-shot operation, which could deliver pulses at wavelengths of 1 ω (1064 nm). The laser pulse width was about 10 ns. The pulses were expanded using a beam-expander and focused on the target with an $f = 500$ mm lens so that plasma was produced and emitted EUV

radiation. By changing the position of the focus lens to change a laser spot, laser intensity on the target was adjusted to find an optimized intensity.

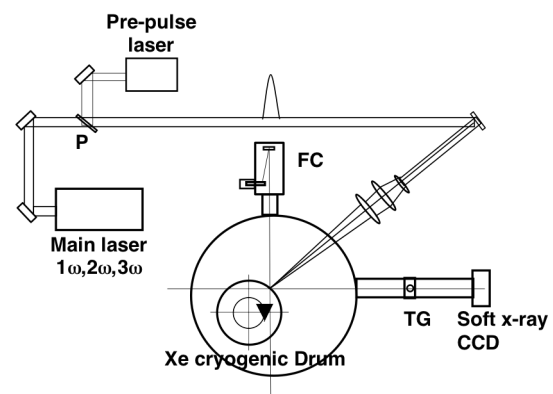


Figure 1. Experimental setup to obtain data of EUV emissions from a cryogenic rotating Xe target. FC represents the Flying Circus III energy generator, and TG is a transmission grating.

To measure the generated EUV emission, we employed an energy detector calibrated at 13.5 nm with 2% bandwidth (SCIENTEC Engineering, Flying Circus III) and a spectrometer having a resolution of 0.76 nm, which is equipped with a transmission grating (50 mm diameter and 1000 line/mm) and a back-illuminated 2D-CCD camera. At first, the 13.5 nm light with 2% bandwidth in the emission spectrum was calibrated using the energy detector. Next, the required 6.7 nm light with 0.6% bandwidth in the emission spectrum was compared with the 13.5 nm light with 2% bandwidth to obtain an absolute CE for the 6.7 nm light with 0.6% bandwidth, taking into account the sensitivity of the CCD camera. To achieve the highest CE at 6.7 nm with 0.6% bandwidth, we attempted to control the plasma

parameter by changing the driving laser conditions. We investigated the dependence of the CE on the drum rotation and laser intensity.

Results

Under certain operating conditions, humps around 6 nm were observed in the emission spectra (see Fig. 2). The emission spectra in Fig. 2 were obtained using a 1ω pulse in the rotation and rest condition. In previous experiments for the EUV emission at 13.5 nm with 2% bandwidth, we observed an increase in CE and a lower production of fast ions when the drum was rotated, as compared with conditions when the drum was at rest [3]. In the present study for the EUV emission at 6.7 nm, the same phenomena were observed as shown in Fig. 2, that is, a hump was observed at around 6 nm, which had a higher intensity in the EUV emission spectrum corresponding to the rotating drum as compared with the EUV emission spectrum corresponding to the drum at rest. This result is explained by the following exploration. The Xe gas vaporized on the target surface by the wipers during the rotation produces an optically thick plasma having an optimized density and a temperature suitable for emitting EUV radiation, where the satellite lines of the plasma contribute effectively to increasing the EUV intensity. As a result in this work, it was found that a maximum CE at 6.7 nm with 0.6% bandwidth was obtained for the 1ω laser irradiation and the rotating drum target (Fig. 2), and its CE was estimated from this emission spectrum to be 0.15%. The CE was spatially integrated taking into account its EUV angular distribution. Because the bandwidth of 0.6% for the La/B₄C mirror reflectivity is narrower than the 2% for the Mo/Si mirror, the available reflected power is intrinsically small. In the case of 13.5 nm light, a maximum CE was also obtained for the 1ω laser irradiation and the rotating drum target, however, the laser intensity in this case was 1×10^{10} W/cm² at a laser energy of 0.8 J. On the other hand, the maximum CE at 6.7 nm with 0.6% bandwidth was obtained for the higher laser intensity of 4×10^{12} W/cm² at a laser energy of 0.8 J. Because the Xe[XI] ion mainly emits 13.5 nm light and the Xe[XLIV] ion emits 6.7 nm light, it is considered that a higher laser intensity is required to achieve a higher charge state.

Because CE is dependent on the laser intensity, a CE at 6.7 nm with 0.6% bandwidth was estimated to be 0.08% for a laser intensity of 1.5×10^{10} W/cm² at a laser energy of 0.3 J. Therefore, when our developed slab laser having an average power of 100 W (0.3 J@320 Hz) was used to irradiate the rotating target, a continuous EUV generation was achieved with an average power of 80 mW at 6.7 nm with 0.6% bandwidth.

Though the obtained power is still low, our source is the only LPX source at present that can generate an emission continuously at 6.7 nm.

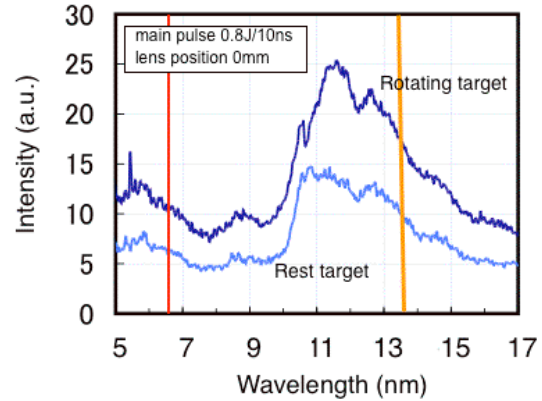


Figure 2. EUV radiation spectra with a hump at 6 nm emitted from the cryogenically cooled Xe drum target. The lines represent 13.5 nm light with 2% bandwidth and 6.7 nm light with 0.6% bandwidth, respectively. 1ω pulse irradiation (0.8 J/10 ns) for both the rotating drum and the drum at rest. The laser intensity was 4×10^{12} W/cm².

References

- [1] J. Benschop, EUV: past, present and prospects, Keynote I, *2009 International Symposium on Extreme Ultraviolet Lithography*, Prague Czech, October 2009, International Sematech, Available from: <<http://www.semtech.org/meetings/archiv/litho/index.htm>>.
- [2] K. Fukugaki, S. Amano, A. Shimoura, T. Inoue, S. Miyamoto, and T. Mochizuki: *Rev. Sci. Instrum.* **77**, 063114 (2006).
- [3] S. Amano, K. Masuda, A. Shimoura, S. Miyamoto, and T. Mochizuki: *Appl. Phys. B.* **101**, 213-219(2010).

Effective collision cross section of xenon plasma debris in argon buffer gas

Tomoaki Inoue, Takayasu Mochizuki, Kazuya Masuda, Sho Amano, and Kazuhiro Kanda

Abstract

Mitigation of fast debris and soft x-rays generated from laser-produced xenon plasmas were studied in an argon buffer gas in laser intensities of 10^9 – 10^{11} W/cm² using a cryogenic drum target. Considerable mitigation of debris was confirmed by measurements of material sputtering. From the experimental results, an attenuation parameter of sputtering by the debris $\bar{\sigma}_1$ and an absorption cross section of soft x-rays at 13.5 nm $\sigma_2(13.5\text{nm})$ were derived to be 2.2×10^{-20} m² and 1.8×10^{-22} m², respectively. Moreover, $\bar{\sigma}_1$ is concluded to be equivalent to the effective collision cross section σ_1 of a debris particle at a kinetic energy of 1–4 keV. Sufficient debris mitigation can be obtained together with low soft x-ray absorption (less than 10%). These parameters provide a useful design tool for realizing a practical soft x-ray source because they predict the effect of the buffer gas well.

Introduction

Soft x-rays from high-temperature, high-density plasmas produced by focusing a high-intensity laser on target materials are expected to be useful as a compact high-brightness soft x-ray source for a variety of applications [1]. However, debris emitted from the plasmas remains one of the most serious problems that must be solved before the source can be used for practical applications. The debris generally causes sputtering and/or deposition on the surfaces of condenser mirrors [2], degrading the mirrors' reflectivity and thus reducing the usable x-ray output power. Chemically inert xenon debris from a xenon plasma target will not be deposited on the mirror surface [2]. Thus, mitigation of fast xenon debris by the buffer gas is a technical issue to be resolved. However, a trade-off between mitigation of the fast debris and absorption of the soft x-rays, both of which are caused by the buffer gas, remains to be studied.

In this paper, we report the experimental results and discuss the effective attenuation cross-sections of plasma debris and soft x-rays in argon buffer gas. We find an effective debris mitigation parameter that is useful for realizing a practical laser-produced soft x-ray source.

Experimental

A rotating drum cryogenic solid xenon target was used. A Q-switched 1.06- μm Nd:yttrium aluminium garnet laser (Quantel YG980) pulse was focused through a $f/500$ lens on the target surface at an angle of 5° to normal incidence. The laser pulse duration was 8 ns at full width at half maximum with an energy of 300 mJ/pulse for either single shot or repetitive shots at 10 Hz. The laser intensity was adjusted in a range of 10^9 – 10^{11} W/cm² by changing the lens position. The target chamber was evacuated by a turbo-molecular pump that maintained a xenon pressure in the chamber of less than 0.2 Pa except

when the argon buffer gas was present. The argon gas at room temperature was introduced into the chamber through a nozzle on an upper wall of the chamber.

The sputtering rate and the absorption rate at 13.5 nm were measured using the QCM and soft x-ray calorimeter, respectively, as a function of the argon gas pressure, which was varied by adjusting the flow rate of the argon gas.

Results and discussions

X-ray emission experiments were performed with the rotating drum cryogenic xenon target. We obtained the laser intensity dependence of the soft x-ray CEs at 5–17 nm. The laser intensity range at which the CE is significant is found to be 10^9 – 10^{11} W/cm², and the maximum CE was about $25\%/2\pi\text{Sr}$.

The circles and triangles in figure 1 represent the sputtering rate $N_{\text{sputter}}(nl)$ and transmission of soft x-rays $T(nl)$ at 13.5 nm, respectively. Here, nl should be expressed more precisely by $\int dn l$, but we assumed that n was uniform in a spatial range of interest for observing the buffering effect.

Note that the experimentally observed $N_{\text{sputter}}(nl)$ decreased in an approximately exponential form as nl increased. Thus, we assume that $N_{\text{sputter}}(nl)$ is well described by

$$N_{\text{sputter}}(nl) = N_{\text{sputter}}(0) \exp(-\bar{\sigma}_1 nl), \quad (1)$$

where $\bar{\sigma}_1$ is the attenuation parameter of sputtering for the argon gas buffer. It has the same unit as a cross section.

Similarly, $T(nl)$ is expressed by

$$T(nl) = \exp(-\sigma_2(13.5\text{nm})nl), \quad (2)$$

where $\sigma_2(13.5\text{nm})$ is the absorption cross section of soft x-rays at 13.5 nm for an argon molecule. From figure 1, $\bar{\sigma}_1$ and $\sigma_2(13.5\text{nm})$ were derived to be 2.2×10^{-20} m² and 1.8×10^{-22} m², respectively.

On the other hands, the relationship between the collision cross section of a debris particles $\sigma_1(E, Z)$

and the attenuation parameter of sputtering $\bar{\sigma}_1$ is expressed by

$$\bar{\sigma}_1 = \frac{\sum_{Z=0}^{\infty} \int \sigma_1(E, Z) s(m, E) N_{Xe}(nl, E, Z) dE}{\sum_{Z=0}^{\infty} \int s(m, E) N_{Xe}(nl, E, Z) dE}, \quad (3)$$

where $N_{Xe}(nl, E, Z)$ is the number of debris particles per unit energy interval arriving at the observation point which is located at a distance l from the source with a buffer gas of density n and $s(m, E)$ is the average number of particles sputtered by a debris particle having a mass m and kinetic energy E . Note that $s(m, E)$ depends on the mass m and kinetic energy E of the colliding debris, and also on the bombarded target material, but not on the charge number Z . We assume the effective charge number in the target material [3].

To evaluate $\bar{\sigma}_1$, the kinetic energy dependence of $s(m, E)$ was calculated by the numerical code The Stopping Range of Ions in Matter (SRIM), as shown in figure 2. The values of $s(m, E)$ for the above sputtered materials were normalized by those at a kinetic energy of 4 keV.

Figure 2 shows that $s(m, E) \cdot N_{Xe}(0, E, \bar{Z})$ has significant values only at energies of 1–4 keV. Thus, we can take a representative average value $\overline{s(m, E) \cdot N_{Xe}(nl, E, \bar{Z})}$ as $s(m, E) \cdot N_{Xe}(nl, E, \bar{Z})$ in (3) for each mirror material in this energy range. The value of $\sigma_1(E, \bar{Z})$ averaged over 1–4 keV should be equivalent to $\bar{\sigma}_1$:

$$\bar{\sigma}_1 \approx \sigma_1. \quad (4)$$

Hereafter, we define $\bar{\sigma}_1$ as the effective collision cross section of a debris particle colliding with a buffer argon gas molecule.

Conclusion

The attenuation parameter of sputtering by the debris $\bar{\sigma}_1$ is concluded to be equivalent to the effective collision cross section σ_1 of a debris particle at kinetic energies of 1–4 keV. From figure 1, $\bar{\sigma}_1$ and $\sigma_2(13.5\text{nm})$ were evaluated as $2.2 \times 10^{-20} \text{ m}^2$ and $1.8 \times 10^{-22} \text{ m}^2$, respectively.

Therefore, sufficient debris mitigation and low absorption of soft x-rays (less than 10%) can be obtained. The obtained parameters are useful as a design tool for realizing a practical laser-produced plasma soft x-ray source because they predict the effects of a buffer gas well.

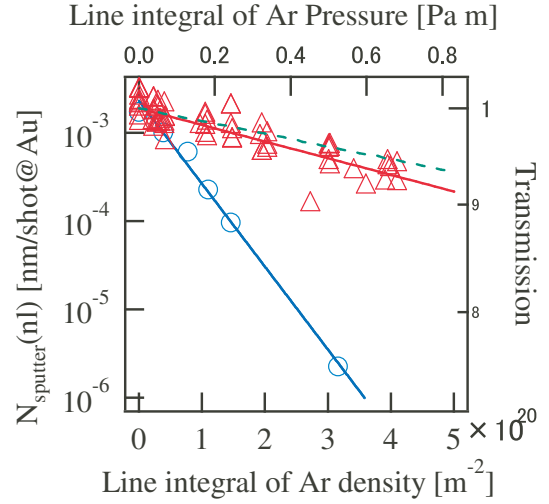


Figure 1 Mitigation of Au sputtering by fast xenon debris (○) and transmission of 13.5 nm soft x-rays (△; experimental, dotted line; Henke et al [4]) as a function of the line integral of the argon pressure.

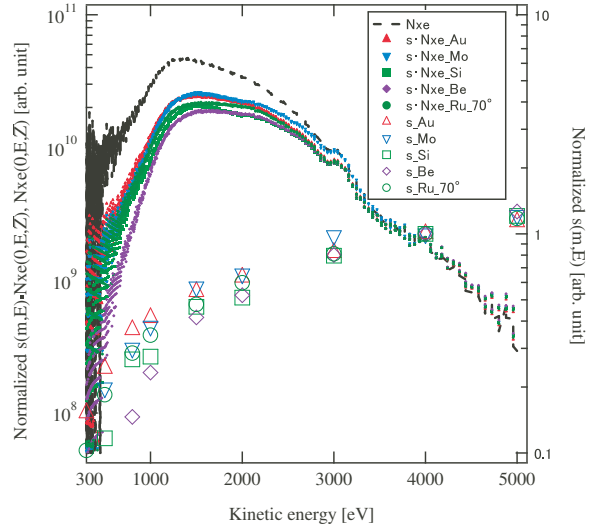


Figure 2 Kinetic energy dependences of the number of xenon ions $N_{Xe}(0, E, \bar{Z})$ and the sputtering rates $s(m, E)$.

Reference

- Tomoaki T, Mochizuki T, Kazuya M, Amano S, Sekioka T and Kanda K 2011 *J. Phys. B: At. Mol. Opt. Phys.* **45** 115401
- [1] Bakshi V 2005 *EUV Source for Lithography* (SPIE, Bellingham, WA) p. 4
- [2] Mochizuki T 2000 *Proc. SPIE* **3886** 306
- [3] Ziegler J F, Biersack J P and Littmark U *The Stopping and Range of Ions in Solids (The Stopping and Ranges of Ions in Matter vol 1)* ed J F Ziegler, p 5
- [4] Henke B L, Gullikson E M and Davis J C 1993 *X-ray interactions: photoabsorption, scattering, transmission, and reflection at E=50-30000 eV, Z=1-92, Atomic Data and Nuclear Data Tables* **54** 181 http://henke.lbl.gov/optical_constants/

EUV Interference Lithography for 1X nm

**Takuro Urayama, Takeo Watanabe, Yuya Yamaguchi, Naohiro Matsuda,
Yasuyuki Fukushima, Takafumi Iguchi, Tetsuo Harada, and Hiroo Kinoshita**

*Center for EUVL, Laboratory of Advanced Science and Technology for Industry,
University of Hyogo
3-1-2 Koto, Kamigori-cho, Ako-gun, Hyogo, 687-1205, Japan*

EUV interference lithographic exposure tool was developed to evaluate hp 20 nm and below. The transmission diffraction grating with hp 30-nm absorber pattern was succeeded to fabricate. In the fabrication process of the transmission diffraction grating, SiO₂ hard mask process and the center stop process were applied to obtain high contrast of the interference fringes to replicate resist fine pattern. In addition, the vibration effect was succeeded to reduce. As results, hp 22.5 nm, hp 20 nm, hp 17.5 nm, and hp 15 nm resist patterns were succeeded to replicate by the two-luminous-flux interference exposure using the two-window transmission diffraction grating in EUV-IL. In addition, the hole pattern of hp 35 nm and hp 28-nm the four-luminous-flux interference exposure using the four-window transmission diffraction grating was succeeded to replicate.

Keywords: EUVL, interference lithography, grating, resist, non-chemical amplified

1.Introduction

Extreme ultraviolet lithography (EUVL) [1] is the most promising technology to be used in high volume manufacturing of the semiconductor devices around 2012 [2]. In EUVL for 22 nm node, the top three technical issues which are listed in order of amount of the problems are defect-free EUV mask, EUV light source with high power and high stability, and EUV resist which satisfies with high resolution, high sensitivity, low line width roughness (LWR), and low outgas.[3] For the extending EUVL to 1x nm node, EUV resist is the top issue.[3] High sensitivity, low LWR, and low outgas should be achieved simultaneously. The resist platform should be changed for 16 nm node and below.[4,5] Thus, EUV resist development for 16 nm node is not so easy. However, there is no exposure tool which can evaluate the resist pattern width of 1X nm. Therefore, we developed the exposure tool based on the EUV interference lithography (EUV-IL) [6]. Previously we demonstrated hp 25 nm resist pattern using EUV-IL.[7-9]

This paper focuses on the pattern replication of 1X nm by the improvement of the transmission grating and the EUV-IL exposure tool.

2.Experimental

2.1 EUV interference lithography

The beamline-setup configuration of the EUV-IL is shown in Fig. 1. The EUV-IL exposure tool was installed in the class 100 clean room at the end station of BL9 beamline in NewsUBARU synchrotron radiation facility [10] which belongs to the University of Hyogo. The 10.8-m-long undulator was employed as a light source of the BL9 beamline. By tuning the undulator gap, the EUV monochromated wavelength of 13.5 nm can be produced by the undulator, and the flux intensity of the EUV light is approximately 1,000 times higher than that from the bending magnet as a light source [10].

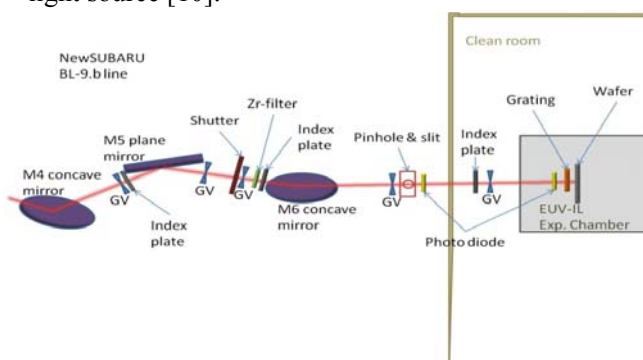


Fig. 1 View of interference lithography system

In the optics design concept of the EUV-IL beamline, to increase the exposure throughput of the EUV-IL, the

number of the optical mirrors reduced as much as possible. And then, reducing the exposure time, it can prevent from the vibration effect.

The principle of the interference lithography [11] based on the two-luminous-flux interference exposure using the two-window transmission grating is shown in Fig.2 By one grating, coherent EUV light is diffracted to the 0th, ±1st, ±2st, order lights. As shown in Fig.2, at the interference point of 1st-order and -1st-order diffracted lights, the interference fringes were created. Since the pitch the interference fringes have a half pitch size of the diffraction grating, replication pattern pitch of the resist pattern has a half pitch size of the diffraction grating.[11]

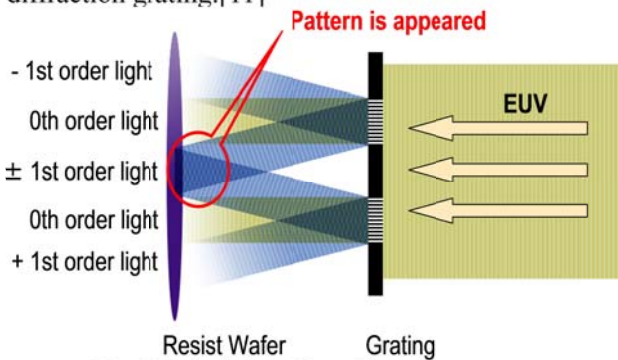


Fig. 2 Principle of interference exposure

2.2 Fabrication of the transmission diffraction grating

The key element of EUV-IL is the transmission diffraction grating.[7] In the fabrication of the transmission diffraction grating for the replication of 20 nm width resist pattern and below, the SiO₂ hard mask process was optimized and the center stop processes was improved.

Figure 3 shows the fabrication process of the transmission diffraction grating. It is prepared that 100-nm-thick Si₃N₄ coating with low film stress on front and back surface of 4-inch Si wafer. Electron beam resist ZEP520A (Nippon Zeon) was coated on it and diffraction grating pattern was replicated by electron beam lithography using by 50 kV electron beam direct writing system (ELS-7500, Elionix). Then the SiO₂ grating pattern was replicated using the inductive coupled plasma of reactive ion etching (ICP-RIE, TCP 9400SE, Lam Research) method employing CF₄ reactive gas by ZEP520A resist pattern as a mask. And the TaN diffraction grating pattern was replicated using ICP-RIE dry etching method employing Cl₂ reactive gas and SiO₂ grating pattern as a mask. The etching time of TaN was increased to 170 s to obtain the fine structure diffraction grating TaN pattern. After removing the residual resist, silicon substrate back etch by KOH solution was applied to obtain a membrane structure of the TaN diffraction pattern on a Si₃N₄

membrane. RF power, bias power, and total pressure were 100 W, 25 W, and 1.3 Pa, respectively. The reactive gas flow rate and the dry-etching time period are shown in Table. 1.

Table 1. Etching process conditions

Mask layer/Etched layer	Gas	Gas flow rate (sccm)	Etch time (s)
Resist/SiO ₂	CF ₄	60 sccm	50
Resist	O ₂	20 sccm	20
SiO ₂ /TaN	Cl ₂ +He	25 sccm+75 sccm	170

In order to increase the light contrast of the interference fringes, the transmitted light between the two-window grating have to be cut off. “Center stop” process was applied after the back-etching silicon substrate. A polymer type chemically amplified EB resist was employed in instead of ZEP520A resist of the center stop layer because of the benefit of the EUV light attenuation. The resist thickness for the center stop was 2 μm because of the enough absorbance of EUV wavelength.

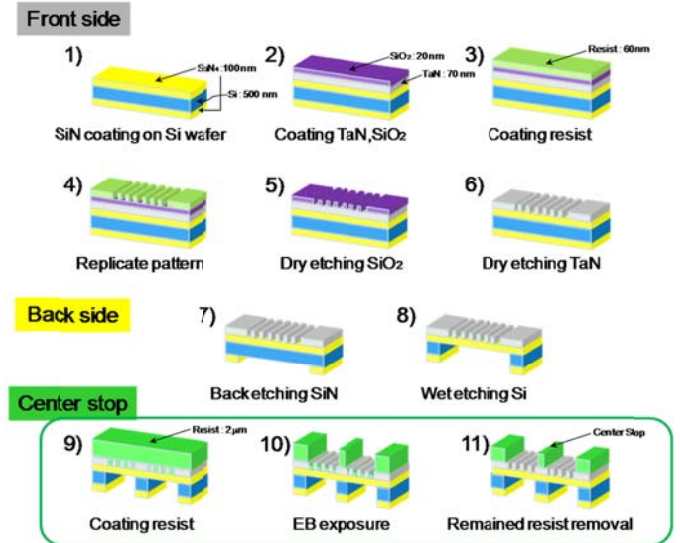


Fig. 3 Fabrication process of the transmission diffraction grating

Figure 4 shows the fabricated transmission diffraction grating. The transmission diffraction grating has four sets of the two-window diffraction grating pattern, such as hp 45 nm, hp 40 nm, hp 35 nm, and hp 30 nm. Using this grating, resist pattern of hp 22.5 nm, hp 20 nm, hp 17.5 nm, and hp 15 nm can be replicated on a wafer. The distance between the grating and a wafer was set to be approximately 1 mm.

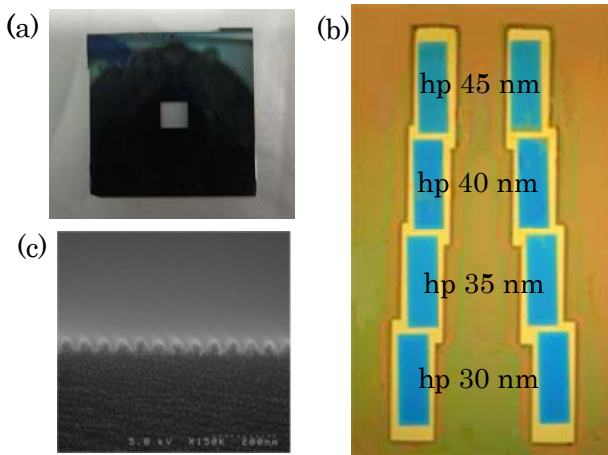


Fig. 4 Fabricated transmission diffraction grating; (a) top view of the transmission grating, (b) arrangement of four sets of the two-windows of diffraction grating, and (c) cross sectional view of the hp 30 nm diffraction gratings before back etching the Si substrate.

2.3 Vibration removal

Since the vibration affects with the replication of the resist pattern, the vibration has to be reduced.

The vibrations on the grating and wafer stages were measured using an accelerometer (Rion Co., Ltd.). As a result of the vibration measurement, the vibration originates to the pumping system. And previous grating stage had a tilt adjustment system and a gap adjustment system with a long range. Since adjustment system had a large degree of freedom, stages were easily to affect with vibrations. Therefore, novel grating stages were designed and installed in the EUV-IL exposure tool. Tilt adjustment system was removed and increased the rigidity of the stages. The setup of the stages is shown in Fig.5.

Figure 6 shows the vibration measurement result of the vibration displacement of the grating and the wafer stages before and after the improvement of the grating stage. After the improvement of the grating stage, the low frequency vibration can be reduced. Before the improvement of the grating stage, the vibration displacement between the grating and the wafer stages was 30 nm in maximum. However, after the improvement of the grating stage, the vibration displacement was reduced to be 5 nm in maximum.

Figures 7(a) and 7(b) show 25 nm line and space pattern before and after the vibration improvement, respectively. As shown in Fig. 7(b), after the improvement, L/S resist pattern with high contrast was replicated. In addition, as shown in Fig.8, by the four-luminous-flux interference exposure using the four-window transmission diffraction grating, hole pattern can be replicated. In the four diffraction grating

system, the replicating resist pattern pitch is $\sqrt{2/2}$ times by the pitch of the transmission diffraction grating. Figures 9(a) and 9(b) show the replicated resist patterns before and after the vibration improvement. After the vibration improvement as shown in Fig.9 (b), 35 nm hole resist pattern was replicated with high contrast.

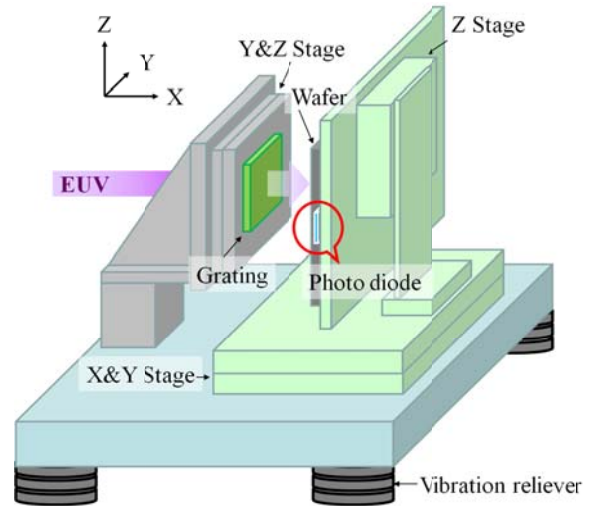


Fig. 5 Stage setup in the EUV-IL exposure tool

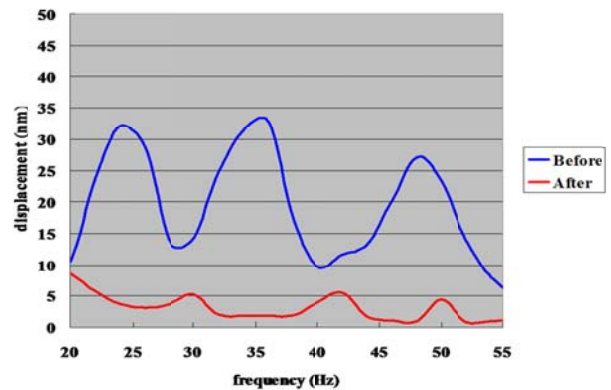


Fig. 6 Vibration of exposure stage

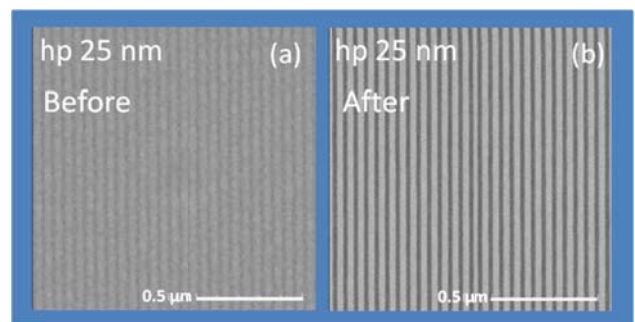


Fig. 7 CD-SEM images of 25-nm-width line and space resist (ZEP520A) pattern (a) before and (b) after the improvement of the grating stage.

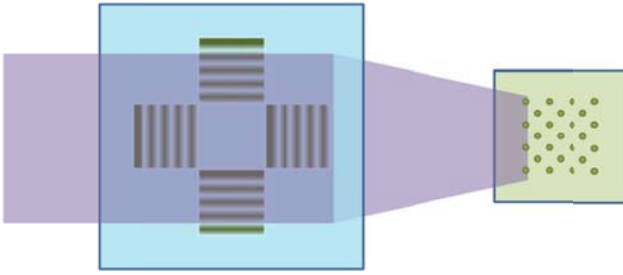


Fig. 8 Hole pattern replication by the four-luminous-flux interference exposure using the four-window diffraction grating.

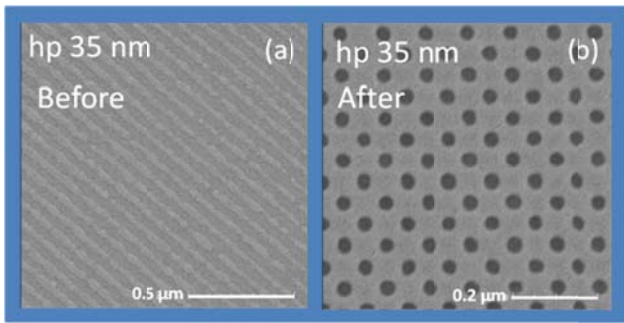


Fig. 9 CD-SEM image of 35-nm-width hole resist (ZEP520A) pattern (a) before and (b) after the vibration improvement.

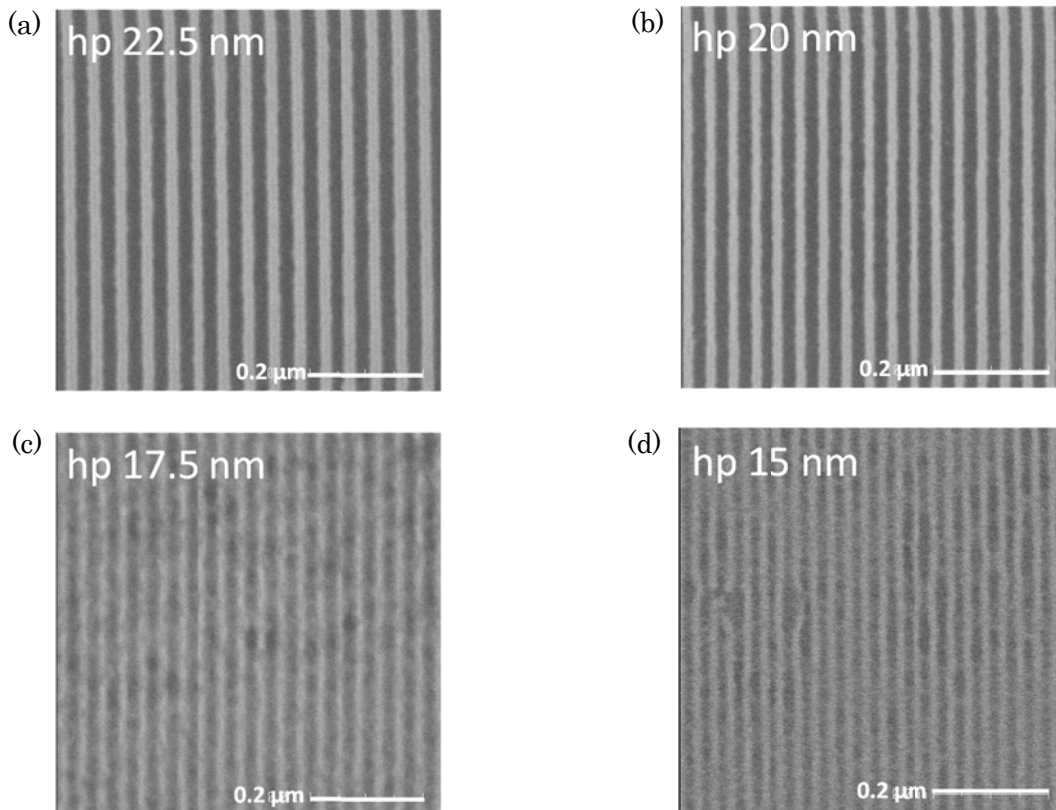


Fig. 10 CD-SEM images of the replicated resist images of the non-chemically amplified negative-tone resist (Inpria); (a) hp 22.5 nm, (b) hp 20 nm, (c) hp 17.5 nm, and (d) hp 15 nm.

3. Results and Discussions

Figure 10 shows the replicated L/S resist pattern of non-chemically amplified resist using the two-luminous-flux interference exposure using the two-window grating. As shown in Fig.10, hp 22.5 nm, hp 20 nm, hp 17.5 nm and hp 15 nm resist pattern were replicated after the vibration improvement. For 15 nm L/S pattern, pattern stripping was observed for the non-chemically amplified resist (Inpria).

As results, it was confirmed that the EUV-IL has a capability to replicate the resist pattern with of 1X nm.

Furthermore, as shown in Figs. 9(b) and 11, by the four-luminous-flux interference exposure using the four-window transmission diffraction grating, hole pattern width of 35 nm and 28 nm resist pattern of ZEP520A resist were replicated. In this case, B by the grating patterns of hp 50 nm and hp 40 nm L/S, hole patterns of hp 35 nm and hp 28 nm were replicated, respectively.

In the near future, the resist pattern replication of 11 nm would be achieved by the fabrication of the transmission diffraction grating pattern of hp 22 nm.

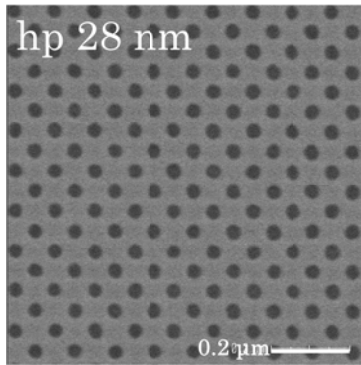


Fig.11 Replicate hole resist pattern (ZEP520A) of hp 28 nm by the four-luminous-flux interference exposure using the four-window diffraction grating.

4. Conclusions

EUV-IL exposure tool was installed in the class 100 clean room at the end station of BL9 beamline in NewSUBARU. The fabrication process of the transmission diffraction grating and the vibration was reduced by the improvement of the grating stage. The two-luminous-flux interference and the four-luminous-flux interference exposures using the EUV-IL exposure tool were used for the resist pattern replication of line and space and hole patterns, respectively. As results, hp 22.5 nm, hp 20 nm, hp 17.5 nm, and hp 15 nm L/S patterns and hp 35 nm and hp 28 nm hole patterns were replicated.

As results, this system can replicated resist for hp 1X nm. Accordingly, the EUV-IL is to open use for the evaluation of the resolution of the EUV resist to accelerate resist development for 1X nm in EUVL

In the near future, for hp 11 nm resist patterning, fabrication of the transmission gratings would be improved and we will realize evaluation of EUV resist for 11 nm.

Acknowledgments

This work was support by the Grant-in-Aid for Scientific Research(B) (22360146), Society for the Promotion of Science, the Ministry of Education, Culture, Sports, Science and Technology, Japan. And also we would like to thank Dr. Andrew Grenville and Dr. Jason Stowers of Inpria Corporation for their support to provide the resist materials.

References

1. H. Kinoshita, K. Kurihara, Y. Ishii and Y. Torii, *J. Vac. Sci. Technol. B* **7** (1989) 1648.
2. ITRS Roadmap 2010 update [<http://www.itrs.net/>].
3. The summaries of the International Symposium of Extreme Ultraviolet Lithography 2010
4. T. Watanabe, Y. Fukushima, H. Shiotani, R.

- Ohnishi, S. Suzuki, H. Kinoshita and S. Yusa, *Jpn. J. Appl. Phys.* **46** (9B) (2007) 6118.
5. T. Watanabe and H. Kinoshita, *J. Photopolym. Sci. Technol.* **21** (2008) 777.
6. H. H. Solak, D. He, W. Li, S. Shingh-Gasson, F. Cerrina, B. H. Sohn, M. Yang, P. Nealey, *Appl. Phys. Lett.* **75** (1999) 2328.
7. Y. Yamaguchi, Y. Fukushima, T. Iguchi, H. Kinoshita T. Harada, and T. Watanabe, *J. Photopolym. Sci. Technol.* **23** (2010) 681.
8. Y. Fukushima, Y. Yamaguchi, T. Kimura, T. Harada, T. Watanabe, and H. Kinoshita, *J. Photopolym. Sci. Technol.* **23** (2010) 673.
9. Y. Fukushima, N. Sakagami, T. Kimura, Y. Kamaji, T. Iguchi, Y. Yamaguchi, M. Tada, T. Harada, T. Watanabe, and H. Kinoshita, *Jpn. J. Appl. Phys.* **49** (2010) 06GD06.
10. S. Hashimoto, A. Ando, M. Nibe, S. Miyamoto, Y. Shoji, Y. Fukuda, T. Tanaka and Y. Goemi, *Nucl. Instrum. Methods Phys. Res., Sect. A* **467** (2001) 141.
11. S. Suzuki, Y. Fukushima, R. Ohnishi, T. Watanabe and H. Kinoshita, *J. Photopolym. Sci. Technol.* **21** (2008) 435.

Imaging of EUV-mask patterns using coherent EUV scatterometry microscope based on coherent diffraction imaging

Tetsuo Harada^{1,2}, Masato Nakasuji^{1,2}, Teruhiko Kimura^{1,2}, Yutaka Nagata^{2,3}, Takeo Watanabe^{1,2}, and Hiroo Kinoshita^{1,2}

1 Center for EUV Lithography, Laboratory of Advanced Science and Technology for Industry, University of Hyogo, Kamigori, Hyogo 678-1205, Japan

2 Core Research for Evolutional Science and Technology, Japan Science and Technology Agency, Kawaguchi, Saitama 332-0012, Japan

3 Laser Technology Laboratory, RIKEN, Wako, Saitama 351-0198, Japan

Abstract

In extreme-ultraviolet (EUV) lithography, defect-free mask production is a critical issue for high-volume manufacturing. For mask inspection and metrology, we have developed a coherent EUV scatterometry microscope (CSM). It is a simple lensless system. An aerial image of the mask pattern is reconstructed with iterative calculation based on coherent diffraction imaging. Periodic patterns, aperiodic patterns and phase structures were reconstructed well by the CSM. A defect in a line-and-space pattern was detected as a diffraction signal. The aerial image of the defect is also reconstructed. This paper demonstrates the capability of the CSM to observe complex diffraction amplitudes directly from the pattern and the defect.

Introduction

In extreme-ultraviolet (EUV) lithography, defect-free mask production is one of the critical issues for high-volume manufacturing. A mask is a master pattern of a semiconductor device, and there must be no defects on the mask. The repair of the defect feature is also important. In EUV lithography, the EUV mask is a reflective type mask, which is different from the transparent type mask used for conventional 193 nm lithography. An EUV mask consists of a glass substrate of 150×150 mm² in size, a Mo/Si multilayer and absorber patterns. A phase structure such as a bump or pit on the substrate, and particles in the multilayers could be printable as a defect. For example, a shallow structure of 1 nm on the surface of a mask substrate causes 53 degrees of large reflection-phase shift in $\lambda=13.5$ nm light, which is the working wavelength of EUV lithography. Also, this buried defect is printable. The illumination of the mask is at an oblique angle of 6 degrees in the present EUV scanner. This causes a shadowing effect because of the height of the absorber pattern, which affects the a critical dimension (CD) value and the reflection phase from the pattern with an azimuth direction relative to the illumination.¹

For defect inspection, ultraviolet (UV) laser^{2,3} and electron-beam⁴ based microscopes have been developed. However,

they inspect only the top surface of the multilayer. The multilayer is sufficiently thick at about 300 nm that small buried structures would not propagate to the surface.⁵ The multilayer could contain printable phase defects despite having a flat top surface. Thus, an actinic (at-wavelength) EUV inspection tool is required to investigate buried defects in the multilayer. SELETE has developed an actinic blank inspection (ABI) tool using Schwarzschild optics and a laboratory source.^{6,7} ABI is a dark-field microscope for specialized defect inspection of blank masks, including detection of phase defects. As a bright-field microscope, we have developed an EUV microscope using Schwarzschild optics and an X-ray zooming tube,^{8,9} which is installed at the NewSUBARU synchrotron facility. It has a high numerical aperture (NA) of 0.3 and a large field with a diameter of 50 μm . This bright-field microscope observes an aerial image of a pattern directly with high resolution. We have also developed a repair method for mask defects using a focused ion beam.^{10,11} The LBNL group has developed an actinic imaging tool (AIT) using a Fresnel zone plate as an optical component.¹² The AIT inspects for pattern defects and phase defects on blank masks.¹³

In general, EUV exposure tools or EUV microscopes illuminate the EUV mask, collect the diffraction from the mask, and project an aerial image. The diffraction from

the mask is important for mask evaluation. However, the aerial image contains not only the mask information but also the properties of the optics. To evaluate the mask alone, we have developed the coherent EUV scatterometry microscope (CSM), which is a lensless type microscope.¹⁴⁻¹⁶ An EUV mask is exposed with coherent EUV light, and the CSM records the EUV diffraction intensity from the pattern directly. The diffraction intensity contains only the amplitude information in the frequency space, where the phase information is missed. This phase information is retrieved via iterative calculations with Fourier transforms and inverse Fourier transforms. Thus, the CSM observes complex diffraction amplitude from the mask. The aerial image of the mask pattern with aberration-free optics is reconstructed by using an inverse Fourier transform. The CSM system is very simple, and is composed of a charge-coupled-device (CCD) camera, a mask stage, and focusing optics, and does not require high-precision optics, or a high precision alignment system. We demonstrated the observation of periodic line-and-space (L/S) and hole patterns as aerial images. We also demonstrated a first method of CD measurement for periodic patterns. An actinic CD value was estimated from the intensity of the 0th and 1st diffraction orders.¹⁵ This method is capable of CD evaluation over the whole mask area.

The image reconstruction method using the diffraction intensity with coherent illumination is called coherent diffraction imaging (CDI). In 1998, Miao, et al. first demonstrated CDI in the hard X-ray region¹⁷, where CDI is a powerful method to achieve a high NA for imaging. Various CDI algorithms have been developed in recent years.^{18,19} Takahashi et al. reported a high resolution of less than 10 nm in three dimensional imaging.²⁰ In this paper, we used ptychographical CDI²¹ to reconstruct an aperiodic structure in the CSM.

Experiment

The CSM system has been installed at the BL-3 beamline of the NewSUBARU synchrotron radiation facility,²² which uses bending magnet as a light source. Two toroidal mirrors collimate the white light to the CSM system. Figures 1 and 2 show a photograph and a schematic view of the

CSM system, respectively. A pinhole with a diameter of 5 μm is exposed to the collimated beam, which reduces the beam diameter. Then, a concave spherical mirror reflects the beam and a planar mirror reflects it onto the EUV mask. The concave mirror projects the pinhole image onto the mask. The radius of the curvature of the concave mirror is 200 mm, and the distance from the pinhole to the concave mirror is 200 mm, which is the same as the distance from the concave mirror to the mask. The mirrors are coated with 40 pairs of Mo/Si multilayers. Diffraction from the mask is recorded using a back-illuminated CCD camera (Roper Scientific MTE-2048B). This camera can operate in a high-vacuum environment. The CCD camera is cooled to a temperature of -50°C . The surface of the CCD is placed parallel to the mask surface. The imaging area is $27.6 \times 27.6 \text{ mm}^2$, which contains 2048×2048 arrays of imaging pixels with an area of $13.5 \times 13.5 \mu\text{m}^2$. The mask x-y stages can move $\pm 75 \text{ mm}$ by using stepping motors to enable observation of the whole area of the EUV mask. The minimum step size of the stage is 100 nm. Two Magnescale LASERSCALER noncontact optical type encoders monitor the movements in the x- and y-directions. The minimum signal step is 34.5 nm. The mask z stage can move 1.5 mm using a stepping motor to focus the exposure light on the mask.

The angle of incidence from normal is 6° on the EUV mask, which is the same as those of the current EUV lithography scanners. The spatial coherence length of the incident beam is about 90 μm , as estimated from the divergence. This is substantially larger than the CSM-field size of 5 μm . The distance from the mask to the CCD camera is about 100 mm, which is equivalent to a numerical aperture of 0.14. The estimated spatial resolution is 50 nm at half pitch.

Figure 3 shows examples of the diffraction images of the CSM, and their scanning electron microscope (SEM) images. Figure 3(a) shows a diffraction image with a 176-nm L/S pattern. The center signal of the white region is directly reflected from the pattern of the 0th diffraction order, where the diffraction fringes of Fraunhofer diffraction are recorded. The two signals other than the center signal are diffractions of the ± 1 st order. Figure 3(b) shows a diffraction image of a hole pattern with a

112-nm half pitch. The center signal of the white region is also directly reflected from the pattern of the 0th diffraction order. The 8 signals other than the center are diffractions of horizontal, vertical and diagonal 1st orders.

The z stage aligns the focusing position of the pinhole image, which is the probe using EUV coherent illumination in the CSM system. Divergence from the pinhole is about 3 mrad, estimated from the Fraunhofer diffraction, and the depth of focus (DOF) of the probe is about 0.8 mm. Thus, re-alignment of the z-axis is not required, even when sample is moved and changed. This long DOF is suitable for quick measurements such as the CD metrology. In a previous paper, we reported the evaluation results of the CD distribution over the whole mask area without focus alignment.¹⁵ The CD uniformity corresponded well with that evaluated using CD-SEM.

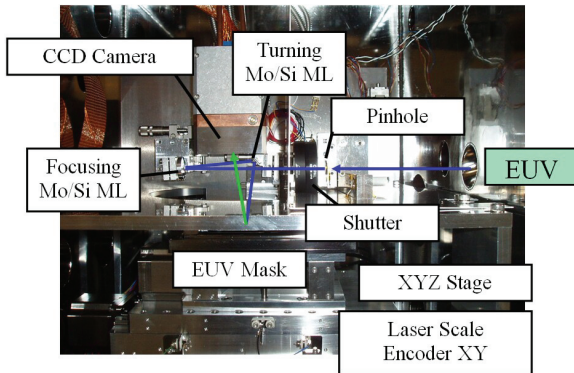


Fig. 1 Photograph of the CSM system. The arrows show the light path of synchrotron radiation. The CCD camera records diffraction from the EUV-mask pattern.

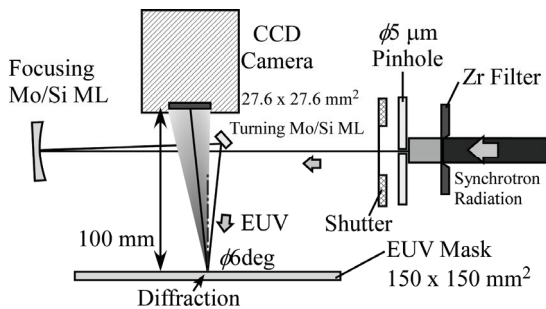


Fig. 2 Schematic view of the CSM system.

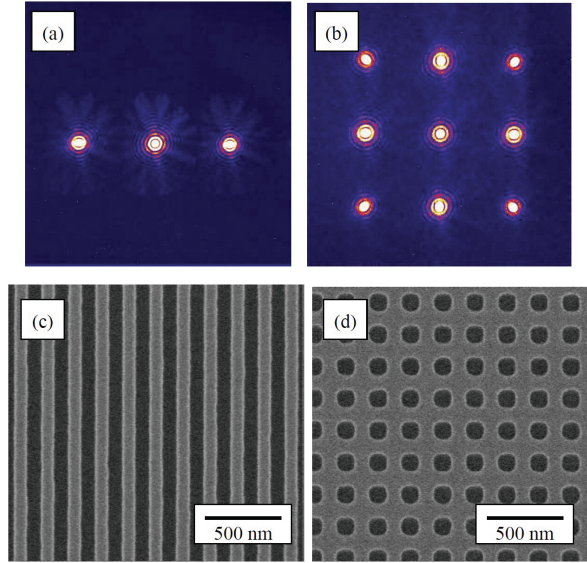


Fig. 3 Diffraction images from the CSM of (a) a 176-nm L/S pattern, and (b) a 112-nm half pitch hole pattern. (c) and (d) are same patterns measured by SEM.

Image Reconstruction Algorithm

We reconstructed an aerial image of EUV mask patterns¹⁵ from the diffraction intensity by using a hybrid-input-output (HIO) algorithm²³, which is widely used for retrieving algorithms of missing phase information in the hard X-ray region. In HIO algorithms, the illumination of the sample is assumed to be a plane wave, where a large area with a small isolated sample is exposed. In the CSM, the probe size of 5 μm is much smaller than a sample mask size of $150 \times 150 \text{ mm}^2$. Because the exposed area size is equal to the probe size, the pattern was not illuminated with a plane wave. The diffraction includes the pattern and the probe information. However, the degraded amplitude at the outside region of the probe made the reconstruction error large. Although the periodic patterns were reconstructed, aperiodic structures were not reconstructed. A suitable method to reconstruct the EUV mask pattern is needed.

Ptychography²¹ is one of the CDI algorithms, in which the sample is illuminated locally with position scanning. Ptychography has been demonstrated to achieve a large field-of-view in the hard X-ray region.²⁴ The probe is scanned to overlap the illumination area, and diffractions are recorded at each probe position. In the iterative calculations of ptychography, revised amounts of

reconstruction are weighted using the probe amplitude. A non-uniform probe distribution is applicable for image reconstruction. Thus, we used ptychographical CDI in the CSM, which consists of a small probe and a large sample.

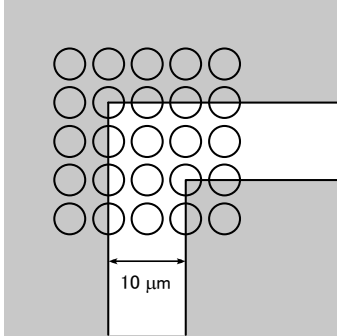


Fig. 4 The schematic of the elbow pattern to reconstruct the illumination probe. The circles indicate the illumination positions.

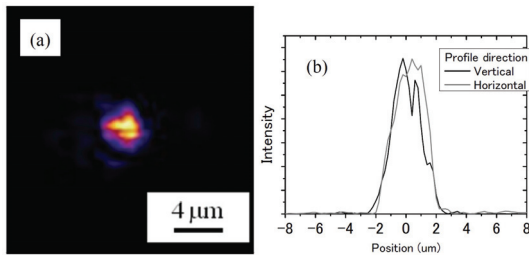


Fig. 5(a) The reconstructed image, and (b) the horizontal and vertical profile of the probe.

EUV Mask Sample

In ptychography, the complex amplitude distribution of a probe is required for phase retrieval. We reconstructed the probe with a prior pattern with a known shape and structure. The known pattern and illuminated position are shown in Figure 4. The pattern which was chosen to reconstruct the two-dimensional profile is an elbow with 10 μm width. The gray color region is covered with an absorber layer of 50 nm thick TaN, and the elbow is a reflective region. The absorption and phase shift were calculated with Henke's optical constant²⁵, where the shadowing effect was ignored. The circle in Figure 4 indicates the illuminated position of the probe. The scanning step was constant at 5 μm in both x and y directions.

The exposure time at each position was

30 s. The elbow was scanned in 5×5 overlapping elbow positions. The illuminated position was measured precisely using the encoders. During exposure, we turned off the encoder to prevent detection of its laser light by the CCD camera. If the stage drifts thermally, the reconstructed image quality would be degraded. In ptychography, precise control of the probe position is crucial for high quality imaging. Thus, we also turn off the stage motor power when the stage has halted to prevent thermal drift.

Figure 5(a) shows the reconstructed image of the probe, and Figure 5(b) shows the horizontal and vertical profiles. The probe size is about 4 μm at full width half maximum. The vertical profile has a notch in the center, and the notch position corresponded with the edge position of the elbow pattern, which indicated that the notch was a probe reconstruction error. There was weak amplitude around the center, and the asymmetric probe shape due to the focusing optics was also well reconstructed. For another reconstruction result for the same probe, the notch shape and the weak amplitude were slightly different.

B. Image reconstruction result

Reconstructed images of the absorber patterns using the CSM are shown in Figure 6. Figure 6(a) is that of a 128-nm L/S pattern, which was illuminated in 5×5 points with a 1 μm step. The probe exposure time at each position was 100 s. The periodic structure of the L/S pattern and the aperiodic structure of the angular shape are well reconstructed. The CCD camera recorded up to 2nd order diffraction from the 128 nm L/S pattern, and the phase of not only the 1st diffraction order but also the 2nd diffraction order was retrieved well using ptychography. In the pattern region, the intensity distribution is not uniform, and would be affected by the reconstructed error of the probe or the scattering noise of the focused optics. Figure 6(b) is a reconstructed image of the crossed line with 2- μm width. The cross shape was well reconstructed. The non-uniformity of the pattern region was also reconstructed, and the left line was blurred. The residual stage drift causes these blurring errors.

Exact and reliable control of the probe is crucial for high-quality imaging in ptychography.²⁶ We are developing a new stage to improve the stage precision, which

is composed of a pulsed-motor stage with laser encoders and a piezo flexure stage with strain-gauge sensors. The pulsed-motor stage moves 150 mm to observe whole area of an EUV mask. The optical encoder is chosen to measure long strokes. The piezo flexure stage moves for ptychographical measurement. The strain-gauge sensor is not an optical type, which could measure the position during exposure. In near future, we intend to observe the EUV mask by ptychographical CDI with this new hybrid stage.

C. Phase structure reconstruction result

We observed a phase structure of bump structures on a glass substrate. The bumps were 5 nm in height, and $0.15 \times 0.5 \text{ mm}^2$ in size. The angular edge of the bump was observed with a scanning position of 4×4 points and step of 1.5 μm . The intended exposure time at each position was 120 s. The observation results for intensity and the phase images are shown in Figure 7. In the intensity image of Figure 7(a), the edge of the phase structure was detected as a dark line due to destructive interference. In the phase image of Figure 7(b), the phase structure was clearly reconstructed. The phase difference was quantitatively estimated to be 0.84 waves, which is different from the calculated value of 0.74 waves by virtue of the height. This difference could be caused by thickness errors for the bump or for the multilayer deposition. Thus, the CSM can observe the phase, which is very important for the EUV-mask evaluation.

D. Defect reconstruction result

We also observed an amplitude defect in the absorber patterns. Figure 8(a) shows the SEM image of the defect, which is a line defect in an 88-nm L/S pattern. This defect line is 30 nm narrower than the other lines. The defect size varied from 2 nm to 40 nm, in which the width of the line was ranging from 44 to 86 nm. Figure 8(b) shows the diffraction image from the defect and the L/S patterns. The exposure time was 100 s. The diffraction from the L/S pattern was similar to that shown in Figure 3(a), and diffraction from the defect was clearly recorded as a line diffraction in the lateral direction. To decrease the shadowing effect, the plane of incidence of the probe was chosen to be parallel to the lines. The line diffraction has symmetrical intensity around the 0th diffraction order, which shows that the phase distribution of the

defect line is symmetrical. When the plane was chosen to be perpendicular to the line, the diffraction intensity was asymmetrical. The diffraction phase from a defect depends on the azimuth of the probe, and the CSM can observe the phase effect. The defect signal for a defect size of up to 10-nm in width was detected at the diffraction image. Thus, the CSM detects the defect as the difference of the calculated diffraction signal without reconstruction of the aerial image. Also, this CSM inspection using the diffraction image quickly detects the existence of defects in the field of view. Image reconstruction is still needed to detect the defect position. Theoretical detection limits for the defect sizes depend on the signal-to-noise ratio of the detector noise, the source brightness and the substrate roughness. The substrate roughness generates speckle noise on the signal. If the detector noise is at imaginary zero, then the detection limit is estimated to about $\phi 30\text{-nm}$ with a current EUV mask.

Figure 8(c) shows the image reconstruction result for the line defect by ptychographical CDI. The defect was illuminated at 7×2 points with a 1 μm step. There is a bright line from the defect in the L/S pattern. However, the periodic L/S pattern around the defect has a blurred shape due to the noise in the image reconstruction. We filtered out diffraction from the periodic L/S signal and reconstructed the aerial image, as shown in Figure 8(d). The defect was clearly detected without a periodic structure. Thus, the CSM can inspect the defect positions by using ptychographical CDI.

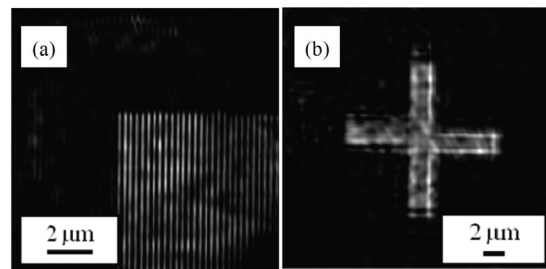


Fig. 6 Reconstructed images of absorber patterns using the CSM. (a) 128-nm L/S pattern. (b) 2- μm width crossed lines.

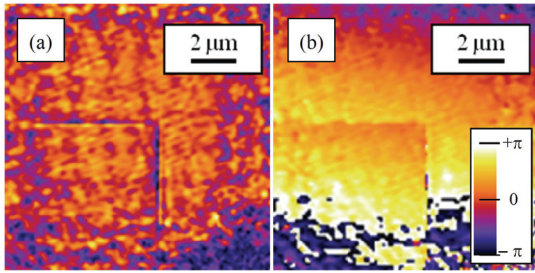


Fig. 7 Reconstructed image of the phase structure of (a) intensity, and (b) phase distribution.

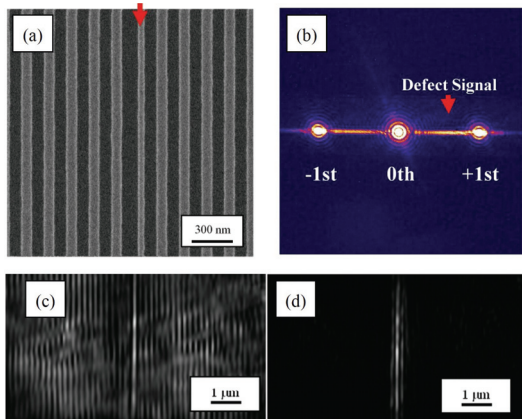


Fig. 8 (a) SEM image and (b) diffraction image of the 30-nm size line defect. (c) Reconstructed image, and (d) that with the periodic signal filtered out.

Conclusions

We have developed the CSM for EUV mask inspection and metrology. The CSM is an actinic and lensless type microscope, which records diffraction from an EUV mask directly. The EUV mask patterns were observed using ptychographical CDI. Ptychography is a suitable CDI method for the CSM, and consists of a small probe and a large sample. The aerial images of the periodic L/S structure and the aperiodic angular edge structure were well reconstructed. The amplitude and phase images of the bump on the substrate were reconstructed quantitatively. Also, a line defect with 10-nm width was detected as a diffraction image, and the defect position was also inspected in the reconstructed image. Thus, it is demonstrated that the CSM can observe complex diffraction amplitudes in the EUV mask pattern.

In the near future, we intend to install a laboratory EUV laser source of high-order harmonic generation²⁷ for practical inspection. The power will be 1,000 times stronger than that of our present source, which wastes most of the light to achieve a high spatial coherence.

References

- [1] K. Otaki, *Jpn. J. Appl. Phys.* **39**, 6819 (2000).
- [2] W. Cho, P. A. Kerney, E. M. Gullikson, A. Jia, T. Tamura, A. Tajima, H. Kusunose, C. U. Jeon, *Proc. SPIE* **6517**, 65170D (2007).
- [3] S. Stokowski, J. Glasser, G. Inderhees, P. Sankuratri, *SPIE Proc.* **7636**, 76360Z (2010).
- [4] T. Shinomura, Y. Inazuki, T. Abe, T. Takikawa, H. Mohri, N. Hayashi, F. Wang, L. Ma, Y. Zhao, C. Kuan, H. Xiao, J. Jau, *SPIE Proc.* **7823**, 78232B (2010).
- [5] M. Sugawara, I. Nishiyama, K. Motai, J. Cullins, *Jpn. J. Appl. Phys.* **45**, 9044 (2006).
- [6] T. Terasawa, Y. Tezuka, M. Ito, T. Tomie, *SPIE Proc.* **5446**, 804 (2004).
- [7] T. Terasawa, T. Yamane, T. Tanaka, O. Suga, T. Tomie, *Jpn. J. Appl. Phys.* **49**, 06GD02 (2010).
- [8] K. Hamamoto, Y. Tanaka, T. Yoshizumi, N. Hosokawa, N. Sakaya, M. Hosoya, T. Shoki, T. Watanabe, H. Kinoshita, *Jpn. J. Appl. Phys.* **45**, 5378 (2006).
- [9] K. Takase, Y. Kamaji, N. Sakagami, T. Iguchi, M. Tada, Y. Yamaguchi, Y. Fukushima, T. Harada, T. Watanabe, H. Kinoshita, *Jpn. J. Appl. Phys.* **49**, 06GD07 (2010).
- [10] T. Amano, N. Takagi, H. Shigemura, T. Terasawa, O. Suga, K. Shiina, F. Aramaki, A. Yasaka, Y. Inazuki, N. Hayashi, *SPIE Proc.* **7823**, 782323 (2010).
- [11] A. Barty, Y. Liu, E. Gullikson, J. S. Taylor, O. Wood, *Proc. SPIE* **5751**, 651 (2005).
- [12] K. A. Goldberg, P. P. Naulleau, A. Barty, S. B. Rekawa, C. D. Kemp, R. F. Gunion, F. Salmassi, E. M. Gullikson, E. H. Anderson, H. Han, *Proc. SPIE* **6730**, 67305E (2007).
- [13] I. Mochi, K. A. Goldberg, B. La Fontaine, A. Tchikoulaeva, C. Holfeld, *SPIE Proc.* **7636**, 76361A (2010).
- [14] T. Harada, J. Kishimoto, T. Watanabe, H. Kinoshita, D.G. Lee, *J. Vac. Sci. Technol. B* **27**, 3203 (2009).
- [15] T. Harada, M. Nakasuji, M. Tada, Y. Nagata, T. Watanabe, H. Kinoshita, *Jpn. J. Appl. Phys.* **50**, 06GB03 (2011).
- [16] T. Harada, M. Nakasuji, T. Kimura, Y. Nagata, T. Watanabe, H. Kinoshita, *Proc. SPIE* **8081**, 80810K

(2011).

[17] J. Miao, D. Sayre, H. N. Chapman, *J. Opt. Soc. Am. A* **15**, 1662 (1998).

[18] B. Abbey, K.A. Nugent, G.J. Williams, J.N. Clark, A.G. Peele, M.A. Pfeifer, M.D. Jonge, I. McNulty, *Nature Physics* **4**, 394 (2008).

[19] M. Guizar-Sicairos, J.R. Fienup, *Opt. Lett.* **33**, 2668 (2008).

[20] Y. Takahashi, N. Zettsu, Y. Nishino, R. Tsutsumi, E. Matsubara, T. Ishikawa, K. Yamauchi, *Nano. Lett.* **2010**, 1922 (2010).

[21] J. M. Rodenburg, H. M. L. Faulkner, *Appl. Phys. Lett.* **85**, 4795 (2004).

[22] T. Watanabe, T. Haga, M. Niibe, H. Kinoshita, *J. Synchrotron Rad.* **5**, 1149 (1998).

[23] J.R. Fienup, *Appl. Opt.* **21**, 2758 (1982).

[24] J. M. Rodenburg, A. C. Hurst, A. G. Cullis, B. R. Dobson, F. Pfeiffer, O. Bunk, C. David, K. Jefimovs, I. Johnson, *Phys. Rev. Lett.* **98**, 034801 (2007).

[25] B. L. Henke, E. M. Gullikson, and J. C. Davis, *Atomic Data and Nuclear Data Tables* **54**, 181-342 (1993).

[26] Y. Takahashi, A. Suzuki, N. Zettsu, Y. Kohmura, Y. Senba, H. Ohashi, K. Yamauchi, T. Ishikawa, *Physical Review B* **83**, 214109 (2011).

[27] E. J. Takahashi, Y. Nabekawa, K. Midorikawa, *Appl. Phys. Lett.* **84**, 4 (2004).

Critical Dimension Measurement of an Extreme-Ultraviolet Mask Utilizing Coherent Extreme-Ultraviolet Scatterometry Microscope at NewSUBARU

Tetsuo Harada^{1,2}, Masato Nakasuji^{1,2}, Masaki Tada^{1,2}, Yutaka Nagata^{2,3}, Takeo Watanabe^{1,2}, and Hiroo Kinoshita^{1,2}

1 Center for EUV Lithography, Laboratory of Advanced Science and Technology for Industry, University of Hyogo, Kamigori, Hyogo 678-1205, Japan

2 Core Research for Evolutional Science and Technology, Japan Science and Technology Agency, Kawaguchi, Saitama 332-0012, Japan

3 Laser Technology Laboratory, RIKEN, Wako, Saitama 351-0198, Japan

Abstract

We have developed a coherent extreme ultraviolet scatterometry microscope (CSM) for actinic inspection and metrology of an extreme ultraviolet (EUV) mask. It was installed at the BL-3 beamline of the NewSUBARU synchrotron radiation facility. The CSM is a lens-less system with no objective, and aerial images and critical dimension (CD) values are estimated using the recorded diffraction image. A method of measuring CD values by reconstruction of aerial images using diffraction intensity has been developed. A repeatability of 0.3 nm (3σ) with a high precision is achieved with the actinic method. We also evaluate the CD uniformity of the 88 nm lines-and-spaces patterns on the finished EUV mask, which corresponds well with that obtained by critical-dimension scanning electron microscopy (CD-SEM) results.

Introduction

In extreme ultraviolet (EUV) lithography, the mask is of the reflective type composed of a glass substrate of $150 \times 150 \text{ mm}^2$ in size, a Mo/Si multilayer, and absorber patterns. EUV mask fabrication has specific issues in EUV lithography such as phase defects of the multilayer and the shadowing effect due to the oblique illumination.¹⁻⁵⁾ Thus, EUV inspection and metrology are required to evaluate the actinic feature of defect printability and critical dimension (CD) values. A poor CD uniformity influences the electric properties of semiconductor devices. On the international technology roadmap for semiconductors,⁶⁾ the required CD uniformity is 3.3 nm (3σ), and the acceptable uncertainty of CD metrology tool is 0.69 nm (3σ) for dense lines of the 22 nm node. The conventional tool of CD metrology is critical-dimension scanning electron microscopy (CD-SEM). In the process of mask-pattern writing by electron beam lithography (EBL), the proximity effect could make the CD distribution non-uniform. EBL controls exposure dose to compensate for the effect. Thus, the CD evaluation of the whole mask area is required to detect local CD errors. However, mask-pattern CDs for about 100 points are measured typically by CD-SEM, because only a limited size can be observed by CD-SEM and it takes a long time to observe the whole mask area.

We have developed a coherent EUV scatterometry microscope (CSM), which is a lens-less system for actinic inspection and metrology.⁷⁾ For CSM, the mask is exposed to a coherent EUV light. A charge-coupled-device (CCD) camera records diffraction and scattering from the mask directly, which contains amplitude information in the frequency space. CD is estimated using diffraction intensity, and an aerial image of the pattern is reconstructed with iterative calculation. We observed line patterns and hole patterns, and the aerial images of these patterns were well reconstructed. This paper focuses on an actinic and quick CD-measurement method using diffraction intensity, and the results of evaluation of CD uniformity for the finished EUV mask.

Design of the Coherent EUV Scatterometry Microscope

The CSM system has been installed at the BL-3 beamline of the NewSUBARU synchrotron radiation facility,⁸⁾ which employed a bending magnet as a light source. Two toroidal mirrors collimate the white light to the CSM system. Figures 1 and 2 show a photograph and a schematic view of the CSM system, respectively. A pinhole with a diameter of 5 μm is exposed to the collimated beam, which reduces the beam diameter. Then, a concave spherical mirror reflects the beam and a planar

mirror reflects it onto an EUV mask. The concave mirror projects the pinhole image onto the mask. The radius of the curvature of the concave mirror is 160 mm, and distance from the pinhole to the concave mirror is 160 mm, which is the same as the distance from the concave mirror to the mask. The mirrors are coated with 40 pairs of Mo/Si multilayers. Diffractions from the mask are recorded with a back-illuminated CCD (Roper Scientific MTE-2048B) camera. This camera can operate in a high-vacuum environment. The CCD camera is cooled to a temperature of ± 50 °C. The surface of the CCD is placed parallel to the surface of the mask. The imaging area is 27.6×27.6 mm², which contains imaging pixels of 2048 \times 2048 arrays with an area of 13.5×13.5 μ m². The mask x-y stages can move ± 75 mm through stepping motors to enable observation of the whole area of the EUV mask. The minimum step size of the stage is 100 nm. Two encoders of Magnescale LASERSCALER of the noncontact optical type monitor the movements in the x- and y-directions. The minimum signal step is 34.5 nm. The mask z stage can move 1.5 mm through a stepping motor to focus the exposure light on the mask.

The angle of incidence on the EUV mask from normal is 6°, which is the same as those of the present EUV lithography scanners. Owing to the oblique illumination of the exposure tools, CD includes the shadowing effects caused by absorber pattern height. The shadowing effect causes a horizontal-vertical bias, which means a CD value difference between horizontal and vertical line-and-space (L/S) directions.¹⁾ Thus, CSM can evaluate actinic CD value including the shadowing effect. The spatial coherence length of the incident beam is 18 μ m, as estimated from the divergence. This is substantially larger than the CSM-field size of 5 μ m. The distance from the mask to the CCD camera is about 100 mm, which is equivalent to a numerical aperture of 0.14. The estimated spatial resolution is 50 nm at half pitch. Figure 3 shows an example of a diffraction image recorded using the CCD camera. The sample was a L/S pattern with a 176 nm pitch. The center signal of the white region is directly reflected from the pattern of the 0th diffraction order, where diffraction fringes of Fraunhofer diffraction are recorded. The two signals besides the center are diffractions of the ± 1 st order.

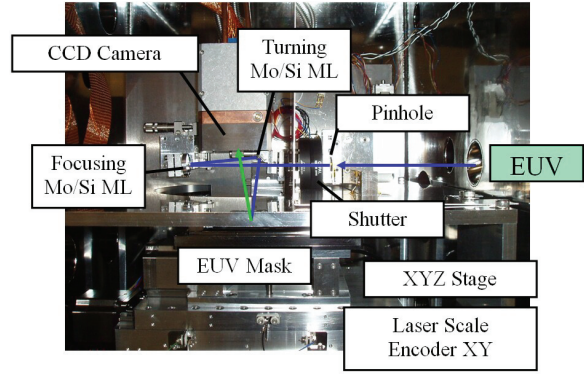


Fig. 1 Photograph of the CSM system. The arrows show the light path of synchrotron radiation. The CCD camera records diffraction from the EUV-mask pattern.

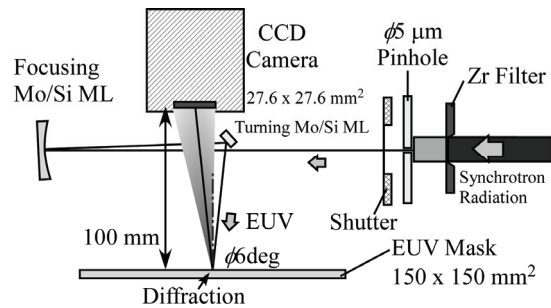


Fig. 2 Schematic view of the CSM system.

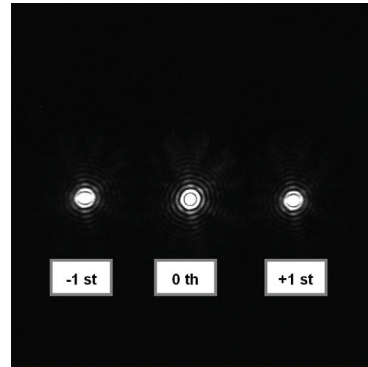


Fig. 3 Diffraction pattern image recorded with the CCD camera from an L/S pattern with 176 nm pitch.

CD Analysis

We develop a method to measure the CD value based on the scalar diffraction theory. At the exposure tool, an EUV mask is illuminated, and diffractions from the mask pattern are generated. The projection optics propagates the diffractions from a mask to the focal plane as aerial images on a wafer. In this study, an aberration-free system is

assumed, since the wave front error of the projection should be very small in lithography. The imaging optics do not add wave front error to the diffraction from the mask, but filter the diffraction with the pupil. At CSM, the CCD camera records diffraction intensity. If the phase of the diffraction is known, aerial images can be calculated. For the L/S pattern, aerial images can be calculated using CSM data and the phases of the diffraction orders.

For small-pitch patterns, only a few diffraction orders make it through the imaging optics. Near the resolution limit, only the 0th and the 1st diffraction orders are transmitted through the imaging optics. For imaging with the 0th and 1st diffraction orders, an intensity profile of an aerial image can be calculated using the diffraction intensities. The aerial image is generated by the interference of the three diffracted waves of the 0th and ± 1 st orders. The phase difference between the 0th and 1st diffraction orders causes defocus, which can be ignored at the in-focus position. The phase difference between the +1st and -1st diffraction orders causes defocus and position shift of the aerial image. Thus, the intensity profile of the aerial image at the in-focus position can be calculated by the diffraction intensities of the 0th and ± 1 st diffraction orders. The 0th diffraction order means the bias component of the interference, and the 1st diffraction order means the modulation component. We describe the intensity profile of the L/S aerial image as follows:

$$I(x) = \left| u_0 + u_{-1} \exp\left(\frac{-2\pi x}{p} i\right) + u_{+1} \exp\left(\frac{+2\pi x}{p} i\right) \right|^2 \quad (1)$$

The amplitudes of the 0th and ± 1 st diffraction order are denoted as u_0 , u_{+1} and u_{-1} , respectively. p means the pitch of the L/S pattern, and x means the position in the image plane. Calculated intensity profiles of L/S patterns with 176 nm pitch (22 nm node) are shown in Fig. 4. The TaN-absorber width was varied at 64 nm (black dashed line), 88 nm (black line, 1:1 L/S ratio), and 112 nm (gray line), which is equal to CD value for CD-SEM. The diffraction intensities of these patterns are calculated on the basis of the scalar diffraction theory. The intensity profiles of the aerial images shown in Fig. 4 are calculated using eq. (1). As shown in Fig. 4,

the profile with a wide reflection area (small CD value) has a high peak intensity. The other profile with narrow area (large CD value) has a low intensity.

On the wafer of the image plane, the aerial image interacts with the photoresist to create a binary structure in ideal. The width of the resist pattern is influenced by resist sensitivity, dose, intensity profile, and the resist process. For simple evaluation, we apply a constant-intensity threshold to the aerial image profile, which determines the image CD value.⁹⁾ Thus, the image CD corresponds to the reflection region as the space width in CD-SEM results, not to the CD value of the absorber region. For example, the threshold is determined to make the image CD value 88 nm for the CD 88 nm L/S pattern (L/S ratio of 1:1). The same threshold determines the image CD with other profiles. As shown in Fig. 4, the image CD values are 101.3 and 74.9 nm for the patterns that have absorber widths of 64 and 112 nm, respectively.

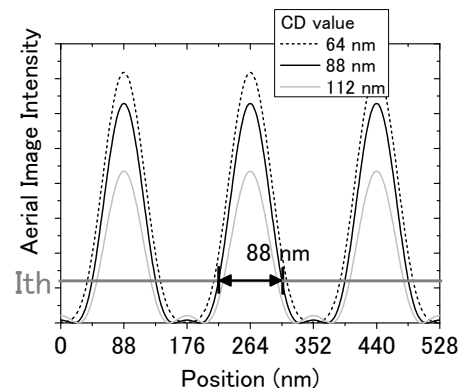


Fig. 4 Calculated intensity profiles of 88 nm L/S patterns, which have varied absorber widths of 64, 88, and 112 nm.

EUV Mask Sample

The sample EUV mask is a finished mask (Dai Nippon Printing), which is a glass substrate with 40 periods of the Mo/Si multilayer structure. The top layer of the multilayer is a 11-nm-thick silicon capping layer. The absorber is composed of a 10-nm-thick CrN layer (buffer layer) and a 70-nm-thick tantalum-based layer.

Various types of L/S pattern are located on the mask. The L/S patterns have five L/S ratios of 1:1, 1:2, 2:1, 1:4, and 4:1. Twenty-two types of the vertical L/S pattern, horizontal L/S pattern, wiring pattern and bit-line pattern are located. Each pattern type has ten pattern widths ranging from

80 to 600 nm, which are equivalent to the patterns on the wafer with widths from 20 to 150 nm. Therefore, the number of patterned areas in one region is 220. Each patterned area is $35 \times 35 \mu\text{m}^2$. The areas are located with 50 μm steps. One pattern group has seven pattern regions with various mask biases ranging from -12 to +12 nm. 21×21 pattern groups are located on the EUV mask with 6.5 mm steps. In this study, we measured the L/S patterns that have 88 nm hp, 1:1 ratio, and 0 nm mask bias. The incidence plane of EUV illumination was parallel to the L/S direction; this configuration caused no shadowing effect. We evaluated the image CD uniformity of the 10×9 patterns with 13 mm steps. The distribution was also measured by CD-SEM (Vistec LWM9000), which has an average CD value of 91.9 nm and a uniformity of 7.7 nm (3σ). The magnification was $75,000\times$. The acceleration voltage was 1,500 V. The number of signal integrations was 128. The field of view was $1.9 \times 1.9 \mu\text{m}^2$. Figure 5 shows a CD-SEM image of a 88 nm L/S pattern.

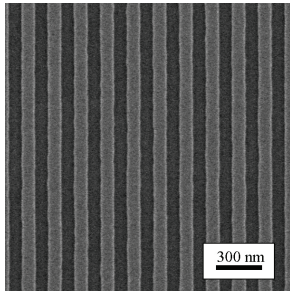


Fig. 5 CD-SEM image of an 88 nm L/S pattern.

Results and Discussion

The intensity threshold discussed in §3 is determined by a reference L/S pattern that has an almost 88 nm CD value of 1:1 L/S ratio. An aerial image is calculated using diffraction intensities from the reference pattern. The threshold is determined to make the reference image CD value 88 nm. The exposure time was 20 s. We determine the diffraction intensity of each order as the integral of CCD signals that distribute around the diffraction center within $\pm 0.5^\circ$.

First, we evaluated the image CD profile in one pattern area of $35 \times 35 \mu\text{m}^2$. The profile was not uniform, where the edge region had a 4 nm larger image CD value

than the center. Thus, the absorber width at the center region is smaller than that at the edge, which is caused by the proximity effect of the EBL process. The backscattering of the electrons at the pattern edge affects the center position as the bias component, and makes the resist width small. The radius of a uniform region of the image CD within 0.1 nm is less than 2.5 μm from the center. CSM can measure the uniform center region of $35 \times 35 \mu\text{m}^2$ in size, since the alignment precision of the stage position is less than 1 μm .

Next, we evaluated the repeatability of image CD. The repeatability for the 88 nm L/S pattern was measured at the same position 20 times. The image CD values are shown in Fig. 6 (black points). The fluctuation is large, about 1.1 nm (3σ). However, all the diffraction intensities of the 0th and ± 1 st orders fluctuated at the same ratio. Thus, the image CD fluctuation is caused by the fluctuation of exposure-light dose. In this study, we compensate for the dose fluctuation using the intensity ratio of the 0th and 1st diffraction orders. If the reflectivity of the mask is uniform in the whole area, then the intensity ratio depends on the CD value only. Image CD value can be calculated using intensity ratio. In practice, we calculate diffraction intensity from the L/S pattern with various absorber widths, which has a rectangular pattern and designed absorber thickness. Image CD value is determined by comparing between the experimental and calculated intensity ratios. The image CD fluctuation with the dose compensation is shown in Fig. 6 (gray points), and the repeatability is greatly improved from 1.1 nm to 0.3 nm (3σ).

The exposure time dependence of repeatability for 20 measurements is also shown in Fig. 7, where the time is varied from 1 to 100 s. The repeatability is low at 2 nm (3σ) for 1 s, which is improved with increasing time; 0.3 nm for 20 s and 0.13 nm for 100 s. The image CD value is markedly stable even for different and long exposure times. We choose 20 s for evaluating image CD uniformity, considering the balance between exposure time and repeatability. The dark current noise of the CCD camera is about 0.02 electrons/s/pixel, and the readout noise is about 5.0 electrons/pixel at 100 Hz. Since the readout noise is dominant with less than 250 s of exposure time, the

repeatability is limited by the signal-to-noise ratio of exposure dose and readout noise. Thus, the low repeatability of the short exposure time will be improved using a large dose. The high-brightness source of coherent EUV provides high-speed and high-precision measurement of image CD by CSM.

The results of evaluation of image CD uniformity of the EUV mask are shown in Fig. 8. For this measurement, we did only position alignment to move the mask. The gray contrast shows the image CD value. The horizontal and the vertical axes indicate the x and y positions of the mask, respectively. The image CD values of the left side region are larger than those of the right side. This distribution is almost the same as that of CD-SEM results. To compare with the CD-SEM results, the relationship between CSM and CD-SEM results is shown in Fig. 9. The vertical axis indicates the image CD value obtained by CSM, and the horizontal axis indicates the space width obtained by CD-SEM. Since the relationship is almost linear, CSM results correspond well to CD-SEM results. The deviation of CSM results from CD-SEM results is approximately 1.4 nm (3σ), which is comparable to the uncertainty of the CD-SEM results in this study. The gradient of the relationship is 0.7, which means that the image CD is not equal to the space width obtained by CD-SEM. Thus, CSM can evaluate the actinic CD uniformity of the whole mask area with high speed and no complex alignment.

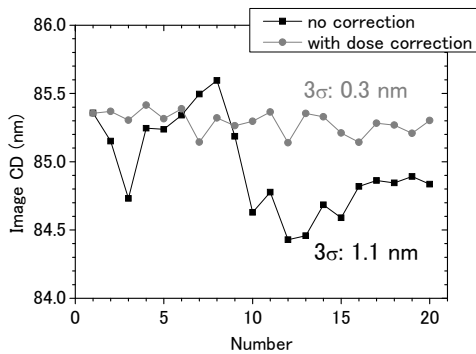


Fig. 6 CD value fluctuation measured by CSM 20 times at the same position of an 88 nm L/S pattern, which shows repeatability of CSM. The two data series show measurements with and without dose correction.

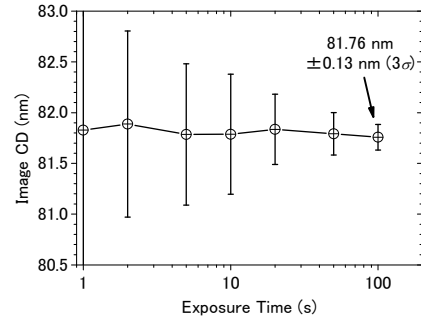


Fig. 7 Repeatability of CSM at various exposure times from 1 to 100 s. The error bar means the three-sigma deviation from the average.

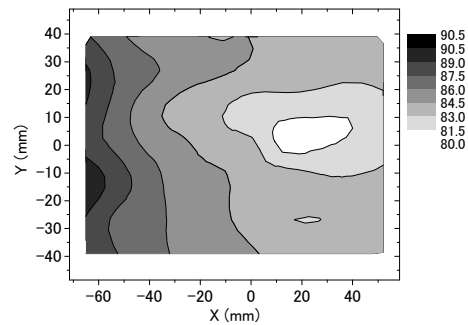


Fig. 8 Results of evaluation of image CD uniformity for CSM. The number of sampling points is 10×9 , where the 88 nm L/S patterns fabricated by the same process are located with 13 mm steps.

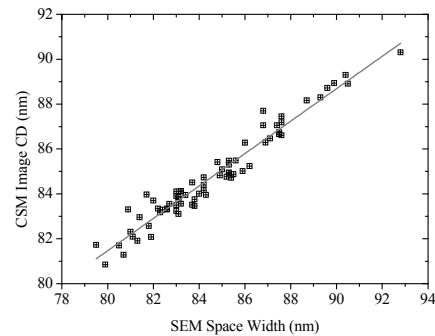


Fig. 9 CD value relationship measured using CSM and by CD-SEM of the EUV mask.

Conclusions

We have developed the coherent EUV scatterometry microscope for actinic inspection and metrology of the EUV mask. The CD measurement method by estimation of the aerial image using the diffraction intensities has been developed. A high repeatability of 0.3 nm (3σ) is achieved. We evaluate the CD uniformity of the 88 nm L/S pattern, which corresponds well to that obtained by CD-SEM.

In the near future, we will install a laboratory EUV laser source of high-order harmonic generation (HHG) for practical inspection. The power will be 1000 times greater than that of our present source, which wastes most of the light to achieve a high spatial coherence. The target scanning time for the whole mask is less than 90 min.

References

- [1] K. Otaki: Jpn. J. Appl. Phys. **39** (2000) 6819.
- [2] T. Terasawa, T. Yamane, T. Tanaka, T. Iwasaki, O. Suga, and T. Tomie: Jpn. J. Appl. Phys. **48** (2009) 06FA04.
- [3] E. M. Gullikson, C. Cerjan, D. G. Stearns, P. B. Mirkarimi, and D. W. Sweeney: J. Vac. Sci. Technol. B **20** (2002) 81.
- [4] K. A. Goldberg, I. Mochi, and P. Naulleau: J. Vac. Sci. Technol. B **27** (2009) 2916.
- [5] Y. Kamaji, K. Takase, T. Yoshizumi, T. Sugiyama, T. Uno, T. Watanabe, and H. Kinoshita: Jpn. J. Appl. Phys. **48** (2009) 06FA07.
- [6] Semiconductor Industry Association: International Technology Roadmap for Semiconductors: 2009 Lithography (International SEMATECH, Austin, TX, 2009) .
- [7] T. Harada, J. Kishimoto, T. Watanabe, H. Kinoshita, and D.G. Lee: J. Vac. Sci. Technol. B **27** (2009) 3203.
- [8] T. Watanabe, T. Haga, M. Niibe, and H. Kinoshita: J. Synchrotron Rad. **5** (1998) 1149.
- [9] Chris Mack: Fundamental Principles of Optical Lithography (Wiley, Chichester, U.K., 2008) Chap. 3.8.

Fabrication of Carbon X-ray Mask for High Aspect Ratio X-ray Diffraction Grating

Daiji Noda¹, Atsushi Tokuoka¹, Megumi Katori², Yasuto Minamiyama², and Tadashi Hattori¹

¹Laboratory of Advanced Science and Technology for Industry, University of Hyogo,

²Nanocreate Co., Ltd.

Abstract

For X-ray lithography, the accuracy of the fabricated structure depends largely on the accuracy of the X-ray mask. Conventionally, a resin material is used for the support membrane for large area X-ray masks. However, resin membranes have the disadvantage that they can sag after several cycles of X-ray exposure due to the heat generated by the X-rays. Therefore, we proposed thin carbon wafers for the membrane material because carbon has an extremely small thermal expansion coefficient. This new type of X-ray mask is very easy to process, and it is expected that it will lead to more precise X-ray masks. We succeeded in fabricating X-ray masks with large effective areas up to $100 \times 100 \text{ mm}^2$ on carbon membranes. Au, with a height of about $4 \mu\text{m}$ and a pitch of $5.3 \mu\text{m}$, was used as the X-ray absorber material.

Introduction

X-ray lithography technique is one of the most promising technologies for fabricating micrometer level three-dimensional microstructures. This is used a highly directional synchrotron radiation light, which makes a process suitable for high accuracy, high aspect ratio microstructure fabrication. For X-ray lithography, the accuracy of the fabricated structure depends largely on the accuracy of the X-ray mask pattern, that is, a bottom surface and side wall configurations of structure. Since, in X-ray lithography, the radiation is highly directional, a micro-fabrication technology that produces un-tapered and high aspect ratio highly absorbent structures on a low absorbent membrane is required.

X-ray mask generally consists of X-ray absorber, membrane and frame. An effective area of X-ray mask should be as large as possible to improve production efficiency and reduce cost. Here, we focus on the membrane material. The membrane material should have high transmittance, since lithography requires high contrast between absorber and blank pattern. And, it is also important in forming a high accuracy mask pattern. In order to having these requirements, a resin material is conventionally used for a membrane of large effective area pattern of X-ray masks [1-2]. However, resin membrane has a great disadvantage, that is, sag due to X-ray derived heat after several cycles of X-ray exposure. In this study, we have proposed that carbon wafer was used as membrane material because carbon has an extremely small thermal expansion coefficient [3].

Fabrication of carbon X-ray mask

The conventional X-ray mask fabrication process using Si wafer has bonding process of a frame and etching process of Si wafer because the X-ray transmittance is not good. On the other hand, the newly X-ray mask fabrication process is very easy, as shown in Fig. 1. The thickness of carbon wafer was used at $200 \mu\text{m}$ to ensure necessary transmittance and strength. Therefore, thin carbon wafer also has role of frame. Thus, bonding and etching processes was disused in conventional fabrication process.

Fabrication of X-ray grating

X-ray radiographic imaging techniques have

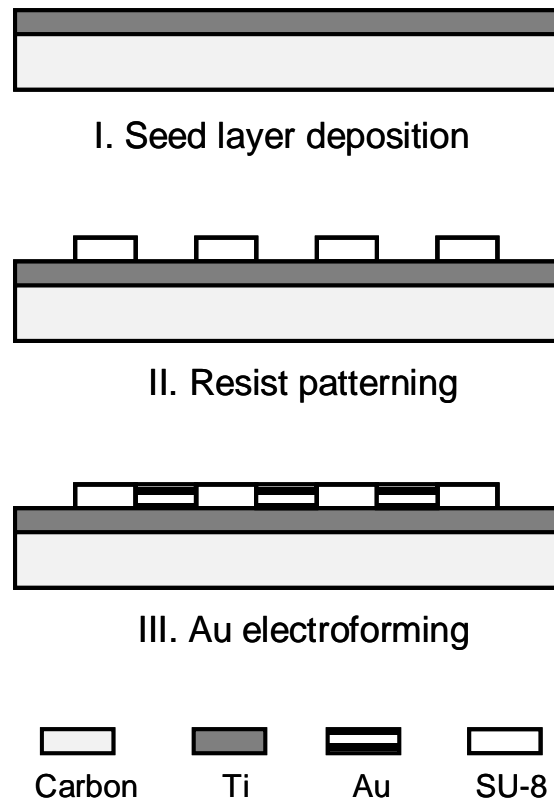


Fig. 1: New fabrication process of X-ray mask.

been applied in many fields. Previously, we proposed a method for X-ray phase imaging using X-ray Talbot interferometry [4], which requires the use of X-ray gratings with high aspect ratio structures. Therefore, we have fabricated a new X-ray mask on 6 inch carbon wafer having 1:1 line and space patterns at 5.3 μm intervals, with an Au absorber height of 4 μm . This mask has a large effective area of 100 \times 100 mm^2 , as shown in Fig. 2.

For the deep X-ray lithography, we used NewSUBARU, which is the synchrotron radiation facility owned by our university. Beamline 2 has the potential to pattern large areas up to A4 size with highly uniform pattern thickness. Using the newly fabricated X-ray mask, we have fabricated microstructure patterns with 35 μm thick photoresist by X-ray lithography technique. Figure 3 shows a picture of an X-ray grating pattern on a 6 inch Si substrate made using the new carbon X-ray mask. The structure of the patterned photoresist over the whole area is excellent.

For the X-ray diffraction grating, gold was formed between the photoresist structure by electroforming.

Conclusions

The purpose of this research was to develop an X-ray mask to be used in the production of X-ray gratings for phase tomography imaging with an X-ray Talbot interferometer. A conventional X-ray mask was fabricated using a large area resin membrane. However, the patterned area became warped after several X-ray exposures. As a result, we proposed and fabricated a new X-ray mask using a carbon wafer to serve as the support membrane. This overcame the problem of thermal deformation during X-ray exposure that usually occurs when using masks based on resin membranes.

We successfully fabricated a large area X-ray mask on a thin carbon wafer with Au lines with a pitch of 5.3 μm and a height of about 4 μm covering a large effective area of 100 \times 100 mm^2 . Using this new carbon X-ray mask, large area X-ray gratings were fabricated on 6-inch Si substrates.

These results give us confidence that the spatial resolution of phase tomography imaging using X-ray Talbot interferometry can be significantly improved using gratings produced using carbon membrane-based X-ray masks.

Acknowledgment

This research was supported by the research project “Development of Systems and Technology for Advanced Measurement and Analysis” from the Japan Science and Technology Agency (JST).

References

- [1] D. Noda, M. Tanaka, K. Shimada, and T. Hattori, *Jpn. J. Appl. Phys.*, **46**, 2, pp. 849-851 (2007).
- [2] D. Noda, M. Tanaka, K. Shimada, W. Yashiro, A. Momose, and T. Hattori, *Microsyst. Technol.*, **14**, 9-11, pp. 1311-1315 (2008).
- [3] N. Takahashi, H. Tsujii, D. Noda, and T. Hattori, *Proc. 2008 IEEE Int. Symp. Micro-Nano Mech. Human Sci. Nagoya, Japan*, pp. 414-419 (2008).
- [4] A. Momose, *Jpn. J. Appl. Phys.*, **44**, 9A, pp. 6355-6367 (2005).

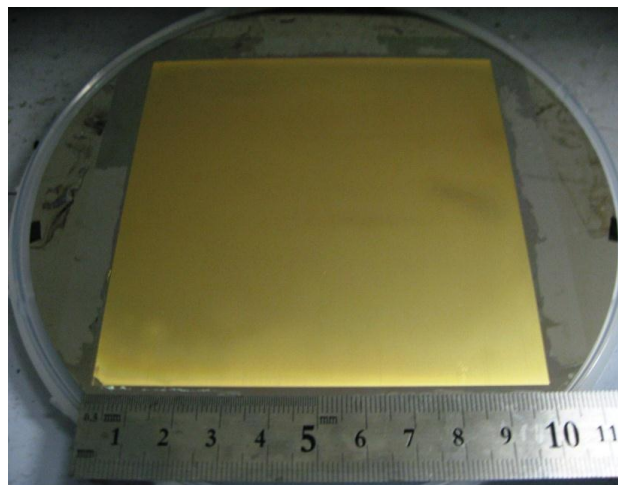


Fig. 2: Picture of carbon X-ray mask.

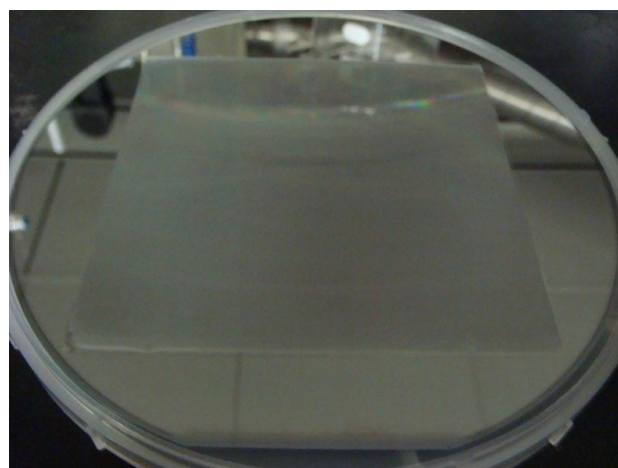


Fig.3: Picture of resist microstructure on 6 inch wafer.

Fabrication of High Aspect Ratio Au microstructures using Direct Electroforming on Si microstructures

Atsushi Tokuoka, Daiji Noda, and Tadashi Hattori
Laboratory of Advanced Science and Technology for Industry, University of Hyogo,

Abstract

Our research study combines the capabilities of Silicon deep reactive ion etching technology with UV lithography in order to fabricate high precision X-ray masks consisting of rectangular patterns, which cannot be achieved by UV lithography alone. Silicon deep reactive ion etching technology using inductively coupled plasma has attracted the attention of engineers working in this field, and this is a very effective technology for fabricating Si microstructures. We developed a fabrication method in which metallic microstructures are fabricated by electroforming directly into grooves etched in the Si after the sidewalls of the grooves have been coated with an insulating film. Au electroforming was accomplished from the bottoms of grooves etched into silicon. It is expected that this technology can be used in the production of a wide variety of devices.

Introduction

Nanotechnology is attracting attention as a technology that will play a key role in miniaturization and the increased sophistication of parts in the future. In particular, remarkable developments are being made in micro electro mechanical systems (MEMS) technology and this is contributing to downscaling and enhancing the performance of various components. Silicon deep reactive ion etching (DRIE) technology using an inductively coupled plasma (ICP) has attracted the attention of engineers working in this field [1], and this is a very effective technology for fabricating Si microstructures as shown in Fig. 1. Our research study combines the capabilities of Si dry etching technology with UV lithography in order to fabricate high precision X-ray masks consisting of rectangular patterns, which cannot be achieved by UV lithography alone. For the study, the X-ray mask to be fabricated was configured as a rectangular line-and-space mask comprising 5.3 μm pitch narrow lines [2-3].

We considered the method to fabricate Au microstructures in grooves fabricated in the Si substrate. In this method, the Au is electroplated directly onto the Si. However, in that alone the Au microstructures obtained are poor as shown in Fig. 2. This is due to the fact that electroplating takes place from among the bottoms, the top and the sidewalls of the grooves. It is necessary that electroplating take place from the bottoms of the groove only. If Au doesn't extract it only from the bottom of the structure, the cave can be done in the structure, and an excellent Au microstructure cannot be obtained as shown in Fig. 2.

New fabrication process

The new method for fabricating Au microstructures by directly electroplating on a structured Si substrate is shown in Fig. 3. The fabrication process consists of five steps: (1) applying resist to the Si substrate and forming a mask pattern in it using UV lithography, (2) etching grooves into the silicon by Si dry etching using an ICP etching system, (3) covering the Si microstructure and the remaining resist with a polymer film, (4) removing the polymer

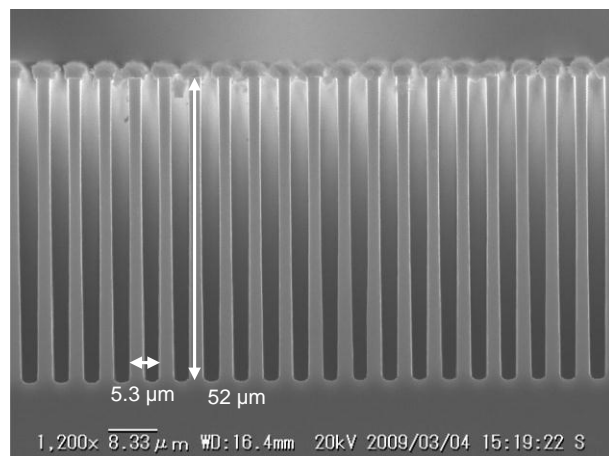


Fig. 1: SEM image of Si microstructures using ICP-RIE.

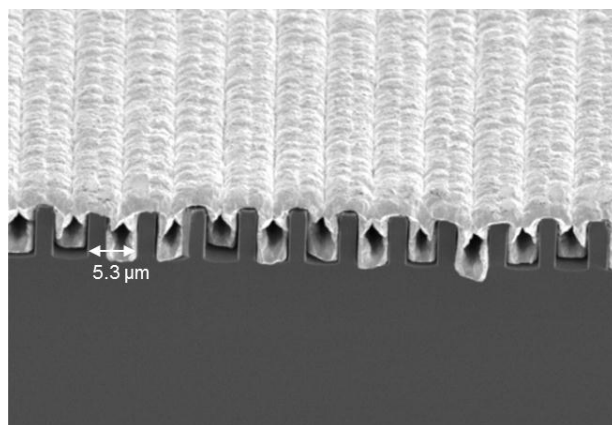


Fig. 2: SEM image of defective Au microstructures.

film from the bottoms only of the grooves by vertical anisotropic etching (5) depositing Au in the grooves by electroplating up from the bottoms of the grooves only. This new Au microstructure fabrication method uses the polymer coating process normally used in the Bosch process [4]. It is necessary that growth take place from the bottoms of the grooves only in order to form good quality Au microstructures. The polymer coating forms an insulating layer that prevents electroplating on the sidewalls.

Fabrication of high aspect ratio structures

The grooves were fabricated to a depth of 20 μm in first trial. After coating the sidewalls with polymer film the grooves were filled with Au to a depth of 18 μm by electroplating. A cross section of the completed microstructure is shown in Fig. 4. Thus, we successfully demonstrated the fabrication of high aspect ratio Au microstructures using the new fabrication method. Following this, we attempted to carry out the process on even higher aspect ratio grooves. However, it was difficult to form a sufficiently good quality polymer film on the sidewalls of the higher aspect ratio grooves using the process used on the lower aspect ratio grooves. We believe that changes to the experimental conditions are needed to enable us to fabricate Au microstructures in higher aspect ratio grooves.

Conclusions

Silicon dry etching technology makes it possible to fabricate precise high aspect structures. If these high aspect ratio grooves can be filled with Au then it becomes feasible to fabricate a structure that can be used as an X-ray mask. The Au structures were fabricated by electroplating directly on the Si. However, good quality Au microstructures cannot be obtained by electroplating in etched grooves since growth takes place from both the bottoms and the sidewalls of the grooves. In order to fabricate good quality microstructures, i.e. to completely fill the grooves with void-free Au, the sidewalls of the grooves need to be insulating, so that growth takes place from the bottoms only.

This can be achieved by coating the sidewalls with polymer. As a result, grooves 20 μm deep filled to a depth of 18 μm were successfully fabricated. However, it was difficult to form a sufficiently good quality polymer film on the sidewalls of the higher aspect ratio grooves.

From these results, we believe that changes to the electroplating conditions are needed to enable us to fabricate high-quality Au microstructures in these deeper grooves.

Acknowledgment

This research was supported by the research project “Development of Systems and Technology for Advanced Measurement and Analysis” from the Japan Science and Technology Agency (JST).

References

- [1] C. K. Chung, H. C. Lu, and T. H. Jaw, *Microsyst. Technol.*, **6**, 3, pp. 106-108 (200).
- [2] H. Tsujii, K. Shimada, M. Tanaka, D. Noda, and T. Hattori, *J Advanced Mech. Design, Systems, Manuf.*, **2**, 2, pp. 246-251 (2008).
- [3] D. Noda, H. Tsujii, N. Takahashi, and T. Hattori, *Microsyst. Technol.*, **16**, 8-9, pp. 1309-1313 (2010).
- [4] F. Lamer, A. Schilp, K. Funk, and M. Offenber, *Techn. Digest MEMS '99*, pp. 211-216 (1999).

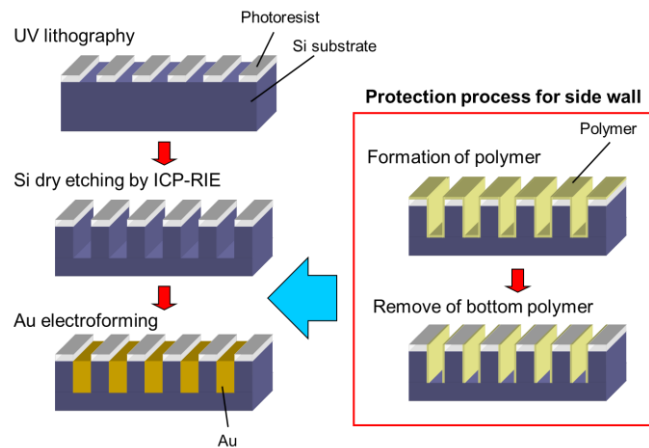


Fig. 3: Fabrication process of Au microstructures.

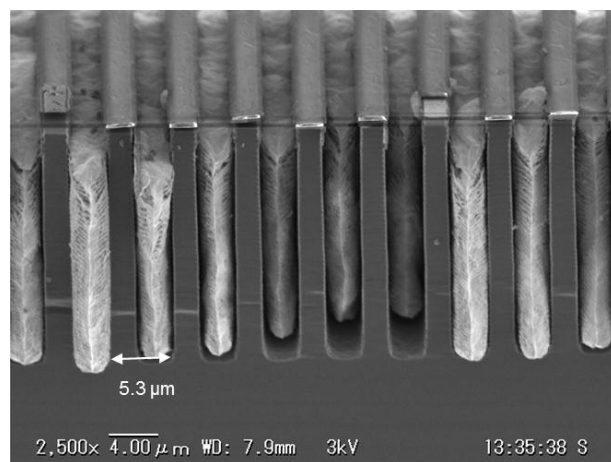


Fig. 4: SEM image of high aspect ratio microstructures.

SERS Active Three Dimensional Gold Nanostructure Fabrication for Optofluidic Device

R.Takahashi*

*Laboratory of Advanced Science and Technology for Industry, University of Hyogo, JAPAN

Introduction. Recently, surface enhanced Raman scattering (SERS) is attracting attention as a detection method suitable for micro region of microfluidic devices. In this study, we aimed at in situ, label-free and high sensitivity measurement by applying SERS to detection unit of microfluidic devices. In SERS measurement of fluidics, conventional colloid type is the mainstream. Such detection method using colloid, however, has resulted in problem of quantitativity because it is difficult to control colloidal particles in flow channel. To resolve this problem, we have developed and demonstrated the three dimensional gold nanostructure (Au3D).

Fabrication of Au3D. We prepared the well for construction of gold nanostructure by the way that the silicone sheet with a 6 mm through hole was stuck on the slide glass. Approximately 18 μl of gold nanoparticle (AuNP, 20 nm) and 1 μl of polystyrene latex beads (PS, 600 nm) dispersion liquid were mixed. 5 μl of the mixed solution was dropped into the well and dried under 75 % relative humidity. The self-assembled three dimensional PS structure was formed by casting method of convective self-assembly [1], where AuNPs were simultaneously accumulated in the gaps of the PS. Finally, in order to remove PS, the self-assembly structure was soaked in dichloromethane for 5 min. Thus, Au3D was obtained (Fig.1).

SERS measurement. At first, in situ SERS measurement was performed in the form of a batch using Au3D and 4,4'-Bipyridine (4bpy) as the Raman active molecule as following steps: Step 1, a measurement well was made of a clean silicone sheet with about 6 mm hole and Au3D on the slide glass. Step 2, 30 μl of 4bpy aqueous solution was dropped into the well, and covered with a cover glass so as to prevent drying of 4bpy solution and changing of 4bpy concentration. Step 3, 1 s irradiation of 785 nm (100 mW) laser focused on the Au3D was started. As shown in Fig.2, characteristic enhanced Raman spectrum of 4bpy (1000 cm^{-1} , 1200 cm^{-1} , 1280 cm^{-1} , 1600 cm^{-1}) was observed within 1 min after dropping 4bpy. The peak of 1 nM 4bpy solution was, however, weak although it was detectable without drying nor concentration.

Next, in situ and flow SERS measurement in microfluidic device with Au3D was performed as shown in Fig.3. The polydimethylsiloxane (PDMS) with microchannel was set on the slide glass where Au3D had been fabricated. The composed microfluidic device was fixed to the jig, and 50 μl of 4bpy aqueous solution was injected by a syringe. As results, we succeeded in highly sensitive detection of 1 nM with extremely improved S/N ratio as shown in Fig.4. This enhancement was estimated 10 times larger than that of batch measurement and reached over 10^7 compared with the normal Raman spectroscopy without Au3D. High sensitive improvement using microfluidic device like this didn't occur in the case of the two dimensional SERS substrate which was used in our laboratory [2]. The reason of this excellent result was as follows. In regard to two dimensional SERS substrate effective thickness of gold is less than 10 nm, while Au3D thickness is about 3 μm . Since adsorption surface area of the molecule becomes very large in being three dimensional, Au3D sterically produces many SERS activity spots. Furthermore, as explicit decrease in the peak intensity was not observed even by washing repeatedly as shown in Fig.5, Au3D has strongly absorbed 4bpy molecules. Thus, it was considered Au3D enabled trapping and accumulation of coming 4bpy molecules in a flow, and as a result, the excellent SERS was achieved. We demonstrated sufficiently that Au3D was effective for SERS measurement in microfluidic devices.

Conclusion. We have fabricated Au3D as SERS active substrate by casting method of convective self-assembly and demonstrated that Au3D is successful for optofluidic devices using SERS by comparing batch measurement and flow measurement.

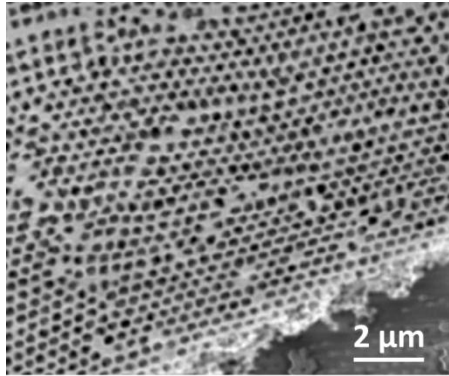


Fig.1: SEM image of Au3D. The diameter of the holes is about 600 nm.

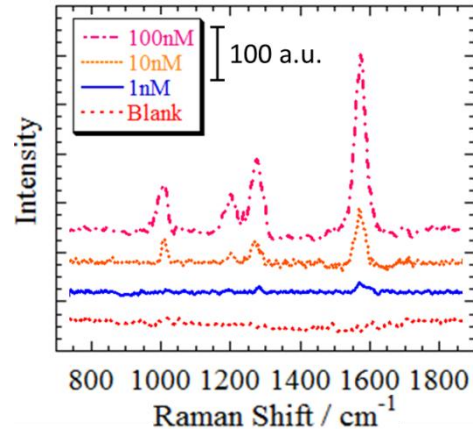


Fig.2: Characteristic enhanced Raman spectra of 4bpy with different concentration (100 nM, 10 nM, 1 nM, Blank) by batch measurement.

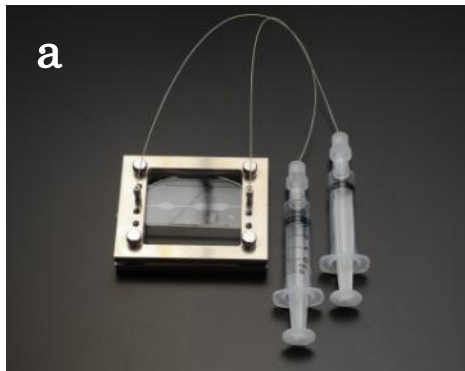


Fig.3: (a) Photo image of microfluidic device. (b) Cross section of microchannel in the microfluidic device (a). Au3D width is 6 mm, height is about 3 μm. Slide glass thickness is 1 mm. PDMS thickness is about 2 mm.

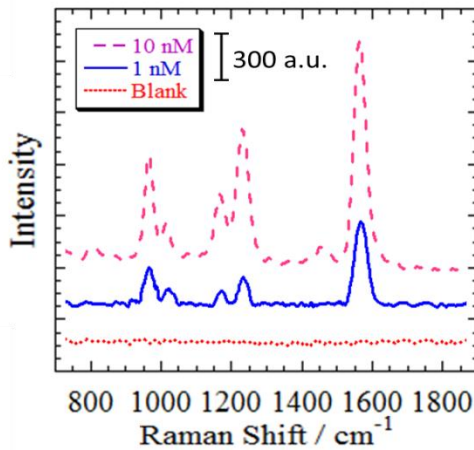


Fig.4: SERS spectra of 4bpy with different concentration (10 nM, 1 nM, Blank) by flow measurement.

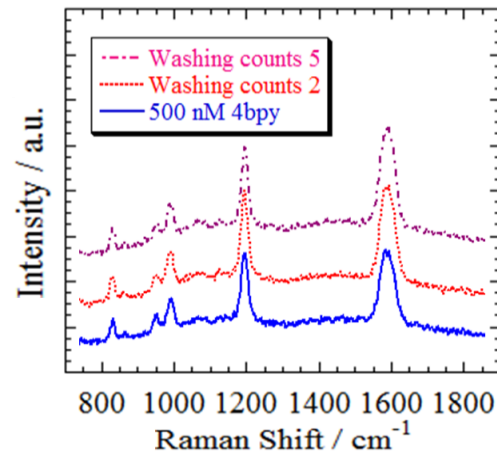


Fig.5: Evaluation of adsorption effect by washing Au3D. Au3D was repeatedly soaked in ultrapure water for 5 min after SERS measurement of 500 nM 4bpy.

Reference

- [1] Y. Mori, N. Shinohara, and T. Fukuoka, in International Workshop on Nanomechanical Cantilever Sensors 2008 (Mainz, Germany, 19 May 2008)
- [2] T. Fukuoka, M. Yoshida, R. Takahashi, M. Suzuki, Y. Utsumi, IEEE-NEMS W5D-3, (Kyoto, Japan, 7 March 2012).

Fabrication of Integrated Magneto Impedance Sensor for Medical Monitoring

Y. Yoritama¹⁾, T. Yamamoto¹⁾, T. Uchiyama²⁾, A. Yamaguchi³⁾, Y. Utsumi¹⁾
¹⁾University of Hyogo, ²⁾Nagoya University, ³⁾Keio University

Abstract

For medical monitoring, we fabricate integrated Magneto Impedance (MI) sensor. The sensor is magnetic sensor using skin effect. The fabricate process is complex consisting lithography process, sputtering process and electroplating process. Therefore, we optimize the process through repeated study of the chemical resistance of various materials and procedures, aimed at completion of the sensor.

Introduction

In recent years, the people's concern about their health is increasing under the influence of aging society in advanced nations. It is said that human health state is determined by the homeostasis of the body. Physical changes occur pulled by external factor will be offset by the action of the autonomic nerve system. This means that, the human health state depends on the autonomic nervous system. So if the system malfunctions, the state of the body can't be control. And the owner is ill. Therefore, we fabricate un-invasive healthy monitoring system consisted by near-infrared spectroscopic device for detection the amount of substance inside blood and integration magnetometric sensor to measure the dynamic characteristics of human's circulatory organ system as one of the function of the autonomic nervous system in same time. And the dynamic fluctuation of the circulatory system at the time of quiet and stress, and the characteristic of constant maintenance are investigated systematically. From the measurement results, do the mathematical modeling of the circulatory system response. And estimation and control of health status will be possible by this model applied to the signal obtained from the sensor.

The Principle of MI Sensor

Our present study aims at to fabricate ultra-high sensitivity magnetic sensor for medical monitoring system. This sensor is to be measured biomagnetic field, and its value size is about $10^{-10} \sim 10^{-13} \text{T}$. This value is very small than the magnetic field in the external environment such as geomagnetism, the minimum magnetic field like this could be measured by SQUID (Superconducting Quantum Interference Device) which is one of the most sensitive magnetic sensors. On the other hand, MI sensor using a magnetic impedance (MI) element has been attracting attention for improved the resolution of up to 10^{-12}T in late year [1]. The change in the high frequency impedance of very soft ferromagnetic materials upon the action of external dc fields, known as magneto-impedance (MI) effect, has been intensively studied for magnetic sensor applications [2]. The sensitive MI

effect occurs, when high-frequency current is applied to the zero magnetostrictive amorphous metal in which spin is arranged circumferentially. The impedance of a thin film, having length l and width w , is expressed as following formulas. The low frequency impedance corresponds to the DC resistance, while the high frequency impedance is proportional to the skin depth δ which is function of the dc magnetic fields. The sensing elements utilizing significant change in impedance due to the skin effect are easy handling devices. Our sensors detecting only the inductance component of impedance, is operating based on a pickup coil method (Fig.1).

$$\mu = \mu_0 + J/H$$

$$\delta = \sqrt{\frac{2\rho}{\omega\mu}}$$

$$Z \approx \frac{(1+j)\omega\mu\delta l}{4w} = \frac{\sqrt{\rho\omega\mu}}{4w}$$

Theoretical formulas.

μ_0 : Space permeability,

J : Magnetic polarization,

δ :Skin depth of skin effect,

ρ : Electric resistivity,

ω : Angular frequency of current,

l :Sheet length, w : Sheet width.

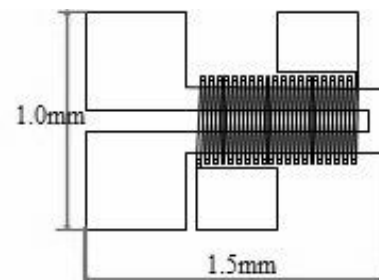


Fig.1 Outline of MI sensor. The number of turns on the coil was 20. The width of the Au wire is 20 μm .

Fabrication of Prototype Sensor

In this study, integrated MI sensor is fabricated using UV lithography and succeeding packaging method to improve productivity. In detail, we fabricated it by building up SU-8 layers shown in Fig.2. The sensor is in Fig.3. One side of sensor that was removed from the brass substrate is covered with Kapton film for insulation. Its size is 1.5mm in length, 1.0mm in width, and the thickness is 35 μ m (Without Kapton film). Its characteristics are

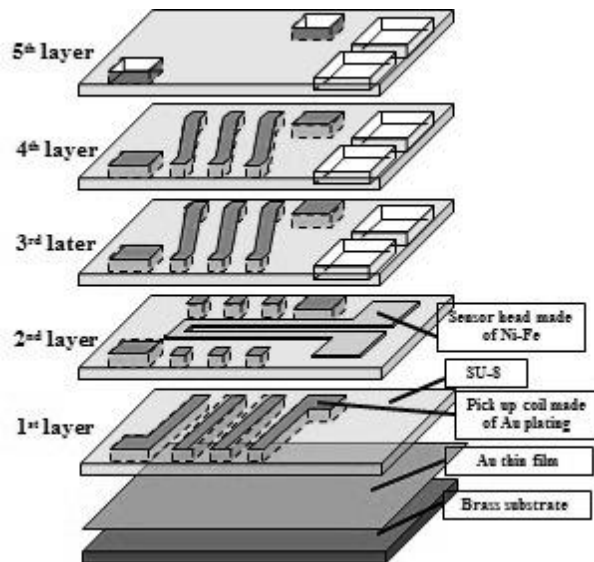


Fig.2 Outline our process.

SU-8 layer thickness of one is about 70 μ m.

Ni-Fe plate thickness is 60nm.

currently under investigation.

In this way, we have succeeded in fabricate a novel integrated MI sensor using UV lithography. This integrated sensor can be applied for health monitoring system using the results of this measurement. From the standpoint of maintaining health it can be applied in the prevention of lifestyle-related diseases. In addition, this device is also expected to apply to measure human stress or develop the some industrial technology.

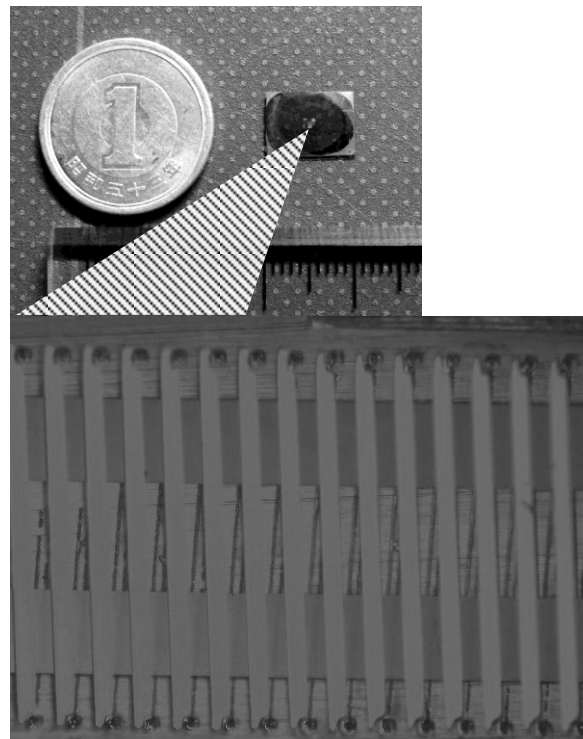


Fig.3 The completed sensor.

References

- [1] T. Uchiyama, A. Yamaguchi, Y. Utsumi, Noise Characterization of Coil Detection Type Magnetic Field Sensor Utilizing Pulse Excitation Amorphous Wire Magneto-Impedance Element, in J. Magn. Soc. Jpn., 34(Japan, 2010),533-536.
- [2] K. Mohri, Magnetic Sensors (Tokyo, Japan, 1998)

Blood separation chip for automated biological analysis

Hiroki Nose^a, Kazahisa kuroda^a, Masatoshi Kataoka^b and Yuichi Utsumi^a

^a Laboratory of Advanced Science and Technology for Industry, University of Hyogo,
Kamigori, Ako, Hyogo, 678-1205, Japan

^b Health Technology Research Center, AIST, Hayashi, Takamatsu, Kagawa 761-0395, Japan
e-mail: hiroki@lasti.u-hyogo.ac.jp

Abstract

We present a chip for the blood separation using centrifugal force and capillary force. We expect that this chip can perform overall assay with high-efficiency and significantly shorten the analysis time by integrate our proposed 3D lab-on-a-CD. The material of the chip which is fabricated by using X-ray lithography is SU-8 and Si. Blood separation is done using centrifugal force by spinning the chip at a frequency of 40Hz and transport to collection chamber from separation chamber using capillary force. It is necessary for capillary force to treat surface condition. We succeed in liquid transportation by only control spin speed.

Introduction

The lab-on-a-CD is promising for the automation of multiple microreactor systems. Recently, high-performance immunoassay based on lab-on-a-CD has been proposed [1]. The extraction of plasma from whole blood is the first preparative step in many assay protocols and major importance in medical diagnosis [2]. We present a chip for the extraction of blood plasma from whole blood using centrifugal force of spin and capillary force. We expect that this chip can be overall assay with high-efficiency and significantly shorten the analysis time by integrate our proposed 3D lab-on-a-CD [3].

Separation of the plasma from the blood cell is done using centrifugal force by spinning the chip at a frequency of 40Hz. Phase separation is caused in a centrifugal field by a difference in mass density. Only plasma is transported to collection chamber from whole blood separation chamber by capillary force. We designed chip show fig. 1. We expect that proposed chip would be able to extract only plasma from whole blood by only control spin speed.

Capillary force

$$F_{ca} = T \cos \theta \cdot 2\pi r$$

induced surface tension T and contact angle θ and bore diameter r .

Centrifugal force

$$F_{ce} = \rho \pi r^2 h R (2\pi v)^2$$

induced density of fluid mass ρ , frequency of spin v , the height of the rise of liquids h , and radial position to raised liquid center position from spinning center position R .

Centrifugal force exceeds capillary force, the plasma stays in the 1st chamber. When capillary force exceeds centrifugal force by acceleration of spin, the plasma is transported to the next chamber. The frequency which starts transportation of the plasma is shown below.

$$v = \sqrt{\frac{rT \cos \theta}{2\rho\pi^3 h R}}$$

Experiments and Results

This preparation chip made from a photoresist SU-8 (an epoxy-negative-tone resist) and Si wafer is fabricated by using X-ray lithography. X-ray photoresist SU-8 was applied to Si wafer and was exposed to x-ray and the exposed resist was developed by immersing into the SU-8 developer. Fig. 2 shows the preparation chip fabricated by using X-ray lithography. PDMS (polydimethylsiloxane) is used as the cover to seal microchannel.

According to affect capillary force, surface modification is important process. Contact angle of capillary are about 75° with normal condition. In order to increase capillary force, we control contact angle by the surface modification. The surface modification was done with UV ozone cleaner. We examined the optimum modification for capillary force. Optimum UV irradiation time which is ideal for liquid transportation is 7min.

We performed liquid transportation by using a water colored red (not blood) and we observed the behaviour of liquid transportation with a hydrophilic device. Fig. 3 which shows flow sequence in the chip was obtained by using strobe scope system. Thus, we succeeded in transporting the liquid to the 2nd chamber from the 1st chamber.

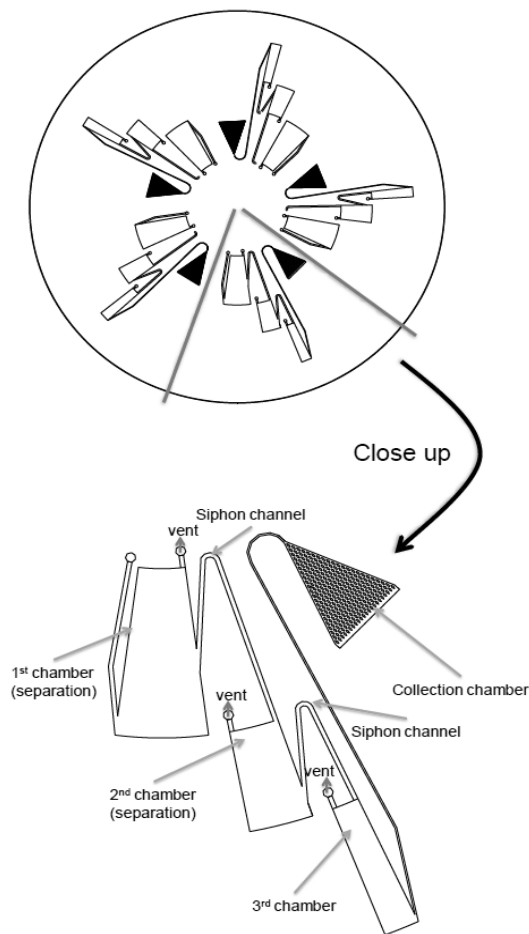


Figure 1 Schematic layout of blood separation

1. We inlet the whole blood to 1st chamber (separation chamber).
2. Separate plasma and blood cells by spinning chip at a frequency of 50Hz.
3. Separated blood plasma by sedimentation of whole blood transported to 2nd chamber (separation chamber) using capillary force.
4. Transported plasma in 2nd chamber again separated by spinning chip as well as 1st chamber and transport to 3rd chamber.
5. Transported plasma in 3rd chamber transported to collection chamber using capillary force.
6. Bottom of Collection chamber is pillar form for collection plasma using only capillary force.

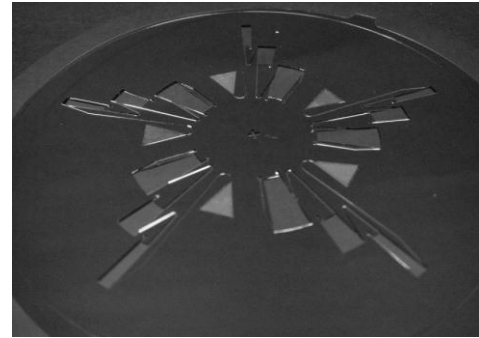


Figure 2 Photo of the fabricated chip The microchannels are fabricated by patterning photoresist SU-8 by x-ray lithography. The fabricated SU-8 chip is locally hydrophilized by exposure UV.

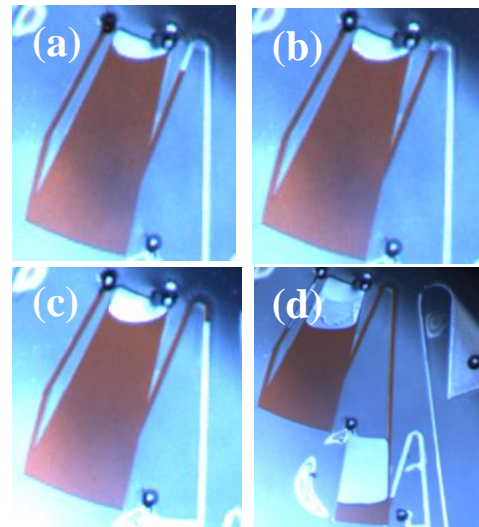


Figure 3 The figure shows the transportation from the 1st chamber to the 2nd chamber.

We observed the behaviour of liquid transportation with a hydrophilic device. (a) First we spun chip with high frequency. (b) Liquid transportation to 2nd chamber is begun at a frequency of about 25Hz. (c) The liquid passes the top of microchannel at a frequency of about 17Hz.(d)After the liquid passes the top, we rise rotation to the high frequency. The liquid transported to 2nd chamber rapidly. Thus, the transportation from the 1st chamber to the 2nd chamber succeeded.

References

1. Design of a Compact Disk-like Platform for Enzyme-Linked Immunosorbent Assay, S. Lai, S. Wang, J. Luo, L. J. Lee, S. T. Yang, and M. J. Madou, *Analytical Chemistry*, 76, 1832 (2004)
2. Centrifugal extraction of plasma from whole blood on rotation disk, Stefan Haebelre, Thilo Brenner, Roland Zengerle, and Jens Ducree, *lab chip*, 2006, 6, 776-781
3. Vertical liquid transportation through capillary bundle structure using centrifugal force, Saki Kondo, Tsukasa Azeta, Yoshiaki kita, Yuichi Utsumi, *Microsyst Technol*, 2010, 16, 1577-1580

Fabrication of fluorocarbon resin micro fluidic chip for processing of amino acid derivatization

Hideki Kido ^a, Hajime Mita ^b, and Yuichi Utsumi ^a

^a University of Hyogo, 3-1-2 Kouto, Kamigori, Ako, Hyogo, 678-1205, Japan

^b Fukuoka Institute of Technology, 3-30-1 Wajiro-Higashi, Higashi-Ku, Fukuoka, 811-0295, Japan

Abstract

Polytetrafluoroethylene (PTFE) is very attractive material for various fields. But, micro fabrication of PTFE is difficult from its high stability. However, synchrotron radiation (SR) induces the scission of polymer chain of PTFE. In this study, we succeeded the fabrication of PTFE micro fluidic chip by SR dry etching and thermal compression bonding. In the derivatization process, prevention of leaks is important to this device. Thus, we measured the liquid holding force by pressurizing of the channel while applying a load. In addition, we confirmed that breaking pressure changes with the capillary diameter of the PTFE filter.

Introduction

Polytetrafluoroethylene (PTFE) is very attractive material for various fields, because of its chemical resistance and heat resistance, etc. But, micro fabrication of PTFE is very difficult from its high stability. Therefore, PTFE has never been applied to micro fluidic device. However, it is known that synchrotron radiation (SR) induces scission of polymer chain of PTFE [1 2]. We have been fabricated PTFE microstructures such as micro filter by dry etching using SR [3]. As a next step, we have been considering application of PTFE micro fluidic chip for amino acid derivatization process. In this study, we succeeded in the fabrication of PTFE micro fluidic chip by SR dry etching and thermal compression bonding. PTFE is an ideal material for performing the derivatization process. Because, this process using some strong acid such as hydrochloric acid, and some processes such as extraction and hydrolysis require high temperature heating operation.

Experiments and Results

Figure 1 shows the schematic diagram of amino acid derivatization device. This device consists of two microchips, and the function of valve is performed by sliding of the chip. And it's also includes micro filters for filtration and hold the liquid during the heating operation. In this study, we demonstrate the fabrication of PTFE micro fluidic chip which include two simple micro channels. The PTFE chip is fabricated by the SR dry etching and the thermal compression bonding. In the SR dry etching, PTFE evaporates from the surface by irradiation of high energy X-ray and leads to the etching of micro patterns. In the assembly, we bonded PTFE substrates by the thermal compression bonding to form the PTFE micro fluidic chip. We have confirmed that the bond strength of this method is approximately 10 MPa (Fig. 2). Figure 3 shows the overview of assembly of PTFE chip. This chip is formed by laminating of three PTFE substrates. Size of PTFE chip is 1.2×20×60mm and dimensions of included channel is 600μm width and 400μm height. Figure 4 shows the fabricated PTFE micro fluidic chip, which has been filled in the channel with dye solution.

The derivatization device shown in Figure 1, upper chip has not bonded with lower chip. Therefore, prevention of leaks is very important to this device. Thus, we measured the liquid holding force by pressurizing of the channel while applying finite load. In this experiment, we used fabricated PTFE micro fluidic chip. Figure 5 shows the measurement result of the liquid holding force. In the derivatization process, approximately 30 kPa of liquid holding force is required for respond to pressure rise when the heating operation. From the measurement results, we have confirmed that sufficient holding force can be obtained by more than 15 MPa of applying load. In addition, we confirmed that breaking pressure changes with the capillary diameter of the PTFE filter as shown in Fig. 6. This micro filter consists from the bundle of capillaries. This measurement was performed using fabricated PTFE micro fluidic chip.

As mentioned above, we have proposed a micro fluidic chip for amino acid derivatization process. In this study, we succeeded in fabrication of PTFE micro fluidic chip. And we measured the fluid characteristic performance in the PTFE chip.

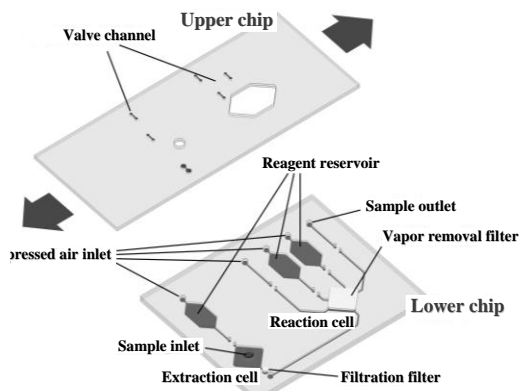


Figure 1. Schematic diagram of amino acid derivatization device.

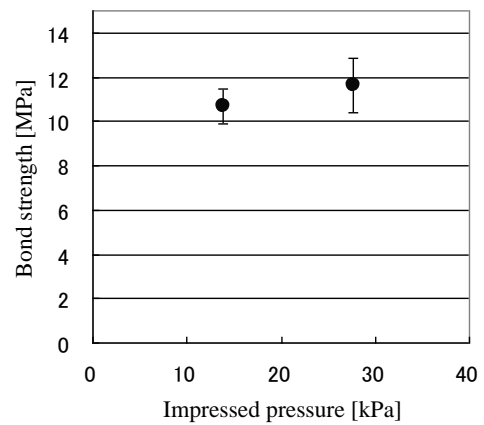


Figure 2. Measurement results of bond strength.

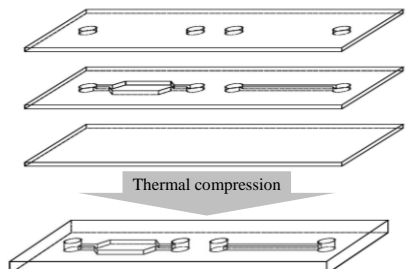


Figure 3. Overview of thermal compression bonding.



Figure 4. Fabricated PTFE micro fluidic chip.

Figure 5. Measurement results of holding pressure of slide valve.

Figure 6. Measurement results of breaking pressure of PTFE micro filter.

References

[1] Y.Zhang, T.Katoh, M.Washio, H.Yamada, S.Hamada, Appl.Phys.Lett.67 (1995) 872-874
 [2] Yuichi Utsumi, Takefumi Kishimoto, Tadashi Hattori Hirotsugu Hara, Jpn. J. Appl. Phys., 44,7B (2005) 5500-5504
 [3] Yoshiaki Ukita, Kazuhiro Kanda, Shinji Matsui, Mitsuyoshi Kishihara, Yuichi Utsumi, Microsyst Technol 14 (2008) 1567-1572

Contamination-Free Internally-Triggered Automatic Flow Sequencing for Microfluidics

M. Ishizawa^{a*}, H. Nose^a, Y. Ukita^b, and Y. Utsumi^a

^aLaboratory of Advanced Science and Technology for Industry, University of Hyogo, Japan

^bSchool of Materials Science, Japan Advanced Institute of Science and Technology, Japan

Abstract

Automation of micro-scale chemical system (MicroTAS) using centrifugal microfluidics has been intensively investigated [1-3]. Conventional valving methods using centrifugal microfluidics does not require complex external machines, however the device requires hand operations to do chemical process. We propose a simple liquid flow sequencing method which can carry out fully automated chemical process by just spinning the device at constant speed.

Introduction

Automation of micro-scale chemical system (MicroTAS) has been realized using a external control system consist of multiple components such as syringepump, pneumatic valve, reagent stock, many tubing, and computer controllers, therefore the whole system become huge and expensive and result in a problem so-called 'chip in a lab'. The centrifugal microfluidics realize liquid pumping with relatively simple control system. For the automation of multistep liquid handling on a centrifugal microfluidics, microvalves have been studied as follows. B. S. Lee et al have proposed the wax based microvalve [1]. The operation of the valve is realized by irradiating a laser from outside. S. Lay et al realized multi-step flow sequencing to use a passive valve that holds the liquid by surface tension, multi step flow sequencing is realized by accelerating the disk [2]. G. Welte realized multi-step flow sequencing by combining the principle of the siphon and the capillary action [3]. These studies report successful flow sequencing, however none of them realize low-cost, reliable, and simple automation due to the requirement of *external-triggered* control. This paper reports a fluidic circuit design which realize on-chip controlling of multi-step flow sequencing on a steadily spinning CD.

Experiments and Results

Figure 1 shows the principle of valving method, which applied in our method. Considering microfluidic channel on a disk as shown in fig. 1(a), the liquid reservoirs, which are arranged in a radial direction on a disk and be connected with vent. When one of vent is closed as shown in fig. 1(b, c) the loaded liquid in a reservoir cannot flow in the waste even the disk is spun at high speed. On the other hand, when both of the vents are opened the liquid can flow and be injected in the waste reservoir, when the disk is spun as shown in fig. 1(d). In other words, by controlling the air supply to the reservoirs, can be controlled liquid flowing.

Figure 2 shows schematic illustration of designed flow sequencer. The device has two liquid stock reservoirs. Both of them are connected to waste reservoir having air out vent, however only 1st reservoir is connected to air in vent. On the other hand, vent channel of 2nd reservoir is connected to the outlet of the 1st reservoir via dummy reservoir. When the device is spun, the liquids will move toward to the edge of the disk due to centrifugal force, however the liquid from 1st reservoir will flows in the venting channel of 2nd reservoir and block the vent channel of 2nd reservoir. Because this state is same as fig. 1(b), therefore the liquid in the 2nd reservoir cannot move and retained until the 1st reservoir become empty as shown in fig. 2(b). We observed that the dropped pressure in 2nd reservoir aspirates liquid plug, therefore the dummy reservoir is located in middle of the venting channel, to prevent the contamination in 2nd reservoir. The vent channel will be opened when the 1st reservoir become empty, then the liquid in 2nd reservoir starts to flow as shown in fig. 2 (c). Then finally the liquid sequencing will be completed. In this concept, the first liquid behaves like '*clepsydra*' to control the timing of injection of other reservoir(s).

To demonstrate the concept, we fabricated a device based on the design shown in fig. 2. The microchannel structure is patterned on poly-dimethylsiloxane (PDMS) by conventional soft lithography process. This PDMS is attached on the spin coater. For the visualization of the flow sequencing the colorized waters (red and blue) are loaded in the reservoirs and reservoirs are sealed with flat PDMS having vent hole made with syringe needle. The device is placed in custom-made machine and spun at constant frequency of 2000 rpm for 10 sec. Flow image is recorded by strobe scope system. Figure 3 shows the images of flow sequencing. As shown in the fig. 3, automatic flow sequencing at constant and high rate spinning is successfully demonstrated. The method is expected to be effective realizing simple automated *internally-triggered* liquid handling for multi-step chemical process.

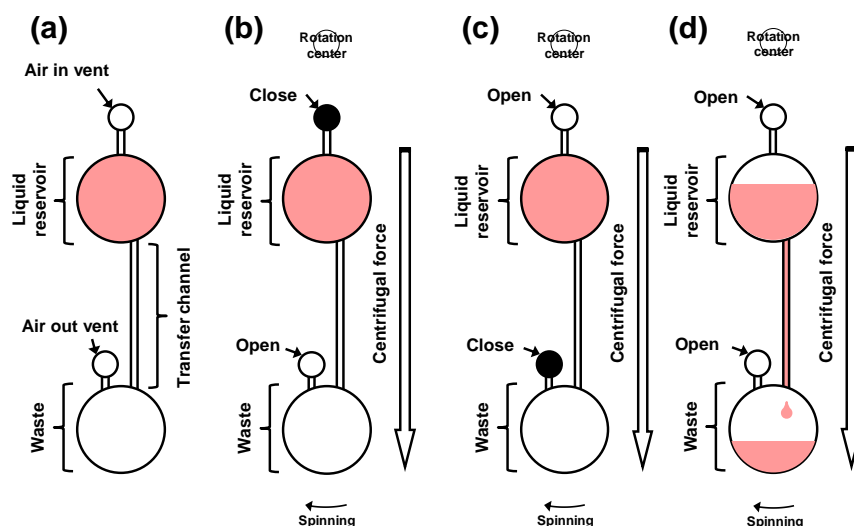


Figure 1: Principle of valving. (a) Initial state of the liquid (liquid is loaded in the liquid reservoir) (b) liquid injection with closed air in vent (liquid does not flow due to lack of air supply from air in vent) (c) with closed air out vent (liquid does not flow due to blocking of air exit) (d) with opened vents (liquid flows and get transported to waste reservoir)

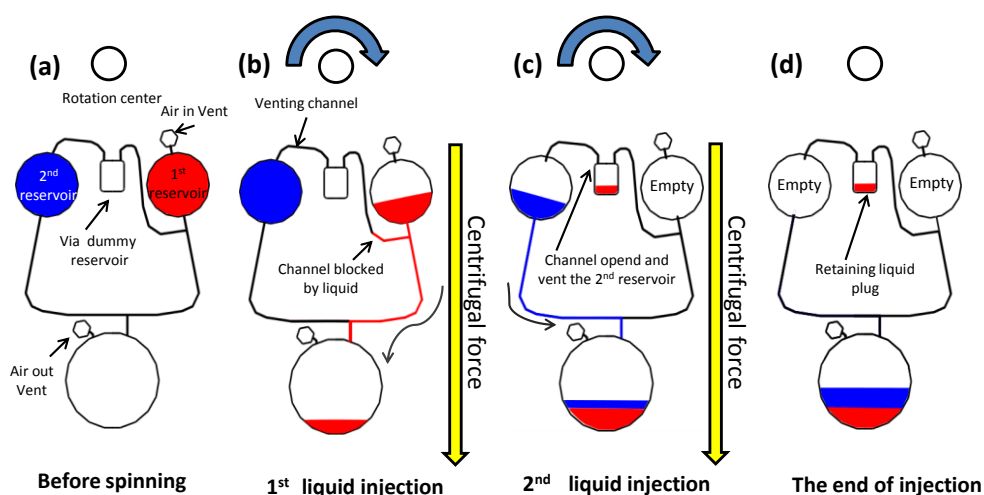


Figure 2: Sequencing method (a) initial state of flow sequencing (b) 1st liquid injection (vent channel of the 2nd reservoir is blocked by 1st liquid) (c) 2nd liquid injection (following 1st liquid injection) (d) sequencing completed (both reservoirs are empty)

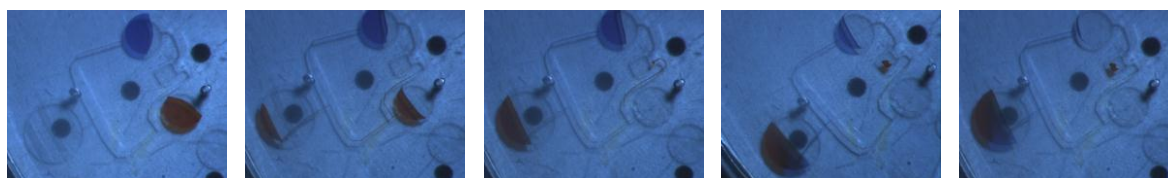


Figure 3: (a) Initial state of spinning (both reservoirs are filled with water) (b) 1st liquid injection (air vent channel of 2nd reservoir is blocked by 1st liquid) (c) 1st liquid injection completed and 2nd liquid injection starts (e) during 2nd liquid injection (e) 2nd liquid injection completed

References

- [1] B. S. Lee *et al.*, *Lab Chip*, 2009, 9, pp. 1548-1555
- [2] S. Lai *et al.*, *Anal. Chem.*, 2004, 76, pp. 1832-1837
- [3] G. Welte *et al.*, *Proc. of Micro TAS 2010*, pp. 818-820

Reflected Surface Acoustic Wave Actuator Using Micro Groove

Tsunemasa Saiki^{a,b}, Hikaru Tomita^b, Yasuto Arisue^b, Hiroo Shizuka^b, Koichi Okuda^b, Kazusuke Maenaka^b, Yuichi Utsumi^b

^a Hyogo Prefectural Institute of Technology, Kobe, 654-0037, Japan

^b University of Hyogo, Himeji, 671-2280, Japan

e-mail: saiki@hyogo-kg.go.jp

Abstract

Surface acoustic wave (SAW) devices with very simple structures have attracted attention. Therefore, we studied SAW actuators that could enable a. high efficiency microfluidic mixing chip [3]. On the other hand, we considered that powder transport is also possible by using the SAWs. However, in powder transport that is different from continuous liquid flow in channels, it is difficult to move object in directions other than one of the SAW propagation. Then, a novel SAW actuator based on these results was designed and fabricated, and its possibility of powder transport by the SAW reflected from the micro-groove was evaluated.

Introduction

The manufacturing process for each component device in a lab-on-a-chip must be simplified for multiple functional devices to be integrated. Surface acoustic wave (SAW) devices with very simple structures have attracted attention. Therefore, we have studied a high efficiency microfluidic chip that consists of SAW pumps, a SAW mixer, a Y-type flow channel, and so on [1-3]. Moreover, we considered that using SAWs can not only flow liquid but also transport powder, because solid moving by the SAWs had been reported [4]. If powder can be transported, we can establish a dissolution process consisting of powder movement, powder injection into liquid, and themselves mixing operated only by the SAWs on one-chip. However, unlike continuously flowing liquid in a channel, spatially controlling powder transport by using the SAWs is difficult, because the powder transport direction must be aligned with an axis direction of an interdigital transducer (IDT) that generates the SAWs. We thus proposed and fabricated a novel SAW actuator using a reflection wave from a micro groove and evaluated its ability to move powder.

Experiments and Results

Figure 1 shows our experimental setup for observing the powder movement caused by a reflected SAW actuator. In the experiment, a function generator created 1-kHz burst waveforms consisting of 1000 cycles of 19.2-MHz sine waves, and an amplifier boosted the burst waveform voltage. When the burst waveform voltage was applied to an IDT electrode (a 200- μm stripline pitch, a 5-mm aperture, and 20 stripline pairs) patterned on a piezoelectric wafer (127.8-degree y-rotated x-propagating LiNbO_3), SAWs were generated. The SAWs propagated in the perpendicular direction against orientation flat of the wafer. The SAWs were then reflected by a micro groove (a 30-degree inclination angle, a 100- μm depth, a 100- μm width, a 5-mm length) located 20-mm from the IDT and fabricated by cutting work. We chose this inclination angle because the SAWs reflected by the micro groove can propagate efficiently. Note that Figure 2 shows our other experimental results for the relationship between SAW propagation angle against orientation flat and SAW transfer characteristic (SAW amplitude / electric power applied to IDT). Here, the SAW amplitudes were measured by a laser Doppler vibrometer. The SAWs of a 60-degree propagation angle, i.e. the reflected SAWs of a 30-degree inclination angle, had good transfer characteristics. On the other hand, we chose this micro groove depth because we considered that the SAW reflection ratio increases as the micro groove deepens in theory. The reflected SAWs arrived at copper powder, which has an 8.9 specific gravity and an average particle about 10- μm in diameter. The powder was then energized by the reflected SAWs and moved to the upper stream of the SAWs, i.e. the micro groove, as shown in the photographs taken using a high-definition camera in Figure 3. Here, the electric power applied to the IDT was about 1.7-W. This fact reveals that the reflected SAW actuator can transport the powder. Moreover, to investigate the powder moved by transmitted SAWs, we also carried out another powder movement experiment for different a micro groove shape (a 15-deg. inclination angle, a 10- μm depth). Figure 4 shows photographs of powder moved by transmitted SAW. These results reveal that not only reflected but also transmitted SAWs can transport the powder.

The above mentioned facts prove that the powder transport using the reflected and transmitted SAWs can be controlled by adjusting the inclination angle and depth of the micro groove. In our future work, we will develop high-performance reflected and transmitted SAW actuators by using multiple micro grooves in order to fabricate lab-on-a-chips for synthesis and analysis including the dissolution process.

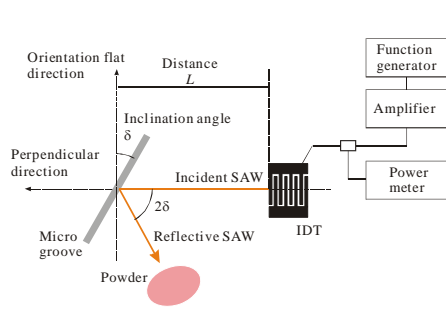


Figure 1. Experimental setup for observing powder moved by reflected SAW actuator.

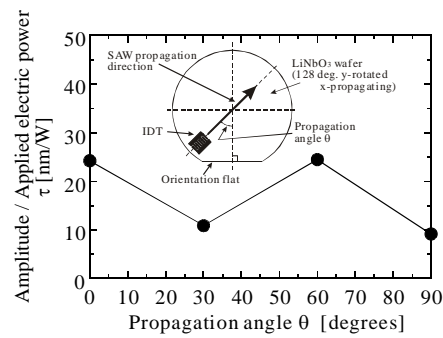


Figure 2. Relationship between SAW propagation angle against orientation flat and SAW amplitude / electric power applied to IDT. Here, \square is $2\square$.

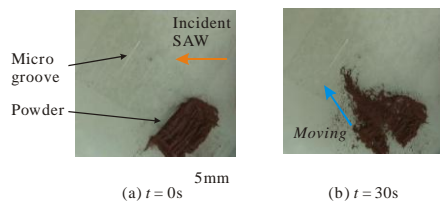


Figure 3. Photographs of powder moved by reflected SAW.

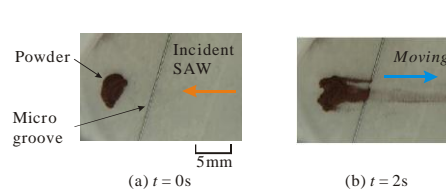


Figure 4. Photographs of powder moved by transmitted SAW.

References

- [1] Y. Utsumi, T. Saiki and K. Okada, "Proposal of a Novel Continuous Flow Pumping Operated by Surface Acoustic Wave," 12th International Conference on Miniaturized Systems for Chemistry and Life Sciences (μ TAS2008), 715 (2008).
- [2] T. Saiki, K. Okada and Y. Utsumi, "Micro Liquid Rotor Operated by Surface-acoustic-wave", Micro System Technology, Vol.16, pp.1589-1594 (2010).
- [3] T. Saiki, K. Okada and Y. Utsumi, "High Efficiency Mixing and Pumping of Continuous Liquid Flow using Surface-Acoustic-Wave", 13th International Conference on Miniaturized Systems for Chemistry and Life Sciences (μ TAS2009), 58 (2009).
- [4] M. Kurosawa, M. Takahashi and T. Higuchi, "Ultrasonic Linear Motor Using Surface Acoustic Waves", IEEE Transactions on Ultrasonics, Ferroelectrics, and Frequency Control, 43, 901 (1996).

Damage Analysis of n-GaN Etched with He and N₂ Plasmas

Masahito Niibe¹, Takuya Kotaka¹, Retsuo Kawakami², Yoshitaka Nakano³, and Takashi Mukai⁴
¹Univ. Hyogo, ²Univ. Tokushima, ³Chubu Univ., ⁴Nichia Co.

Abstract

To understand the details of etching-induced damage on a GaN surface, n-GaN crystals were plasma-etched with He and N₂ gases. The etched surfaces were analyzed by XPS and soft X-ray absorption spectroscopy (XAS) methods. The shape of the near-edge absorption fine structure (NEXAFS) of the N-K edge deformed with increasing gas pressure and processing time. The deformation can be explained by the increase of the band widths of a number of peaks constructing the NEXAFS spectra due to the increase of structural disorder in the crystal. The increase in band widths for the surface etched with N₂ plasma was larger than that for the surface etched with He plasma.

Introduction

GaN-based semiconductors are widely applied to photoemission devices or high-frequency power electronics devices because of their excellent characteristic features. To further improve the performance of these devices, it is highly desirable to develop plasma-etching processes that are damage-free. However, control of plasma-etching damage is currently insufficient because of the complicated relationships between the non-equilibrium plasma behavior and reactions on the semiconductor surfaces in plasma processes.

To understand the mechanism of defect creation by physical etching, we have etched n-GaN crystals using a capacitively coupled radio frequency (RF) plasma reactor with rare gases of Ar, Kr, or Xe and evaluated various characteristics, such as the surface morphology, surface composition, and electronic properties [1]. Helium (He) is a rare gas with very light mass; it is expected to have a much larger preferential etching ratio than other rare gases for the two constructing atoms, Ga and N, in a GaN binary alloy. On the other hand, N₂ has the capability to compensate for the composition deviation induced by preferential etching because it contains the component element of GaN crystal. In this paper, n-GaN crystals were plasma-etched with He and N₂ gases, and their surfaces were analyzed from the viewpoint of structural disordering. The result of nitrogen-K near edge X-ray absorption fine structure (NEXAFS) spectroscopy [2] is reported.

Experiments

Plasma etching of n-GaN crystals was carried out using a capacitively coupled RF plasma reactor with an unbalanced electrode structure at the constant self-bias voltage of -200 V. He and N₂ gases were used as the plasma source gas. GaN samples were Si-doped GaN crystals grown on a sapphire substrate with 4 μm thickness by the metal-organic chemical vapor deposition (MOCVD) method (n-GaN, Nichia Co.). The etching gas pressure was changed in the range of 10 – 100 mTorr with the processing time changing up to 200 min. The etching rates for He and N₂ plasmas were 0.77 and 0.36 nm/min at gas pressure of 10 mTorr and 0.59 and 0.17 nm/min at 50 mTorr, respectively.

The composition change in the plasma-etched GaN surface was evaluated by the X-ray photoelectron spectroscopy (XPS) method (Shimadzu, ESCA-1000). The N/Ga ratio on the surface was determined by the integrated intensities of N1s and Ga3s peaks. The relative composition deviation was calculated with an N/Ga ratio of the as-grown sample equaling one.

NEXAFS spectroscopy at nitrogen K-edge soft X-ray absorption (~400 eV) was conducted for analyzing the etching damage. The NEXAFS measurement was carried out at the analyzing station of beamline 9 at the NewSUBARU synchrotron radiation facility. The measurement was carried out using the total electron yield (TEY) method in a sample current mode and the total fluorescence yield (TFY) method [3], which included measuring the amount of fluorescence with an Al-coated photodiode to avoid yellow-band (secondary) emission. TEY and TFY measurements were carried out simultaneously for the same sample at the same position. It is well known that the TEY method can yield information in a shallow region from the sample surface because of the small escape length of photo-generated electrons of less than about 5 nm [2]. Meanwhile, the TFY method can yield information of a deeper region (bulk) of a sample of more than 100 nm [3] because of the much longer penetration depth of soft X-ray photons.

Results

Figure 1 shows the typical NEXAFS spectra at the N-K edge of n-GaN crystals etched with N₂ plasma. Figure 1(a) shows the gas pressure dependence of the spectral changes in NEXAFS at the processing time of 100 min obtained by the TEY method. The spectrum of the as-grown sample agrees well with that previously reported for

wurtzite-type crystal [4]. According to Katsikini et al. [4], the complicated absorption shape at a photon energy of 400 – 414 eV can be explained by the superposition of six Gaussian peaks, i.e., G1- G6 as indicated in Fig. 1(a).

As shown in Fig. 1(a), the complicated peak shape became smoother or blunter with increasing N₂ gas pressure from 10 to 100 mTorr. The same tendency was observed with increasing processing time from 5 to 200 min. This is because of the increases in defect density as well as the amorphous-like structures at the crystal surface with increasing gas pressure or processing time.

Deenapanaray et al. reported [5] that new pre-edge and post-edge absorption peaks called RL1 and RL2 were observed in the NEXAFS spectra by high-energy Ar ion bombardment of 0.4 – 2.5 keV on a GaN surface. After the analysis by Katsikini et al. [6], these new peaks were assigned to the absorption of N atoms at the interstitial site for RL1 and to that of the nitrogen molecules in the crystal for RL2, respectively. However, in this study, the appearance of a remarkable peak corresponding to RL1 or RL2 was not observed even in the most damaged sample etched at 100 mTorr and 200 min.

The NEXAFS spectra of the nitrogen K-edge of n-GaN crystals etched with N₂ plasma measured by the TFY (fluorescence) method are shown in Fig. 1(b). As a distinctive result different from the TEY measurement shown in Fig. 1(a), almost no change in the NEXAFS spectra depending on the processing time was observed for the spectra obtained by the TFY method even though the measurements were carried out for the same samples. This result is related to the fact that the TFY measurement is a bulk-sensitive method. Namely, the etching damage detected by the TEY method in this study could be restricted only in shallow regions of less than about 5 nm from the surface [3]. Furthermore, in regions deeper than 5 nm, a rigid crystalline structure could be maintained containing light defects in the etched n-GaN crystal. The result of particle model (PIS) calculation indicates that the thickness of heavily damaged layer (N/Ga ratio is not equal to one) is about 5 – 6 nm. The above result agrees well with the PIS calculation.

Figure 2 shows the NEXAFS spectra of the nitrogen K-edge of n-GaN samples etched with He plasma obtained by the TEY method. Figure 2 represents normalized data at the G2 (the highest) peaks. The N-K absorption intensity decreased with increasing gas pressure. The result indicates that the surface density of

nitrogen atoms decreases because of the preferential etching of nitrogen atoms on the GaN crystal. On the other hand, the degree of peak shape smoothing in He-etched samples was much smaller than that in the N₂-etched one, although blunting of the peak shape was certainly observed. These results can be mainly attributed to the difference of the elastic energy transfer ratios by the collision of the He⁺ and N₂⁺ ions in plasma to the GaN solid surface.

References

- [1] M. Niibe et al.: *Phys. Status Solidi*, **C8** (2011) 435.
- [2] J. Stohr, '*NEXAFS Spectroscopy*' Springer, Berlin (2003).
- [3] T. Kotaka and M. Niibe: *Adv. X-ray Chem. Analysis*, **43** (2012) 175.
- [4] M. Katsikini et al.: *J. Appl. Phys.*, **83** (1998) 1437.
- [5] P. N. K. Deenapanaray et al.: *Appl. Phys. Lett.*, **83**, (2003) 4948.
- [6] M. Katsikini et al.: *J. Phys. Conf. Series*, **190** (2009) 012065.

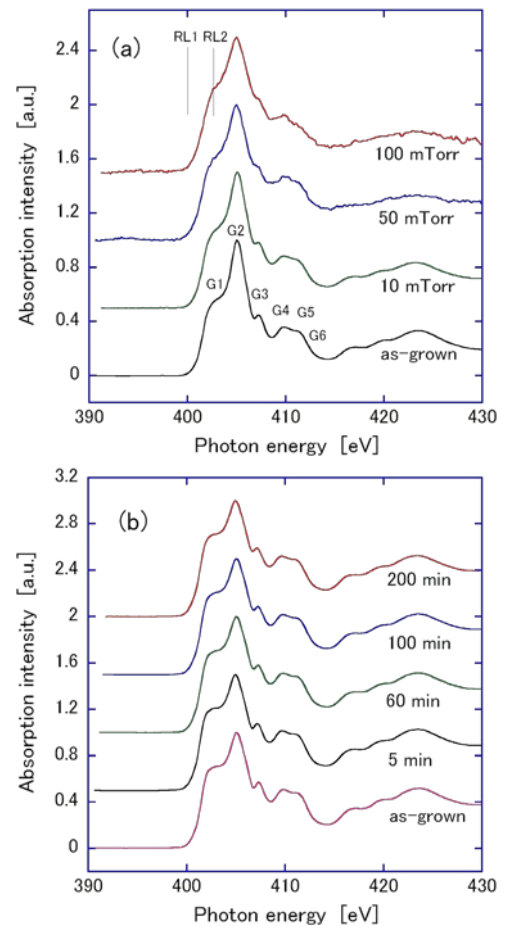


Fig.1 NEXAFS spectra of nitrogen K-edge of n-GaN crystals etched with N₂ plasma obtained by (a):TEY and (b):TFY method at the angle of incidence of 90° from the surface.

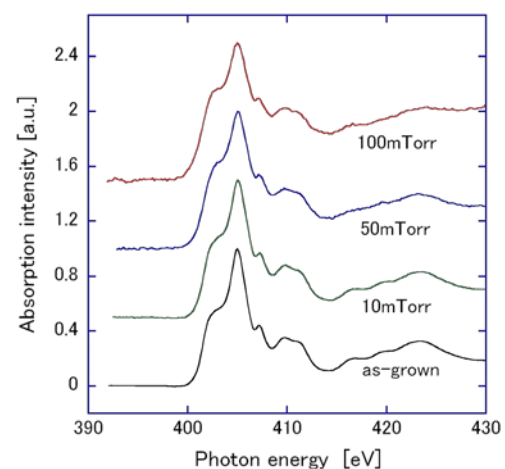


Fig.2 NEXAFS spectra of nitrogen K-edge of n-GaN crystals etched with He plasma obtained by the TEY method.

Investigation of analyzing depth of N-K absorption spectra measured using TEY and TFY methods

Takuya Kotaka, Masahito Niibe, and Tohru Mitamura
LASTI, University of Hyogo

Abstract

In order to investigate the analyzing depth of N-K absorption spectra measured using the TEY and TFY methods, the spectra of Si_3N_4 crystals covered with Cr thin films were measured. The thicknesses of Cr films were 1 – 100 nm. The N-K absorption intensity of Si_3N_4 measured using the TEY method was observed at Cr thickness of less than 3 nm, while that measured with the TFY method was observed for more than 100 nm. The decrease in the TFY peak intensity was explained by the transmittance of Cr film.

Introduction

In near edge X-ray absorption fine structure (NEXAFS) spectroscopy at soft X-ray region, the total electron yield (TEY) method with the sample current mode is widely used because it can be obtained using relatively simple equipment. The partial electron yield (PEY) method is also often used to examine photoelectron yields with a simple energy discrimination detector. However, because the escape depth of an electron in solids is about a few to a few tens angstrom [1], information obtained by TEY or PEY is restricted in a sample surface. To obtain information from sample bulk, the total fluorescence yield (TFY) method is employed with detection of fluorescent X-rays that can penetrate from deeper region of the sample.

Although, the energy dependence of the typical mean free path of an electron [2] or the X-ray penetration depth [3] in solids has been already reported, such data are rather distributed, and, therefore, precise information of analyzing depth for individual energy and material is insufficient. In this paper, we propose a convenient method to investigate the analyzing depth of the TEY and TFY methods for individual photon energy. Absorption intensity at the N-K edge (~ 400 eV) of Si_3N_4 crystals covered with Cr thin film was obtained by the TEY and TFY methods. A photodiode was used as a fluorescence X-ray detector for the TFY measurement; this detector had wide energy range of sensitivity, including visible lights, but was very simple to use. The analyzing depth at the N-K edge for both methods was evaluated.

Experiments

The sample used to investigate the analyzing depth was Si_3N_4 crystal grown on a Si wafer with thickness of 200 nm (NTT-AT Co.). A part of the Si_3N_4 sample was covered with Cr thin films of thickness ranging from 1 to 100 nm, which was deposited by magnetron sputtering. Cr was not coated on the entire surface because, to compensate for an absorption intensity difference arising from the surface state difference of the individual samples (about 5%), the N-K absorption intensity was normalized with the intensity of the non-coated area. Cr is a suitable material for uniformly covering the Si_3N_4 surface because Cr film is less likely to island-grow [4]. The thicknesses of Cr films were controlled with the deposition time because the deposition rate of the sputtering system was very stable.

NEXAFS spectroscopy at the N-K edge was carried out at the end station of the beamline BL9A in the NewSUBARU SR facility at the University of Hyogo [5]. The measurements were carried out using the TEY and TFY methods. The TEY measurement was conducted with monochromated soft X-rays incident on the Cr thin film, and the amount of secondary electrons emitted from the Si_3N_4 layer underneath was detected by means of the sample current mode.

The TFY measurement was conducted by detecting the fluorescence emitted from the Si_3N_4 layer underneath the Cr thin film. The X-ray detector used for TFY method was a photodiode (AXUV-100, IRD), which was placed at the angle of 30° from the sample normal and a distance of 3 cm. To prevent the inflow of secondary electrons from a sample into the electrodes, the surrounding of electrode leads were covered with Al plate, as



Fig. 1 Photodiode detector. The electrode leads were covered with an Al plate.

shown in Fig.1. Because electrons flow into the acceptance surface of the photodiode run down to the earth through a cathode lead, they are not detected by a pico-ammeter inserted in the anode lead. The photodiode, whose acceptance surface was coated with Al thin film of 40 nm thickness, was used to prevent the influence of secondary emission of visible light.

Results and discussion

Figure 2 shows the N-K absorption spectra of Si_3N_4 crystal covered with Cr thin film of various thicknesses measured using the (a): TEY and (b): TFY methods. In Fig. 2(a), the spectra of the samples covered with Cr thicknesses of 0 – 4 nm are shown. There is no change in spectra for the sample with Cr thickness greater than 4 nm. The peak intensity near 405 eV originated from Si_3N_4 crystal decreased with increasing Cr thickness and was observed to a Cr thickness of 2 nm. A slight peak was detected for the Cr thickness of 3 nm, and none was detected at 4 nm. Another peak near 400 eV was observed for the samples with Cr thickness greater than 3 nm. Because the peak was observed only at the Cr-deposited part, the 400 eV peak must arise from a native chromium nitride film. From the result above, the N-K absorption spectra obtained by the TEY method reflected the information at a shallow region of less than about 3 nm from the surface. An electron mean free path in solids at 400 eV is about 1 nm as previously reported [1,2]. Therefore, the analysing depth obtained by the TEY method in this study can be almost explained with the electron mean free path.

As shown in Fig. 2(b), the peak intensity near 405 eV measured with the TFY method decreased with increasing Cr thickness. However, it was detected even from the sample with Cr thickness of 100 nm with an intensity of about 30% of that detected at the non-coated Si_3N_4 surface. From the result above, the N-K absorption spectra obtained by the TFY method was found to reflect the information from the sample bulk, and the amount of contribution from a region of a few nm depth from the surface was relatively small.

Figure 3 shows the thickness dependence of the peak intensity near 405 eV calculated with the transmission coefficient of Cr film

[3] and the peak intensity measured using the TFY method. According to a previous report [6], the N-K fluorescent photon energy of Si_3N_4 is mainly about 393 eV. Therefore, the transmission coefficient was calculated with incident photon energy of 405 eV and with output photon energy of 393 eV. The angle of output light (30°) was also considered to calculate the light path length. The experimental intensity agrees well with the calculated value for various Cr thickness samples. Therefore, the peak intensity obtained by the TFY method can be explained almost fully by the absorption of the upper Cr layer.

Acknowledgements

The authors express their thanks Dr. H. Takenaka at NTT-AT Co. for providing a SiN wafer for sample material.

References

- [1] J. Stohr: "NEXAFS Spectroscopy" Springer Berlin, (2003) p.123.
- [2] I. Lindau and W.E. Spicer: J. Electron Spectrosc. **3**, 409 (1974). C.J. Powell: Surf. Sci. **44**, 29 (1974).
- [3] <http://www.cxro.lbl.gov/>.
- [4] M. Niibe et al.: Rev. Laser Engineer. **24**, 48 (1996).
- [5] M. Niibe et al.: AIP Conf. Proc. No. **705** (AIP, New York, 2004) p.576.
- [6] G. Wiech and A. Simunek: Phys. Rev. B **49**, 5398 (1994).

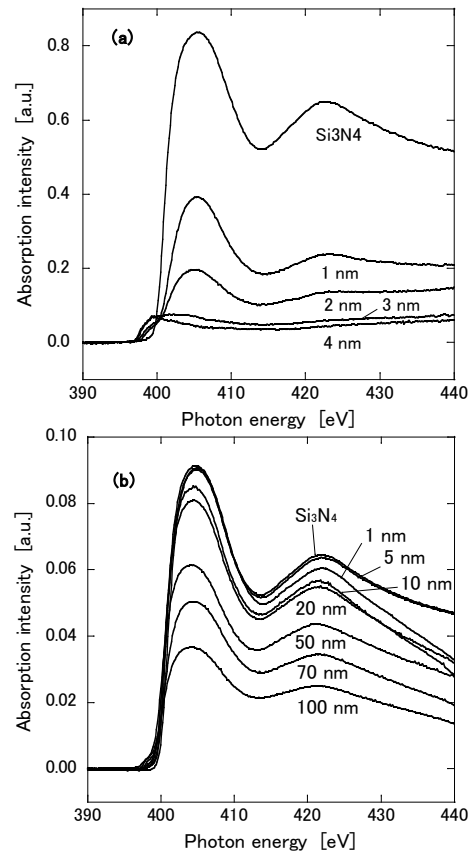


Fig. 2 N-K absorption spectra of Si_3N_4 crystal covered with Cr thin film of various thicknesses measured using the (a): TEY and (b): TFY methods.

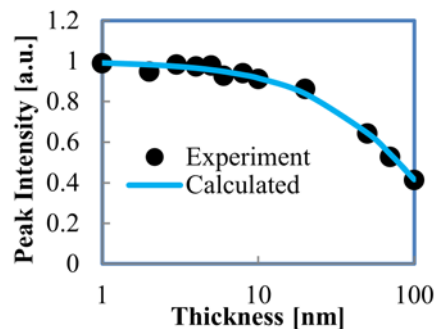


Fig. 3 Thickness dependence of peak intensity at 405 eV of N-K edge of Si_3N_4 covered with Cr film measured with the TFY method (circle) and calculated with transmittance of Cr film (line).

Characterization of Electronic States of Ion-irradiated Multi-walled Carbon Nanotubes and Multi-layer Graphenes using Soft X-ray Absorption Spectroscopy

S. Honda^{1,7}, Y. Noshō^{1,7}, A. Tsukagoshi^{1,7}, M. Niibe², and M. Terasawa^{2,7}

¹Univ. of Hyogo, ²LASTI Univ. of Hyogo

R. Hirase³, H. Yoshioka³, and H. Izumi³

³Hyogo Pref. Inst. of Tech.

K.-Y. Lee⁴

⁴National Taiwan Univ. of Sci. and Tech.

K. Niwase⁵

⁵Hyogo Univ. of Teacher Education

E. Taguchi⁶

⁶Research Center for Ultra-High Voltage Electron Microscopy, Osaka Univ.

M. Oura⁷

⁷RIKEN SPring-8 Center

Abstract

Low energy Ar ions (0.5 - 5 keV) were irradiated to vertically aligned multi-walled carbon nanotube (MWCNT) films and multi-layer graphene films. The electronic states and structural properties of the irradiated MWCNT films and graphene films were characterized by x-ray absorption spectroscopy (XAS) and Raman spectroscopy, respectively. It was found that strong dependence of the intensity of π^* peak on the incident angle of soft x-ray (α) was observed, not for the MWCNT films as-prepared. This should be due to highly oriented orbitals of π^* of multi-layer graphene films as-prepared. On the other hand, after the Ar ion irradiation to the graphene films, with increasing the ion accelerated energy and dose, dependence of height of π^* peak on the incident angle (α) is changed. This implies degradation of the alignment of layers of the multi-layer graphene films induced by the irradiation.

Introduction

Nanostructured carbon materials such as carbon nanotubes (CNTs)[1] and graphenes[2] have been extensively studied toward realization of potential nanodevice applications. Irradiation of nanostructured carbon materials with energetic particles is thought to modify their structure and properties, and are applied to process of nanodevice fabrication[3,4]. It was reported that spatially localized Ar ion irradiation of individual MWCNTs deposited on SiO₂ substrates was used for fabrication of quantum dots[5]. Moreover, Ar ion irradiation of MWCNTs enhanced the field-emission properties due to defects introduced by the ion irradiation[6]. Several analytical techniques can be used to characterize irradiated nanostructured carbon materials. Especially, XAS can characterize defects in MWCNTs introduced by the irradiation. Since XAS gives information on the density of states, it is a powerful tool to characterize change of the local electronic states of target materials[7,8]. In this study, 0.5 - 5 keV Ar ions were used to irradiate the vertically aligned MWCNT films and multi-layer graphene films, and their electronic states and structural properties were characterized by XAS and Raman spectroscopy, respectively. In addition, scanning electron microscopy (SEM) and transmission electron microscopy (TEM)

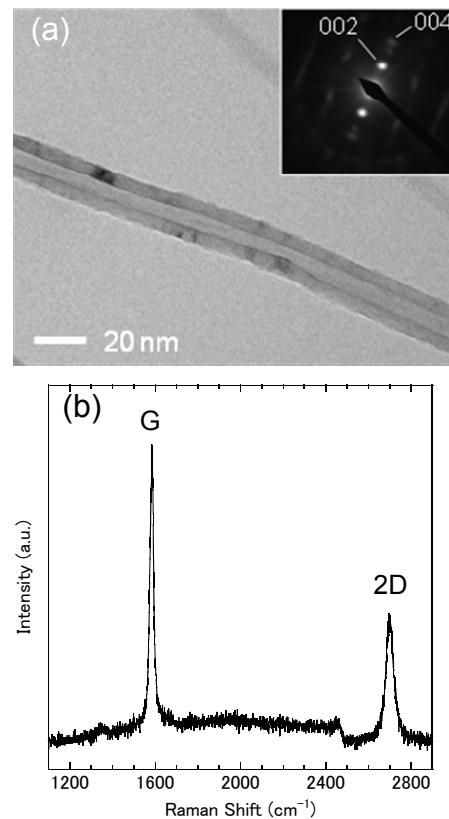


Fig. 1. (a) TEM image of a MWCNT. The inset of (a) shows selected area electron-diffraction pattern. (b) Typical Raman spectrum of multi-layer graphene films.

were utilized to characterize structural properties of the MWCNT films and the multi-layer graphene films.

Experiments and Results

Vertically aligned MWCNT films and multi-layer graphene films were synthesized by thermal catalytic chemical vapor deposition. Figure 1(a) shows a transmission electron microscopy (TEM) image of the MWCNT. The inset of Fig. 1(a) shows a selected area electron-diffraction pattern of the MWCNT. The average length and the diameter of MWCNTs were 160 μm and 23 nm, respectively. We employed electron cyclotron resonance ion source (Pantechnik, Nanogan) at SPring-8 BL17SU[9] to irradiate the MWCNT films at room temperature (RT) with Ar ions. The incident energy ranged from 0.5 to 5 keV and the dose varied between 1×10^{13} and 1×10^{17} cm^{-2} . Micro-Raman spectra were taken with Ar ion laser (514.5 nm) using a Raman spectroscope (JASCO, NRS-2100). Figure 1(b) shows a typical Raman spectrum of as-prepared multilayer graphene films. In the spectrum, G peak (~ 1580 cm^{-1}) and 2D peak (~ 2700 cm^{-1}) are clearly seen. Number of layers of graphene films used in this study was estimated to be 3 to 5 from 2D peak position and shape of Raman spectra of graphene films as-prepared. The carbon K-edge XAS measurement was performed using BL09 of the 1.5 GeV synchrotron radiation source NewSUBARU at the University of Hyogo[10]. The total electron yield method was used for the measurement.

XAS spectra of vertically aligned MWCNT films as-prepared are shown at in Fig. 2(a). The spectra were measured at different angles of incident soft x-ray to the substrate surface (α), and normalized to their intensity at ~ 320 eV. In all the spectra, π^* peak at 285 eV and σ^* peak at 292 eV are clearly seen. Both the peaks relate to sp^2 -hybridized carbon (sp^2 -C) atoms. One should note that the intensity of π^* peak does not strongly depend on the incident angle (α). This should be due to a wavy form of the MWCNTs with an averaged orientation perpendicular to the substrate surface. Figure 2(b) shows XAS spectra of multi-layer graphene films as-prepared. Strong dependence of the intensity of π^* peak on the incident angle (α) was observed, not for vertically aligned MWCNT films as-prepared. This should be due to highly oriented orbitals of π^* . On the other hand, after the Ar ion irradiation to the graphene films, with increasing the ion accelerated energy and dose, dependence of height of π^* peak on the incident angle (α) is changed. This implies degradation of the alignment of layers of the multi-layer graphene films induced by the irradiation.

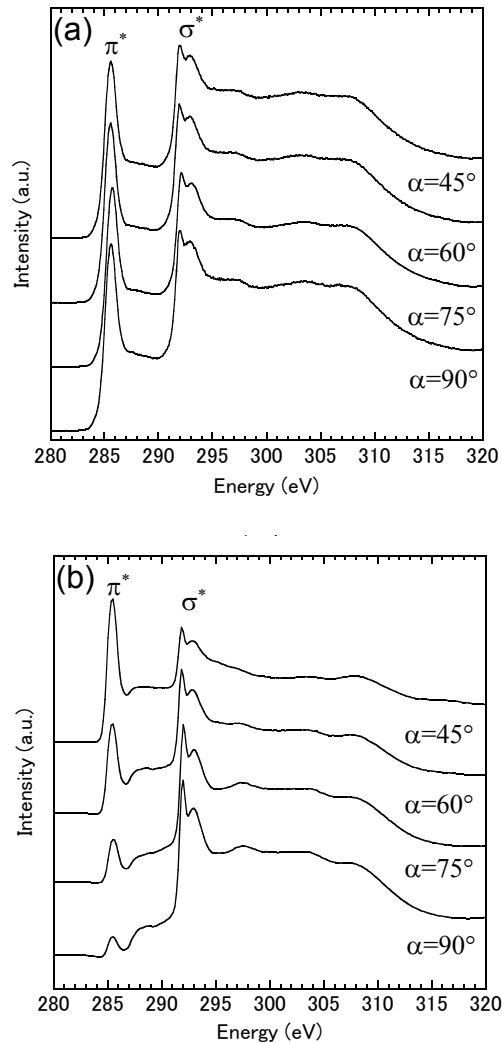


Fig.2. XAS spectra of (a) vertically aligned MWCNT films and (b) multi-layer graphene films at different angles of incident soft x-ray.

References

- [1] S. Iijima, *Nature* **354**, 56 (1991).
- [2] K. S. Novoselov *et al.*, *Science* **306**, 666 (2004).
- [3] A. V. Krasheninnikov and F. Banhart, *Nature Mater.* **6**, 723 (2007).
- [4] A. V. Krasheninnikov and K. Nordlund, *J. Appl. Phys.* **107**, 071301 (2010).
- [5] M. Suzuki *et al.*, *Appl. Phys. Lett.* **81**, 2273 (2002).
- [6] D. -H. Kim *et al.*, *Chem. Phys. Lett.* **378**, 232 (2003).
- [7] J. Schiessling *et al.*, *J. Phys.: Condens. Matter.* **15**, 6563 (2003).
- [8] T. Hemraj-Benny *et al.*, *Small* **2**, 26 (2006).
- [9] M. Oura *et al.*, *J. Synchrotron Rad.* **5**, 1058 (1998).
- [10] M. Niibe *et al.*, *AIP Conf. Proc.* **705**, 576 (2004).

Electronic structure of fluorinated diamond-like carbon thin films as a function of annealing temperature using photoelectron spectroscopy

Yuichi Haruyama, Yuji Kang, Makoto Okada, and Shinji Matsui
Laboratory of Advanced Science and Technology for Industry, University of Hyogo

Abstract

The electronic structure of fluorinated diamond-like carbon (F-DLC) thin films was investigated by the photoelectron spectroscopy. The photon energy dependence of the photoelectron spectra in the valence band region was measured from 70 to 420 eV and the orbital components of the photoelectron spectra in the valence band region were clarified. In addition, the chemical composition of the F-DLC thin films as a function of the annealing temperature were determined by the measurements of photoelectron spectra in the F 1s and C 1s core-levels. Based on the results of the photoelectron spectroscopy measurements as a function of the annealing temperature, the electronic structure of the F-DLC thin films is discussed.

Introduction

The study of diamond-like carbon (DLC) thin films has attracted much attention for wide applications because of the films' interesting properties, such as low friction coefficient, high hardness, and chemical inertness [1]. Since doping the fluorine into DLC thin films reduces the surface free energy, the fluorinated diamond-like carbon (F-DLC) thin films have an additional property such as high detachability, as well as high hardness and chemical inertness. In the field of nanoimprint lithography, F-DLC thin films have been used as an anti-sticking layer of nanoimprint mold, for example [2]. In the previous study, the hardness and the contact angles of a water drop in the F-DLC thin films were evaluated. In addition, the chemical composition and components of the F-DLC thin films were also evaluated by the measurements of X-ray photoelectron spectrum. However, it was pointed out that the thermal stability in the F-DLC thin films was changed, depending on the temperature. Although the temperature of the F-DLC thin films is one of the critical parameters to control their property, the annealing effect on the F-DLC thin films has not been fully understood at present. Therefore, it is important to clarify the electronic structures such as the chemical composition and components on the F-DLC thin films as a function of the annealing temperature.

Experiments and Results

All photoelectron measurements were performed on a BL7B end station at the NewSUBARU facility, University of Hyogo. The photoelectron spectra were measured in an analysis chamber mounted with a hemispherical electrostatic spectrometer (VSW Ltd, CL150). The synchrotron radiation with $h\nu$ between 70 and 420 eV and the Mg $K\alpha$ line ($h\nu = 1253.6$ eV) were used as the excitation source and were incident at 45° with respect to the surface normal. The total energy resolutions were about 0.7 eV for the C 1s core-level regions. Gold films evaporated on copper sample holders and F-DLC films were used for the Fermi level measurements and the total energy resolution reference. The F-DLC thin films were formed on the Si wafers using the RF plasma methods with the RF frequency of 13.56 MHz. The trifluoromethane gas was used during the deposition of the F-DLC thin films. The thickness of F-DLC films was ~ 0.3 μm . The F-DLC films were exposed once in air and led to the photoelectron analysis chamber for photoelectron measurements. Sample annealing was performed in the sample preparation chamber, which was connected to the photoelectron analysis chamber via a manual valve. The F-DLC films were annealed from RT up to 700°C with the electron bombardment behind the sample and the annealing temperature of the F-DLC films was measured with the thermocouple.

Fig. 1(a) shows the photoelectron spectra of the valence band region in F-DLC thin films as a function of $h\nu$. Five peaks at ~ 36 , ~ 20 , ~ 16 , ~ 12 , and ~ 7 eV were observed at $h\nu = 70$ eV. Two peaks at ~ 16 and ~ 12 eV were larger than three peaks at ~ 36 , ~ 20 , and ~ 7 eV. With increasing $h\nu$ from 70 to 420 eV, the intensity of two peaks at ~ 36 and ~ 20 eV increased gradually while the intensity of the peak at ~ 7 eV decreased. According to Yeh and Lindau, the photoionization cross section of the F 2p state at $h\nu = 70$ eV is larger than that of the C 2s, C 2p, and F 2s states. Therefore, two peaks at ~ 16 and ~ 12 eV are predominantly derived from the F 2p state. With increasing $h\nu$, the photoionization cross section of the C 2s and F 2s states increased gradually as compared to that of the F 2p state. At $h\nu = 420$ eV, the photoionization cross section of the F 2s state became larger than that of the F 2p state. These indicate that the two peaks at ~ 36 and ~ 20 eV are predominantly derived from the F 2s and C 2s states, respectively. On the other hand, the peak at ~ 7 eV is

predominantly derived from the C 2p state since the C 2p state increased gradually as compared to that of the F 2p state with increasing hv. In Fig. 1(b), the photoelectron spectrum of the valence band region in F-DLC thin films was compared with that of the DLC thin films and of the polytetrafluoroethylene (PTFE). Although the spectral feature in F-DLC thin films resembles that of PTFE, the intensity of the peaks at ~20 and 7 eV is larger than that of PTFE. The spectral feature in F-DLC thin films is different from that of the DLC thin films. The difference of the spectral feature between F-DLC and DLC thin films is related to the contribution of the F 2s and 2p states since the photoionization cross section of the F 2s and F 2p states was larger than that of the C 2s and C 2p states in this photon energy. In the previous photoelectron spectroscopy study in DLC thin films, the spectral features between 22 and 12 eV and between 12 and 0 eV were predominantly derived from the C 2s and C 2p states, respectively. It is considered that the larger intensity at ~20 and 7 eV in F-DLC thin films as compared to PTFE is probably due to the contribution of the C 2s and 2p states, respectively.

Fig. 2 shows the photoelectron spectra of F-DLC thin films as a function of the annealing temperature. The annealing temperatures of F-DLC thin films are denoted beside each spectrum. There are several peaks originating from the C and F atoms in each photoelectron spectrum. Three peaks at ~690, ~290, ~40 eV are assigned to the F 1s, C 1s and F 2s core-levels, respectively while a peak at ~600 eV is assigned to Auger electrons caused by F KLL decay process. The O 1s and N 1s peaks appeared at ~530 eV and at ~400 eV was not observed at RT although the F-DLC thin films were exposed in air before photoelectron spectroscopy measurements. This indicates that the surface of the F-DLC thin films is inactive for air. After annealing at 120-400 °C, no clear change was observed as compared to the photoelectron spectrum at RT. With increasing the annealing temperature at 500 °C, the intensity of the F 1s peak at ~690 eV decreased. With further increasing the annealing temperature at 600-700 °C, the F 1s peak at ~690 eV decreased rapidly. In our previous photoelectron spectroscopy study of PTFE, the chemical composition ratios of the F atoms to C atoms (F/C) were estimated from the relative intensity of the F 1s peak to the C 1s peak. Using the identical method, the F/C chemical composition ratio at RT was estimated to be 1.36. The F/C chemical composition ratio is plotted as a function of the annealing temperature. After annealing up to 400 °C, the F/C chemical composition ratio was retained between 1.27 and 1.42. With increasing the annealing temperature at 500 °C, the F/C chemical composition ratio decreased to 1.17. After annealing at more than 600 °C, the F/C chemical composition ratio decreased markedly. The F/C chemical composition ratio decreased to 0.14 at 700 °C. These results indicate that the F-DLC thin films were stable at less than 400 °C and that the content of the F atoms in the F-DLC thin films decreased at more than 500 °C.

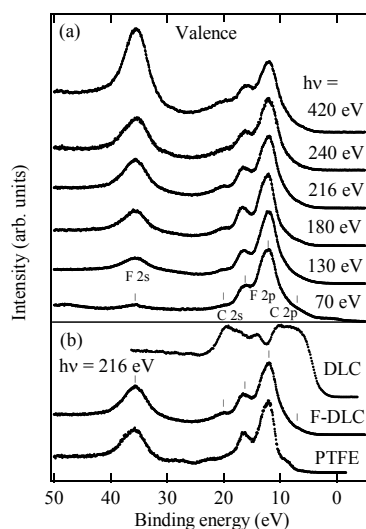


Figure 1. (a) Photoelectron spectra of the valence band region in F-DLC thin films as a function of the photon energy. (b) Photoelectron spectrum of the valence band region in F-DLC thin film was compared with that of the DLC thin film and of PTFE.

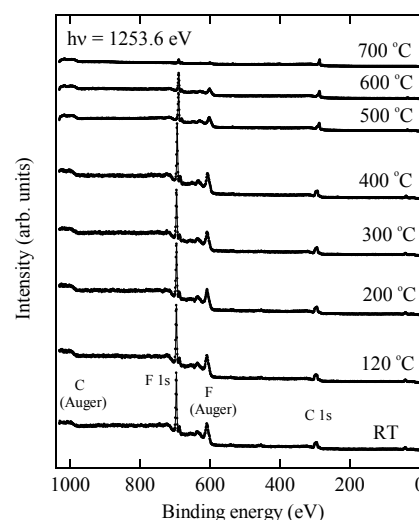


Figure 2. Wide scan of the photoelectron spectra of the F-DLC thin films as a function of the temperature. The photoelectron spectra in this figure were normalized by the C 1s peak intensity.

References

- [1] J. Ullmann, Nucl. Instrum. Methods Phys. Res., Sect. B **127** (1997) 910-917.
- [2] N. Yamada *et al.*, Jpn. J. Appl. Phys. **46** (2007) 6373-6374.

***K* and *L*-edge Spectra of Several Sulfur Compounds**

T. Hasegawa¹, M. Uemura¹, T. Tanikawa², S. Fukushima³, M. Motoyama⁴ and K. Kanda⁴

¹ Synchrotron Analysis L.L.C., 3-2-24 Wadamia-dori, Hyogo-ku, Kobe, Hyogo 652-0863 Japan

² Kansai Research Center, Forestry and Forest Products Research Institute, Nagaikyutaro-68, Momoyama, Fushimi, Kyoto 612-0855 Japan

³ National Institute for Materials Science, 1-2-1 Sengen, Tsukuba-shi, Ibaraki, 305-0047 Japan

⁴ LASTI, University of Hyogo, 3-1-2 Koto Kamigori, Ako, Hyogo 678-1205 Japan

Abstract

Sulfur can occur in many chemical forms in the bio-materials or environment, etc. Therefore, chemical state of sulfur which relates to fundamental properties is an important factor in these fields. We have tried Near Edge X-ray absorption fine structure (NEXAFS) measurement of sulfur *K* and *L*-edge of several sulfur compounds by the beamline BL05 at New SUBARU for the preliminary study of the practical analysis technique. The spectra provided a good deal of information related to oxidation state of sulfur. The usefulness of NEXAFS spectroscopy as a method of sulfur chemical state analysis was demonstrated at BL05.

Introduction

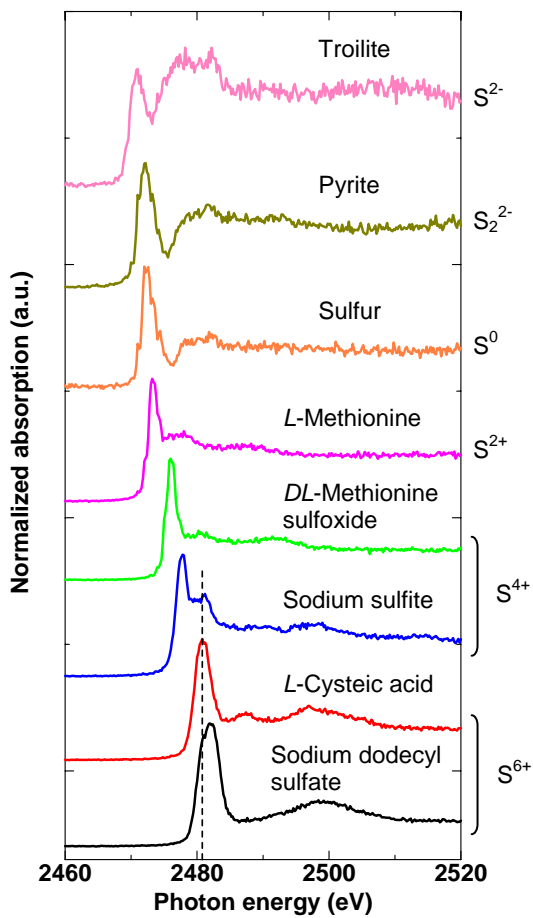
Sulfur is one of the key elements for realizing useful properties of the advanced materials, and is an important element in the field of bio-materials or environment, etc. However, it is also well known that the chemical state analysis, especially oxidation state analysis, for sulfur is not so easy, even by the X-ray absorption fine structure (XAFS) measurement. Because sulfur *K*-edge exists on the soft X-ray region (around 2.47 keV), the example of practical analysis using *K*-edge XAFS has not been reported so frequently. In addition, the measurement of *L*-edge which one can expect to get the more close information about the chemical state is seldom reported. Based on these points, we have tried NEXAFS measurement of *K* and *L*-edge of sulfur by the beamline BL05 (beamline for industrial use) at New SUBARU, University of Hyogo [1], for establishing the base of practical analysis technique. BL05 will be managed and maintained by the Synchrotron Analysis L.L.C. (SALLC), which is composed of the industrial companies, in cooperation with the staffs of the Laboratory of Advanced Science and Technology for Industry in University of Hyogo.

Experiments

BL05 consists of two branch lines, one is a double crystal monochromator beamline (BL05A) for the use in the higher-energy region (1300-4000 eV) and the other is a varied line spacing plane grating (VLSPG) monochromator beamline (BL05B) for the use in the lower-energy region (50-1300 eV). The NEXAFS spectra were measured by fluorescent X-ray yield (FLY) method for *K*-edge in BL05A, and total electron yield (TEY) method for *L*-edge in BL05B. For the FLY measurement, silicon drift detector (SDD, Vortex) was used. The high purity powdered reagents were used as the measured samples, and were diluted with the hexagonal boron nitride (*h*-BN) powder so that the concentration of S atoms may consist with 2% or less for the measurement of *K*-edge. The powdered samples were mounted to the holder with indium foil or double side adhesive conductive carbon tape.

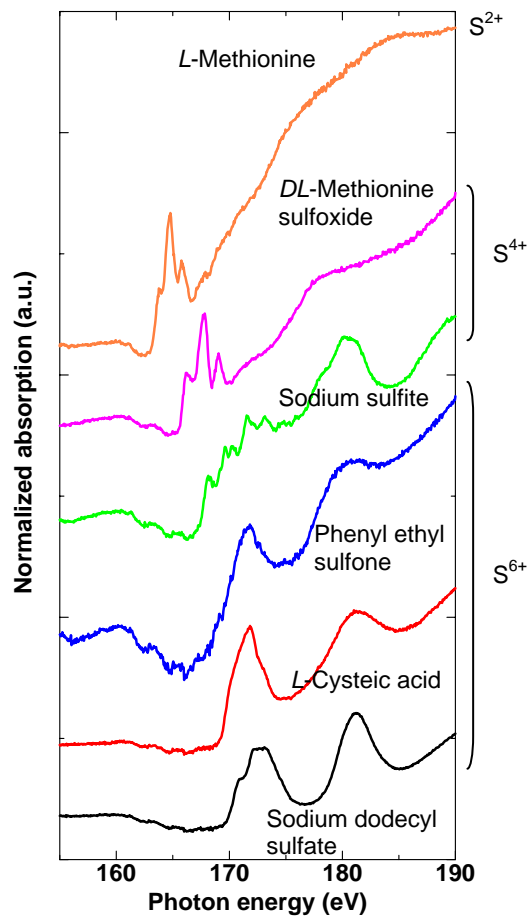
Results

In Fig.1-2, the measured sulfur *K* and *L*-edge NEXAFS spectra of several sulfur compounds are shown. These spectra have been normalized to I_0 and had a linear pre-edge background removed. *K*-edge NEXAFS spectra show good correspondence of strong peak position to the oxidation state of sulfur. The changes of energy position and spectral shape corresponding to the environments of sulfur atom can be seen in *L*-edge NEXAFS spectra. We inferred from *K* and *L*-edge NEXAFS spectra that sulfur in sodium sulfite is partially oxidized, and changes to sulfate (S^{6+} state) due to the radiation damage. In addition, it turned out *DL*-methionine sulfoxide (S^{4+}) is hard to receive the radiation damage, so this compound should be a good practical reference material of S^{4+} state. Considering the circumstances mentioned above, the chemical state analysis of sulfur in organic materials should be possible practically by means of the measurement of both *K* and *L*-edge spectra.



Incident angle at sample surface :
45 deg

Fig 1. S *K*-edge NEXAFS spectra recorded in FLY of sulfur compounds.



Incident angle at sample surface :
90 deg

Fig 2. S *L*-edge NEXAFS spectra recorded in TEY of sulfur compounds.

Reference

- [1] T.Hasegawa *et al.*, *Advances in X-ray Chem. Anal. Jpn.*, **41**, pp.99-106 (2010) [in Japanese].

Crystallization Mechanism of a-SiGe Graded Film by Soft X-ray Irradiation

Shota Kino, Yuki Maruyama, Akira Heya, Kazuhiro Kanda and Naoto Matsuo
University of Hyogo

Abstract

We proposed novel low-temperature crystallization of a-Ge, a-Si and a-SiGe films by the SR soft X-ray irradiation at storage-ring current of 25-220 mA and dose quantity of 50 mA · h. Crystallization mechanism of SiGe graded film by soft X-ray irradiation was investigated as compared with crystallization of 50nm Si_{1-x}Ge_x film. It is found that SiGe graded film was indicated the same pattern for SiGe film with 50nm thickness.

Introduction

It is important to fabricate high-quality semiconductor materials on plastic substrate at low temperature for seat computer. Thin-film transistors (TFTs) are popularly applied to a switching device for flatpanel displays (OLED displays). Recently, germanium is expected as an attractive material to realize the TFT with a high mobility [1]. Crystallization methods induced excimer laser, Ar⁺ laser, green laser and hard X-ray have been reported for low temperature crystallization. So far, the relationship between electron excitation followed by atom migration process, thermal process and the storage-ring current has reported to previous work [2, 3]. In this study, we investigated crystallization of SiGe with different Ge fraction and crystallization of SiGe graded film.

Experiments and Results

Amorphous Si (a-Si) films were deposited by plasma-enhanced chemical vapor deposition (PECVD) method and a-Ge and a-Si_{1-x}Ge_x (x=0.2 0.4 0.5 0.6 and 0.8) were deposited by molecular beam deposition (MBD) method (deposition rate: 0.02 nm/s, base pressure: ~10⁻¹⁰ Torr). The thickness of a-Si, a-Ge and a-SiGe film was 50 nm. In addition, we prepared a-SiGe graded film by MBD. Graded film was deposited different composition of Si_{1-x}Ge_x (x=0.2, 0.4, 0.6 and 0.8) with each 50nm film thickness, and the total film thickness was 200nm. The irradiation of soft X-ray was carried out at BL07A of NewSUBARU. The light source of BL07A was the 3m undulator. The electron energy of the NewSUBARU ring was 1.0 GeV during this experiment. The storage-ring current, photon energy and dose quantity were 100 mA, 50 eV and 50 mA · h respectively. The characteristics of the film were measured by X-ray diffraction (XRD), reflection high energy electron diffraction (RHEED) and Raman spectroscopy.

The crystalline fraction of Si_{0.2}Ge_{0.8}, Si_{0.4}Ge_{0.6} and Si_{0.6}Ge_{0.4} were 85%, 70% and 21%, respectively. When the fraction of Ge in SiGe film was high, crystalline fraction was high and crystallization area was large. Si_{0.8}Ge_{0.2} did not crystallize. Figure 1 shows the optical image of a-SiGe graded film irradiated by same conditions. Crystallization area was center of color changed area and the color-changed area separated to 3 parts. The top layer (Si_{0.8}Ge_{0.2}) did not crystallize in the result of XRD and RHEED. From these results, the crystallized area for each layer was different as shown in Fig. 2. It is considered that SiGe graded film was indicated the same pattern for SiGe film with 50nm thickness. In generally, the temperatures of crystallization for Si and Ge using conventional thermal annealing are 680°C and 500°C [4], respectively. And Ge has higher photoionization cross-section than Si. Therefore, crystallization of bottom layer with high fraction of Ge was enhanced. It is expected that the SiGe graded film with various composition of a-SiGe and poly-SiGe will become excellent material for solar cells.

References

- [1] T. Sadoh et al., Jpn. J. Appl. Phys., **46** (2007), pp. 1250-1253.
- [2] Y. Nonomura et al., AM-FPD'11 (2011) pp.193-196
- [3] S. Kino et al., AM-FPD'12 (2012) pp.223-226
- [4] I. Nakao et al., IEICE SDM2008-17, pp.83-88, 2008.

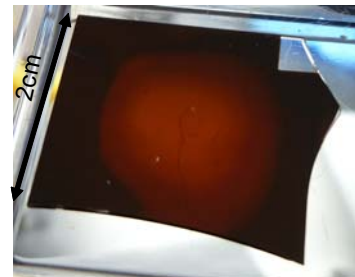


Fig. 1 Optical image of SiGe graded film after soft X-ray irradiation.

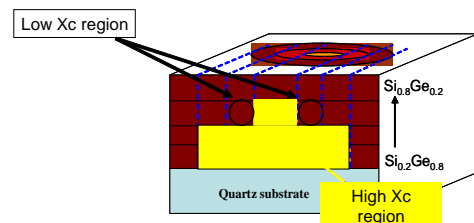


Fig. 2 Cross sectional diagram for crystallization area of SiGe graded film by soft X-ray irradiation.

Thermal Durability of FIB-DLC Films Containing W

Akihiro Fujimoto^a, Makoto Okada^a, Yuji Kang^a, Shinji Matsui^a, Tsuneo Suzuki^b, and Kazuhiro Kanda^a

^a LASTI, University of Hyogo, Kamigori, Hyogo 678-1205, Japan,

^b Extreme Energy-Density Research Institute, Nagaoka University of Technology, Nagaoka, Niigata 940-2188, Japan

Abstract

Diamond-like carbon film containing W (W-DLC) was fabricated by focused-ion-beam chemical-vapor deposition (FIB-CVD), and its thermal durability was investigated using x-ray absorption fine structure near the carbon K-edge (C–K NEXAFS) spectroscopy and a combination of Rutherford backscattering and elastic recoil detection analysis in comparison with those of commercial DLC and W-DLC films. The concentration of W in the films did not decrease when the annealing temperature was increased, while the concentration of H did. The W-DLC film fabricated by FIB-CVD unchanged after annealing for 32 h at 873 K in vacuum. Its thermal durability was comparable to that of the commercial films.

Introduction

Use of diamond-like carbon (DLC) devices fabricated by focused-ion-beam chemical-vapor deposition (FIB-CVD) for electrochemical applications requires high electrical conductivity and high thermal durability because Joule heating occurs when electric current passes through a nano-device. Incorporation of W into DLC film was known to improve the film's thermal durability. Previous work showed that the electrical conductivity of W-DLC fabricated by FIB-CVD using $W(CO)_6$ as the W source is in the range 2.5 to $6.3 \times 10^3 \text{ Sm}^{-1}$.¹⁾ It is sufficiently high for W-DLC to be used for fabricating three-dimensional nano-devices. Therefore, the thermal durability of W-DLC fabricated by FIB-CVD must be improved for it to be in electrochemical applications. In the present study, we investigated the effect of annealing in vacuum at three temperatures ranging from 673 to 873 K on W-DLC film fabricated by FIB-CVD. The metric used for thermal durability was the residual film thickness after. The elementary composition analysis was performed using a combination of RBS and ERDA techniques. The effect of annealing on the W-DLC films fabricated by FIB-CVD was compared to the effect on commercial DLC films for industrial use.

Experiments

The W-DLC films were fabricated on Si substrates using a FIB-CVD apparatus (SII Nano Technology Inc.; SMI2050MS2).^{2,3)} Phenanthrene ($C_{14}H_{10}$) and tungsten carbonyl ($W(CO)_6$) were used as starting materials. The ion source was Ga^+ , and the beam current was 20 nA. Several commercial DLC and W-DLC films were fabricated for comparison. The samples were annealed in a furnace (Thermo RIKO Co. Ltd; GFA430) under vacuum conditions ($Pa \leq 10^{-4}$). The annealing temperature was 673, 773, or 873 K, and the annealing time was 32 hours. RBS and ERDA with MeV- He^+ irradiation were performed using an electrostatic accelerator (Nisshin-High Voltage Co. Ltd.; NT-1700HS) located in the Extreme Energy Density Research Institute at the Nagaoka University of Technology.⁴⁾ The He^+ beam was accelerated to 2.5 MeV, and the incident beam angle with respect to the surface normal was 72° . The film thickness was determined by measurement of the RBS spectrum.

Results and Discussions

The residual Ga in nanodevices fabricated by FIB-CVD is transferred to the surface, where it produces Ga spheres that are vaporized from the film by annealing.^{5–8)} Fig. 1 shows the dependence of the Ga concentration in the W-DLC and DLC films fabricated by FIB-CVD on the annealing temperature, as determined by RBS measurement. “FIB-CVD W-DLC1” indicates the W-DLC film prepared by FIB-CVD in the present work and “FIB-CVD W-DLC2” and “FIB-CVD DLC” indicate the W-DLC film and DLC film prepared by FIB-CVD in the previous work.⁹⁾ Figs. 2 (a)–(c) show the dependence of the H concentration in the DLC and W-DLC films on the annealing temperature, as estimated using a combination of ERDA and RBS techniques. The Ga and W concentrations in the as-deposited W-DLC film fabricated by FIB-CVD in the present work were $\approx 5.5\%$ and $\approx 0.1\%$, respectively. The W concentration in the commercial UBMS W-DLC was

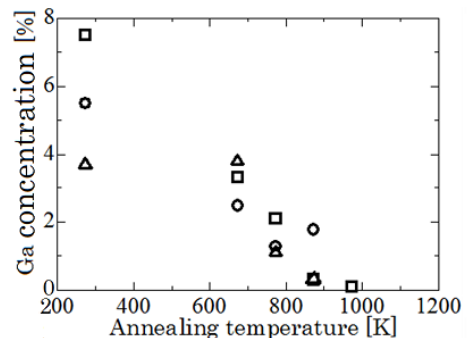


Fig. 1 Dependence on annealing temperature of Ga concentration in W-DLC and DLC films fabricated by FIB-CVD. Circles represent data for FIB-CVD W-DLC1 film fabricated in present work, squares represent data for FIB-CVD W-DLC2 film fabricated in previous work, and triangles represent data for FIB-CVD DLC film fabricated in previous work. Points at 273 K indicate Ga content as-deposited.

≈4.5%, ≈20 times that in the W-DLC films fabricated by FIB-CVD.

As shown in Fig. 1, the Ga concentration in the W-DLC films and DLC films fabricated by FIB-CVD decreased with an increase in the annealing temperature, which is consistent with previous findings.^{7,10,11} The Ga concentration decreased from ≈4–8 % to ≈2 % after annealing at 773 K, and most of the Ga had evaporated after annealing at 873 K. The W concentration in the W-DLC films fabricated by FIB-CVD and in the UBMS W-CVD film did not depend on the annealing temperature. This is attributed to the very high boiling point of tungsten, 5828 K.

H concentration in the as-deposited W-DLC and DLC films in the present work was ≈20 %, except for PE-CVD DLC film, (≈40 %), as shown in Fig. 2. The H concentration in the PE-CVD DLC film decreased after annealing at 673 K and decreased steeply when the annealing temperature was increased from 773 to 873 K. The H concentration in other W-DLC and DLC films kept that of as-deposited after annealing at 673 K and it decreased when the annealing temperature exceeded 773 K. The desorbed H was considered to be emitted from C–H bonding rather than hydrogen molecules in the film, because the desorption starts at a high temperature, ≈773 K. In other words, the exodus of H from the DLC film is considered to lead to the graphitization of DLC film due to the decoupling of the C–H bonding and subsequent coupling of C=C bonding in films.^{12–14}

The dependence of the film thickness on the annealing temperature obtained from RBS measurement is shown in Fig. 3. The thickness of the W-DLC film fabricated by FIB-CVD increased when the annealing temperature was slightly increased from as-deposited to 673 K. This small increase was considered to be due to the variation of film thickness as-deposited films. The thickness decreased steeply when the temperature was increased from 673 to 773 K and this film remained when it was increased to 873 K. This demonstrates that the thermal durability of W-DLC film fabricated by FIB-CVD is higher than that of PE-CVD DLC film and lower than those of W-DLC and DLC films fabricated by UBMS. However, a part of the W-DLC film fabricated by FIB-CVD remained after annealing at 873 K.

References

- [1] S. Matsui, Nucl. Instrum. Methods. Res., Sect. B **257** (2007) 758.
- [2] J. Igaki *et al.*, Microelectron. Eng. **83** (2006) 1221.
- [3] K. Nakamatsu *et al.*, J. Vac. Sci. Technol. B **23** (2005) 2801.
- [4] J. Igaki *et al.*, Jpn. J. Appl. Phys. **46** (2007) 8003.
- [5] J. Fujita *et al.*, Jpn. J. Appl. Phys. **41** (2002) 4423.
- [6] R. Kometani *et al.*, Jpn. J. Appl. Phys., **47**, (2008) 5032.
- [7] K. Kanda *et al.*, Radiat. Phys. Chem. **75** (2006) 1850.
- [8] K. Kanda *et al.*, Trans. Mat. Res. Soc. Jpn, **36** (2011) 71.
- [9] A. Wada *et al.*, Jpn. J. Appl. Phys. **50** (2011) 06GG05.
- [10] J. Igaki *et al.*, Jpn. J. Appl. Phys. **46** (2007) 8003.
- [11] T. Nagata *et al.*, Jpn. J. Appl. Phys. **47** (2008) 9010.
- [12] K. Kanda *et al.*, Jpn. J. Appl. Phys. **41** (2002) 4295.
- [13] A. Saikubo *et al.*, New Dia. Front. Carbon Tech. **16** (2006) 235.
- [14] A. Saikubo *et al.*, Dia. Relat. Mater. **17** (2008) 1743.

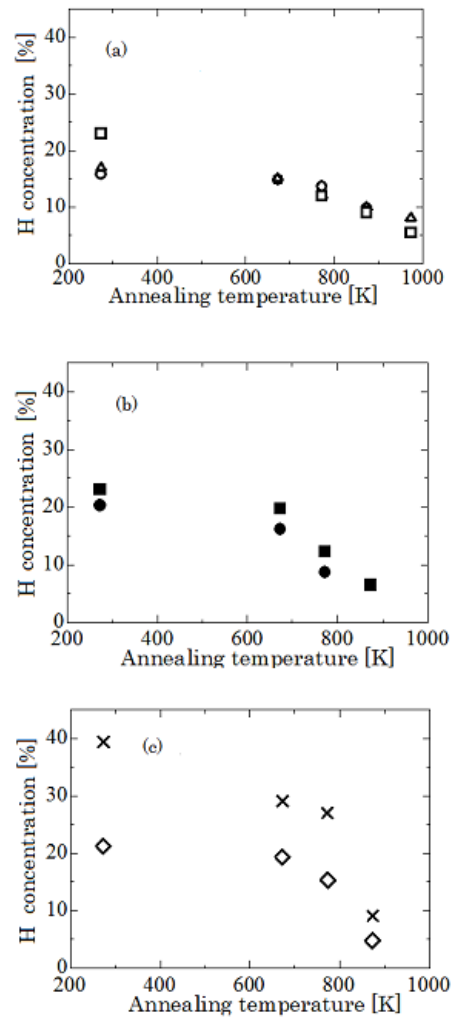


Fig. 2 Dependence on annealing temperature of H concentration: a) Circles represent data for FIB-CVD W-DLC1 film fabricated in present work, squares represent data for FIB-CVD W-DLC2 film fabricated in previous work, and triangles represent data for FIB-CVD DLC film fabricated in previous work; b) Closed circles represent data for UBMS W-DLC film and closed squares represent data for UBMS DLC film; c) Diamonds represent data for IP DLC film and crosses represent data for PE-CVD DLC film.

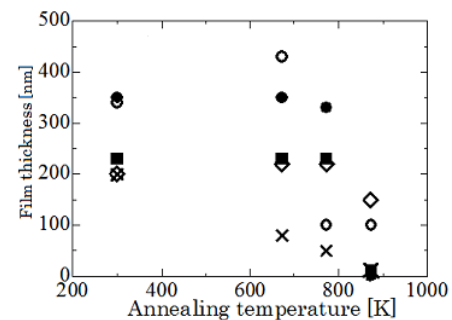


Fig. 3 Dependence on annealing temperature of film thickness obtained from RBS measurement. Circles represent data for FIB-CVD W-DLC1 film fabricated in present work, closed circles represent data for UBMS W-DLC film, closed squares represent data for UBMS DLC film, diamonds represent data for IP DLC film, and crosses represent data for PE-CVD DLC film.

Comparison of Photon Flux of a BL06 with that of the Sun

Yukinori Kawamoto^a, Kensei Kobayashi^a, Ryou Imai^b, and Kazuhiro Kanda^b

^a Graduate School of Engineering, Yokohama National University, Hodogaya-ku, Yokohama 240-8501, Japan

^b LASTI, University of Hyogo, Kamigori, Hyogo 678-1205, Japan,

Abstract

Photon flux at the sample stage of BL06 was estimated for the comparison of the solar system with the simulation experiment using BL06. Photon flux was almost 1.0×10^{10} photons/s/0.1%bw/mm² at the sample stage in the region of photon energy under 1000 eV.

Introduction

A wide variety of complex organic compounds including precursors of amino acids have been detected in carbonaceous chondrites and comets. It was suggested that organics in them were formed in quite cold environments, such as interstellar space. Irradiation of frozen mixture of possible interstellar molecules including CH₃OH, NH₃ and H₂O with high-energy particles gave complex amino acid precursors with high molecular weights. Such interstellar complex molecules would be altered by cosmic rays and solar light (UV, soft X-rays) in proto-solar nebula and interplanetary space before the delivery to the Earth by such extraterrestrial bodies as space dusts.¹⁻³⁾ We are planning to examine possible alteration of amino acids and their precursors by irradiation with photons.

BL06 in NewSUBARU was constructed for the irradiation of white beam in the soft X-ray region. The novel functional surface, whose surface properties, such as wettability, refractive index, and so on, are modified by the exposure to the SR. In addition, experiments in the astrobiology were performed to investigate the irradiation effect of soft X-ray on the molecules in the space. For the discussion on the alteration of organic compounds of interstellar origin in the solar system by the simulation experiments using SR beamline on the ground, estimation of the energy-dependent photon flux was demanded. In the present study, we calculated the photon flux in the square of 1 mm² at the sample stage of BL06.

Calculation

A bending magnet was used as a light source of BL06. The white radiation beam from a bending magnet was introduced to the sample stage using a pair of mirrors, M₀ and M₁, whose incident angle was 3°. Therefore, the photon flux at the sample stage of BL06 was represented by,

$$N = F^{SR} \cdot \varepsilon_{AC} \cdot R_0 \cdot R_1 \quad (1)$$

where F^{SR} was photon flux at the light source position in the bending magnet and ε_{AC} was the accepting efficiency. R_0 and R_1 were the reflectivity of M₀ and M₁, respectively. The photon flux at the light source position was estimated by the production of the brilliance of NewSUBARU⁴⁾ and beam size at the light source position of BL06, which was calculated to $\sigma_x = 0.17$ mm and $\sigma_y = 0.27$ by Prof. Ando. The angles at the light source position corresponding to the square of 1 mm² at the sample stage were estimated by optical trace calculation to 0.41 mrad and 0.40 mrad in the horizontal and vertical direction, respectively. These angles were much smaller than the acceptance of mask and/or M₀. The reflectivity of mirror was determined using the web calculation in the Center for X-ray Optics of the Berkeley Lab. Mirror constants of BL06 were tabulated in Table I.

Table I Mirror constants of BL06

Mirror	M0	M1
Incident angle	3°	3°
Material	SiO ₂	SiO ₂
Shape	Sagittal cylinder	Troidal
Coating material	Pt	Pt
Coating thickness	50 nm	50 nm
Surface roughness	0.299 nm RMS	0.295 nm RMS

Results and Discussions

The determined energy-dependent photon flux was showed in Fig. 1. Photon flux was almost 1.0×10^{10} photons/s/0.1%bw/mm² at the sample stage in the region of photon energy under 1000 eV. In addition, the photon flux in the 1.0 GeV of ring electron energy is almost same that in the 1.5 GeV. Photon flux decreased steeply with increasing photon energy beyond 1000 eV. This decreasing was dominantly ascribable to the decrease in the mirror reflectivity.

We can compare the simulation experimental results using SR beamline with the solar system in the various conditions, by the use of the present calculation results. As sample, Fig. 2 shows the luminance at the sample stage of BL06 with that in the revolution orbit of the Earth from the sun of the present age. As shown in Fig. 2, the simulation experiment using BL06 has a large acceleration factor.

Acknowledgement

The authors thank Prof. Miyamoto for his polite instruction for the calculation on the photon flux.

References

- [1] K. Kobayashi, T. Ogawa, et. al., *Electr. Eng. Jpn.*, 91 (3), 293-298 (2008).
- [2] G. A. Gusev, K. Kobayashi, et. al., *Origins Life Evol. Biosph.*, 38, 509-515 (2008).
- [3] J. Takahashi, K. Kobayashi, H. Mita et. al., *Int. J. Mol. Sci.* 10(5), 3044-3064 (2009).
- [4] A. Ando et. al., 1997 Proc. IEEE Particle Accelerator Conf. (Vancouver) 757.

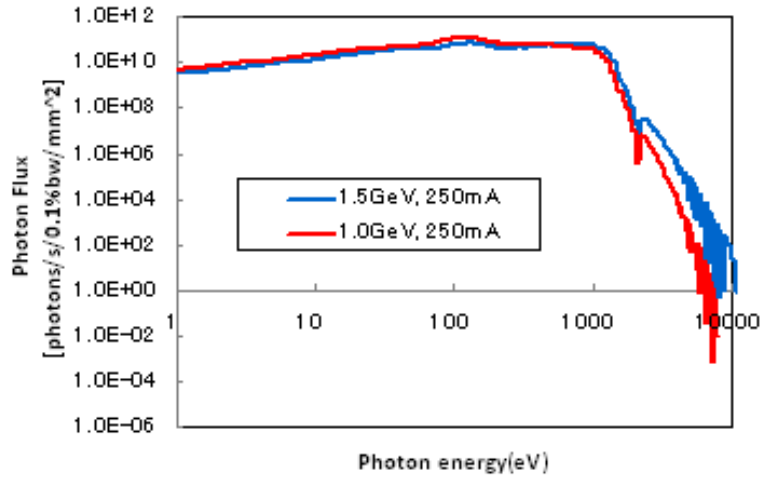


Fig. 1 Photon flux in the BL06

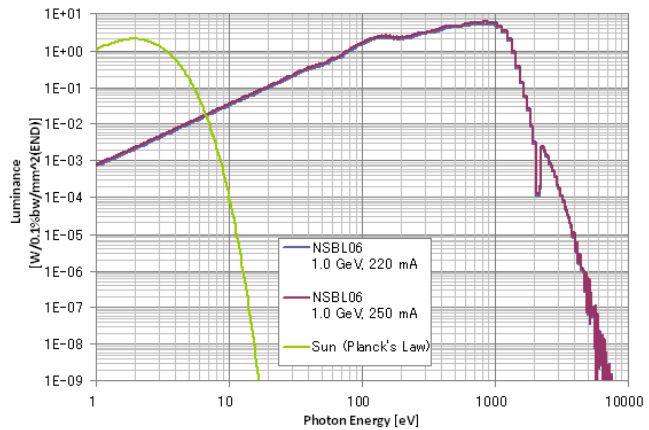


Fig.2 Luminance of BL06 and the sun

Stability and alteration of amino acids and related compounds against soft X-rays in interplanetary space

Yukinori Kawamoto¹, Takuto Okabe¹, Midori Eto¹, Yumiko Obayashi¹, Takeo Kaneko¹, Jun-ichi Takahashi², Hajime Mita³, Kazuhiro Kanda⁴, Kensei Kobayashi¹

¹Yokohama National University, Yokohama, Japan, ²NTT, Isehara, Japan,

³Fukuoka Institute of Technology, Fukuoka, Japan, ⁴University of Hyogo, Kamigori, Japan

Abstract

In order to examine stability and possible stability of bioorganic compounds in space environments, target molecules (amino acids, amino acid precursors, nucleic acid bases) were irradiated with soft X-rays from NewSUBARU BL-6 in a solid state under high vacuum. Free amino acids were less stable than their precursors. Water-insoluble products were produced by irradiation. Changes in structure by irradiation was studied by C-XANES with NewSUBARU BL05.

Introduction

Prebiotic organic matters such as amino acids have been found in extraterrestrial bodies. It was suggested that they were formed in cold space environment, and were delivered to the early Earth. Interplanetary dust particles (IDPs) were promising carriers since they could deliver organics safer than large meteorites or comets. On the other hand, IDPs are so small that they are directly exposed to the solar radiation, which may decompose or alter organic molecules in IDPs. In the present study, we evaluated the stability of amino acids, their precursors, and RNA bases against soft X-rays and extreme ultraviolet light (EUV): Irradiation was performed at NewSUBARU BL-06 (Univ. Hyogo), and the irradiation products were analyzed by several methods including HPLC and C-XANES.

Experiments and Results

Six amino acid-related samples - Glycine (Gly), alanine (Ala), hydantoin (Hyd: precursor of glycine), isovaline (Ival), 5-Ethyl-5-methylhydantoin (EMHyd: precursor of isovaline) and complex organic compounds synthesized by proton irradiation of a mixture of CO, NH₃ and H₂O (referred to as CAW) – and 4 RNA bases were irradiated with continuous light from soft X-rays to IR (hereafter referred as to soft X-rays) at NewSUBARU BL-06 (University of Hyogo) under high vacuum condition. After collecting the irradiated sample with pure water, we measured the recovery ratio of each compound by using ion exchange or reversed-phase HPLC systems. In some cases, CaF₂ window was used to cut soft X-rays and EUV (referred as to VUV irradiation; cut-off wavelength is ca. 130 nm).

Amino acids or their precursors were gradually decomposed by soft X-rays irradiation, and water-insoluble organics were formed. The water-insoluble products could mostly dissolved in dichloromethane. Recovery of the amino acid precursors (Hyd, EMHyd, and CAW) was much more than that of the free amino acids (Gly, Ival) after soft X-rays irradiation. Thus, we could suggest that the precursor amino acids are likely to present more stable than free amino acids in space environment such as meteorite surface and in IDPs. Neither racemization nor formation of glycine was observed even after 99 % of the initial L-alanine was decomposed. RNA bases were more stable than amino acids and their precursors against irradiation.

When CaF₂ window was used, little insoluble matters were formed. Thus, soft X-rays (including EUV) are responsible for the formation of insoluble organics. Soft X-rays fraction in the solar radiation is small in the present time, but it is supposed that the strong X-rays were emitted from the young Sun before the formation of planetesimals. It should be examined the possible formation of insoluble organic matter, that is now found in carbonaceous chondrites and comets, by the irradiation with high-energy photons from the young Sun.

After irradiation, amino acids and their precursors gave water-insoluble products. We measured C-XANES spectra of the isovaline and CAW before and after soft X-rays irradiation to see possible alteration processes in space. C=O peaks in C-XANES spectra of both materials decreased after irradiation, while C=C peaks increased.

Amino acids and their precursors are going to be exposed to actual space environment by utilizing the Exposed Facility of JEM, ISS. The mission named the Tanpopo is now scheduled to start in June, 2014 [1].

References

[1] A. Yamagishi, et al., *Trans. JSASS Space Tech.*, **7**, Tk49-55 (2009).

Effective Modification in Silica-Based Films by Synchrotron Radiation

K. Moriwaki, T.Haraguchi, Graduate School of Eng./ Kobe Univ.,
K.Kanda, S.Matsui, LASTI/Univ. Hyogo, and K.Watanabe, Photonics Labs/NTT

Abstract

Undulator radiation (UR) or synchrotron radiation (SR) by the NewSUBARU is used to change the refractive index in silica-based films for optical waveguide devices. Irradiated samples are shown to have a large refractive-index change of 10^{-2} order. Defects in the glass induced by the irradiation are characterized by optical absorption measurements as the major causes for the refractive-index change. As the results, UR with peak energy of 50eV or 60eV in the first order is found to be more effective to induce the defects in GeO₂-doped SiO₂ sputtered-films than any other peak energies of 80 or 100 eV. In addition, those UR-induced defects are found to concentrate within a 200nm-deep layer from the surface. Those defects are stable up to around 300°C annealing, although they disappear after 800°C annealing.

Introduction

We use synchrotron radiation (SR) and undulator radiation (UR) for photo-induced refractive-index modifications in silica-based glasses for optical waveguide devices¹⁾. Our main objectives are to induce large refractive-index changes more effectively using SR without a spectrometer or UR, and to investigate their origins depending on wavelengths of SR or UR spectra. Especially, UR would be a very useful tool for the materials modifications, because it can select a useful wavelength and it has very high intensity. Their UR characteristics would make materials modified effectively with a very short processing time. For those reasons we mainly use UR for the materials modifications in this report. Our previous results¹⁾ showed that a high refractive index change by SR irradiation was obtained, but the origins are not so clear at the present stage. As one of the major causes of the refractive-index change is defects induced by SR or UR, we characterized the optical absorption changes by SR or UR induced defects, and their depth distributions. This report shows the results related to the defects for GeO₂-doped SiO₂ glass which is used for optical waveguide devices.

Experiments and Results

Experimental conditions are almost the same as in the previous experiments¹⁾. UR (from the NewSUBARU BL-7A) was used to investigate irradiation-wavelength effects. SR (from the NewSUBARU BL6) was also irradiated on samples directly without a spectrometer. The electron energy of the SR was 1GeV. GeO₂-doped SiO₂ fabricated by sputtering on Si or on pure silica substrate were used in our experiments. Optical absorption measurement (wavelength range of 190-400nm) was used to characterize defects induced by SR or UR. Pure silica substrate was used for an optical absorption measurement.

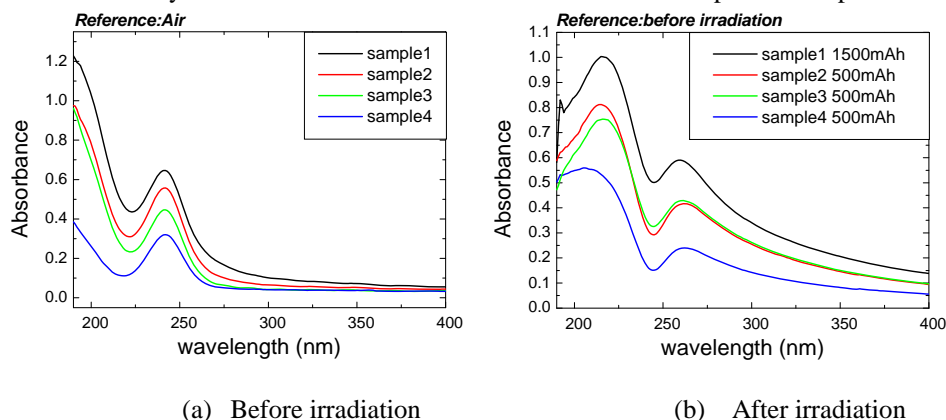


Fig.1 Optical absorbance for (a) before and (b) after UR-irradiated samples (from 1 to 4) of GeO₂-doped SiO₂ film on silica substrate. The UR peak energy is 50eV. Each sample has different amount of original defects which are shown in the spectra in (a). The amount of defects after the irradiation depends on the original ones.

Typical optical absorption spectra for samples of GeO₂ doped SiO₂ films on silica substrates are shown in Fig.1. The spectra in Fig.1 are by four samples which have different amount of original defects before the irradiation. The original defects can be seen in Fig.1(a) which shows that the number 1 sample has the largest amount of defects. Basically large amount of original defects makes the absorbance difference after the irradiation higher as shown in Fig.1(b). Figure 1 (b) also shows that a peak of 242nm is decreased and two peaks around the 242 nm (higher and lower one) appear. The 242nm peak would be attributed as GODC (Germanium Oxygen deficient-type center). The lower peak near 242nm would be attributed as a combination of GEC (Ge Electron trapped Center, 215nm) peak and Ge E' center (193nm) peak which originates from a lone-pair-related defect. In order to characterize an amount of the defects, the combination-peak heights of 193nm and 215nm are used and plotted in Fig.2 with various UR peak energy and dose, including a reference by SR irradiation. Figure 3 shows that the most effective peak energy to induce defects in the experimental data is 50 eV or 60eV. SR irradiation is not so effective in the Fig.3, because the SR intensity is relatively weak compared to that by UR.

In Fig.3, Ar ion etching is used to remove the surface layer for depth-profile characterizations. After a 200 nm-deep etching, absorbance spectra are decreased drastically, but further etching up to 500 nm does not change the absorbance as shown in Fig.3. As the results, the UR-induced defects have been found to concentrate within a 200nm-deep layer from the surface.

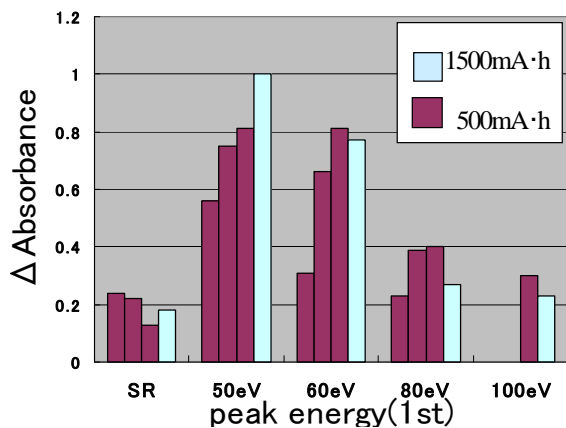


Fig.2 The amount of defects appeared in the absorbance spectra for four samples with two doses after UR-irradiation of 50-100 eV peak energies with reference by SR irradiation.

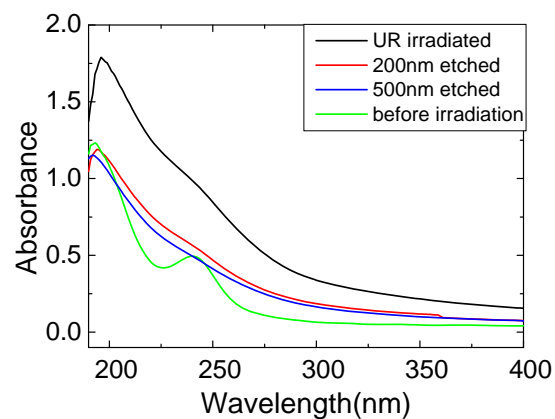


Fig.3 Absorbance spectra for samples before, after UR-irradiation of 50eV peak energy and after etching (270nm and 500nm-deep from the surface).

Thermal stability and relaxation characteristics for the UR-induced defects were also measured by annealing the irradiated samples at temperature range from 300 to 1000°C. The absorbance of the glass films were increased a little bit but almost stable by an annealing at 300°C or 400°C after UR irradiation. After annealing more than 800°C, the absorption spectra became almost the same as the original ones before the irradiation because of relaxation.

Conclusions

An effective tool for refractive index change is investigated for an application of SiO₂ based materials to optical waveguide devices. SR or UR-induced defects are the causes of refractive index change. UR with peak energy of 50eV or 60eV in the first order was found to be more effective to induce the defects in GeO₂-doped SiO₂ sputtered-films than that with any other peak energies of 80 or 100 eV. Those UR-induced defects were found to concentrate within a 200nm-deep layer from the surface. Those defects were stable up to around 300°C annealing, so that thermally-stable devices could be fabricated.

From those results, UR is expected to be an effective irradiation source for the refractive-index change in optical waveguide devices

References

[1] K.Moriwaki *et al.*, LASTI Annual Report vol.10 (2008).

Release property of thin PDMS layer for UV nanoimprinting

Makoto Okada, Yuichi Haruyama, Kazuhiro Kanda, and Shinji Matsui
Laboratory of Advanced Science and Technology for Industry, University of Hyogo, Japan

Abstract

UV-nanoimprint lithography (NIL) is used to fabricate high-throughput, low-cost, high-resolution nanostructure devices. The nanoimprint mold is typically coated with an antisticking layer to ensure easy separation of the mold from the UV nanoimprint resins. This layer must be highly durable to meet the demands of a manufacturing environment, and F-ASL is the standard type used. In this study, we focused on using PDMS as the antisticking layer for nanoimprinting and examined its antisticking capabilities. Experimental results showed that the thin PDMS layer functions comparably to the fluorinated-antisticking layer as an antisticking layer.

Introduction.

Nanoimprint lithography¹⁻³⁾ is a promising and cost-effective ultrafine lithography technique. The nanoimprint molds come into direct contact with the resins used, so an antisticking layer is coated on the molds to prevent resin adhesion. Generally, a fluorinated antisticking layer (F-ASL) is used for nanoimprinting. Polydimethylsiloxane (PDMS) has heat durability, chemical stability, and a release property, and we focused on using a thin PDMS layer^{4, 5)} as the antisticking layer for nanoimprinting. In this study, we examined the thin PDMS layer's antisticking capabilities.

Evaluation of thin PDMS layer

We used P7266-DMS (Polymer Source Inc.) for the thin PDMS layer coating. The coating process is as follows.: (1) The substrate surface was cleaned with an ozone cleaner (SKB401Y-01: SUN ENERGY Co.), this producing the hydroxyl groups. (2) The P7266-DMS was spin-coated on the substrate. (3) The substrate was annealed at 200 °C in a vacuum at 1.0×10^{-3} Pa for 10 h. (4) After annealing, the substrate was rinsed with toluene to remove the excess P7266-DMS.

We compared the thin PDMS layer to a F-ASL formed by using OPTOOL HD1100-TH (Daikin Industries). First, we measured the water contact angles of the F-ASL and thin PDMS layers with a contact angle meter (Drop Master 500: Kyowa Interface Science Co.). Results showed they were 115° and 106°, respectively. Although the contact angle of the PDMS was about 10° less than that of the F-ASL, the fact that it was still over 100° was significant. Next, we measured the adhesion and frictional forces^{6, 7)} on the Si substrate, F-ASL, and thin PDMS layer by scanning probe microscopy (SPM).

The force curve was obtained from the amount of the cantilever's deflection. The difference from

zero of the force curve indicates the adhesion force. In the case of a low-friction surface, the torsional displacement of the cantilever was small because the cantilever was able to move smoothly over the surface. On the other hand, there was a large torsional displacement of the cantilever when the surface had a high friction. The frictional curve was obtained from the torsional displacement of the cantilever. The upper and lower sides of the frictional curve are the measurement results of the approach and return routes, respectively. We determined the frictional force from the difference between the upper and lower sides of the frictional curve. A large difference between the upper and lower sides indicates a high frictional force, and in the reverse case, the frictional force is low. We used an E-sweep/NanoNavi Station (SII NanoTechnology Inc.) as the SPM system and a cantilever with a SiO₂ glass micro-particle with a 1- μ m diameter. The spring constant of the cantilever was 0.95 N/m and the contact force was approximately 10 nN. Figures 1(a), (b), and (c) show the force curves of the Si substrate, F-ASL, and thin PDMS layer, respectively.

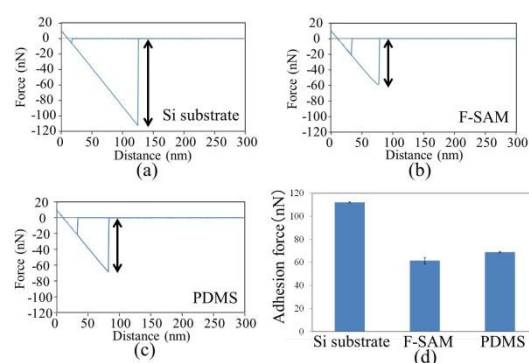


Fig. 1 Force curves of (a) Si substrate, (b) F-ASL, and (c) PDMS. (d) Adhesion forces of Si substrate, F-ASL, and PDMS.

The adhesion forces of both the F-ASL and the thin PDMS layer were lower than that of the Si substrate, although for the thin PDMS layer it was slightly higher than for the F-ASL (Fig. 1 (d)).

Figures 2(a), (b), and (c) show the frictional curves of the Si substrate, F-ASL, and thin PDMS layer, respectively. Measurement of the frictional forces by SPM revealed significant characteristics of the thin PDMS layer. The frictional forces of the F-ASL and thin PDMS layer were lower than that of the Si substrate – in fact, the PDMS had a vanishing low value.

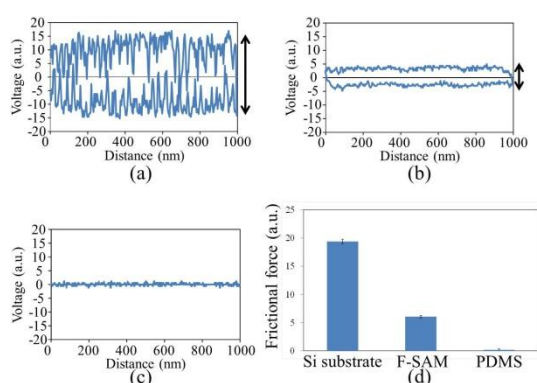


Fig. 2 Frictional curves of (a) Si substrate, (b) F-ASL, and (c) PDMS. (d) Frictional forces of Si substrate, F-ASL, and PDMS.

UV nanoimprinting using mold coated with thin PDMS layer

We performed UV nanoimprinting using a quartz mold coated with the thin PDMS layer. PAK-01 (Toyo Gosei Co.) was used as a UV-curable resin and NM-0901HB (Meisyo Kiko Co.) was used as a nanoimprint apparatus. The imprinting pressure, UV wavelength, UV intensity, and UV irradiation time were 3 MPa, 365 nm, 40 mW/cm², and 30 sec, respectively.

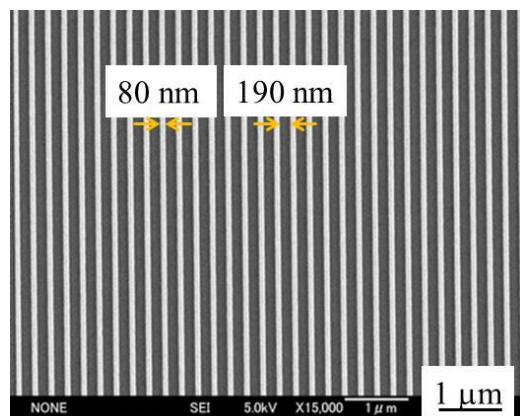


Fig. 3 SEM image of imprinted pattern.

Figure 3 shows the scanning electron microscopy (SEM) image of the imprinted pattern. The line- and space-widths were 80 and 190 nm, respectively. This result indicates that a high-resolution pattern can be obtained when PDMS is used as the antisticking layer.

Conclusion

We examined the suitability of PDMS as an antisticking layer by using a contact angle meter and SPM. The release property of the thin PDMS layer was sufficient to carry out UV nanoimprinting. Significantly, the frictional force of the PDMS had a vanishing low value. The demolding force is related to adhesion and friction between the antisticking layer and the nanoimprint resin, and we therefore expect that the demolding force will be reduced when we use the thin PDMS layer.

Acknowledgements

The authors thank Prof. S. Hosaka from Gunma University for his helpful discussions.

References

- [1] S. Y. Chou, P. R. Krauss, and P. J. Renstrom: *Appl. Phys. Lett.* **67**, 3114 (1995).
- [2] S. Y. Chou, P. R. Krauss, and P. J. Renstrom: *Science* **272**, 85 (1996).
- [3] J. Haisma, M. Verheijen, and K. Heuvel: *J. Vac. Sci. Technol. B* **14**, 4124 (1996).
- [4] I. Bitá, J. K. W. Yang, Y. S. Jung, C. A. Ross, E. L. Thomas, and K. K. Berggren: *Science*, **321**, 939 (2008).
- [5] Y. S. Jung and C. A. Ross: *Nano Lett.*, **7**, 2046 (2007).
- [6] H. A. Mizes, K.-G. Loh, R. J. D. Miller, S. K. Ahuja, and E. F. Grabowski: *Appl. Phys. Lett.*, **59**, 2901 (1991).
- [7] C. M. Mate, G. M. McClelland, R. Erlandsson, and S. Chiang: *Phys. Rev. Lett.* **59**, 1942 (1987).